Journal of Nanoparticles

Nano/Microstructured Materials 2014

Guest Editors: Amir Kajbafvala, Hamed Bahmanpour, Ali Moballegh, Mohammad H. Maneshian, and Hamid Reza Zargar

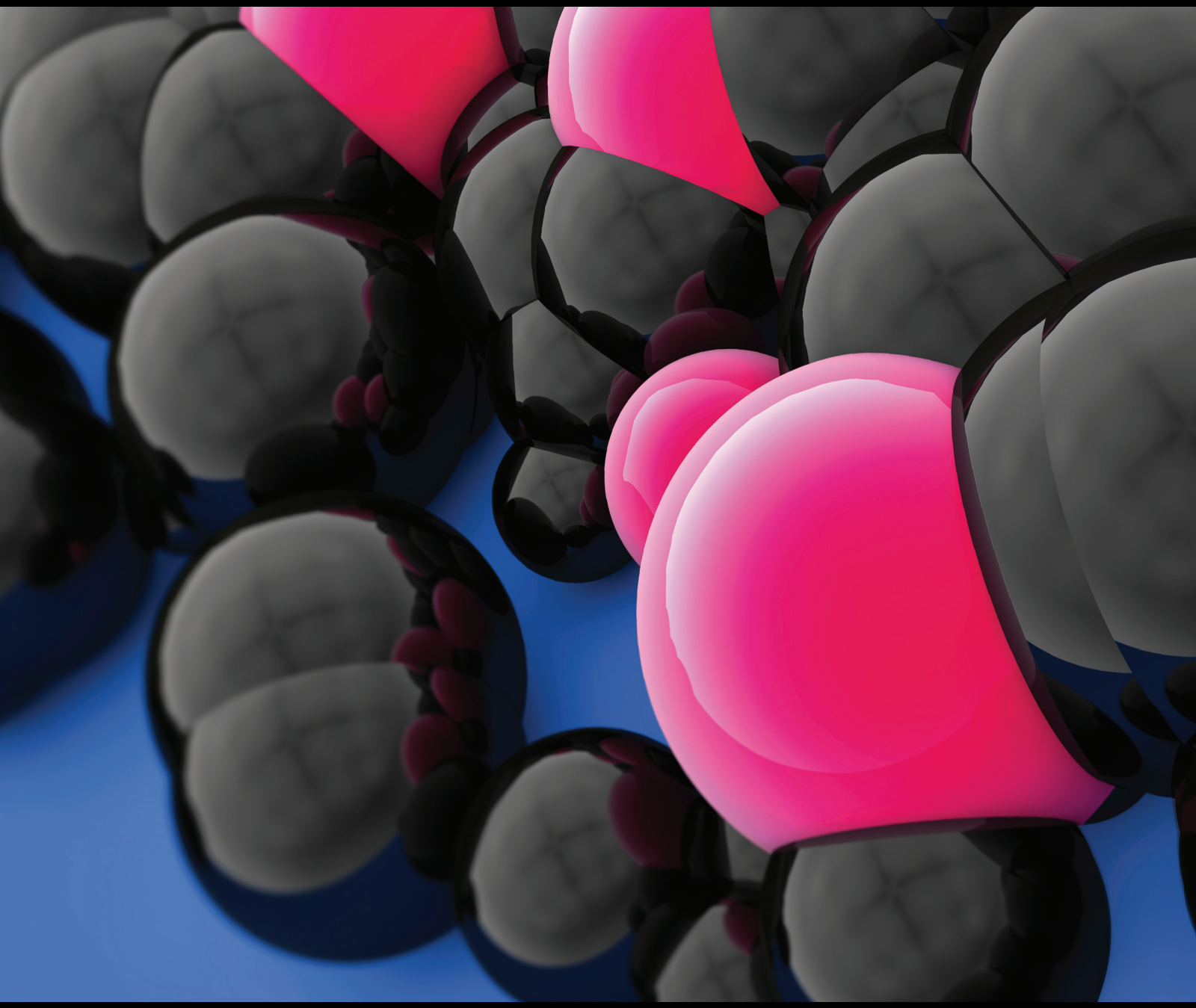

Nano/Microstructured Materials 2014

Journal of Nanoparticles

Nano/Microstructured Materials 2014

Guest Editors: Amir Kajbafvala, Hamed Bahmanpour,
Ali Moballegh, Mohammad H. Maneshian,
and Hamid Reza Zargar

Editorial Board

Contents

Nano/Microstructured Materials 2014, Amir Kajbafvala, Hamed Bahmanpour, Ali Moballegh, Mohammad H. Maneshian, and Hamid Reza Zargar
Volume 2015, Article ID 754236, 2 pages

Modulatory Effect of Citrate Reduced Gold and Biosynthesized Silver Nanoparticles on α-Amylase Activity, Kantrao Saware, Ravindra Mahadappa Aurade, P. D. Kamala Jayanthi, and Venkataraman Abbaraju
Volume 2015, Article ID 829718, 9 pages

Structured Pd/γ-Al_2O_3 Prepared by Washcoated Deposition on a Ceramic Honeycomb for Compressed Natural Gas Applications, MaThlgorzata Adamowska and Patrick Da Costa
Volume 2015, Article ID 601941, 9 pages

Plasmonic and Thermooptical Properties of Spherical Metallic Nanoparticles for Their Thermoplasmonic and Photonic Applications, Victor K. Pustovalov, Liudmila G. Astafyeva, and Wolfgang Fritzsche
Volume 2014, Article ID 893459, 15 pages

Synthesis of Silver Nanoparticles in Photosynthetic Plants, Ram Prasad
Volume 2014, Article ID 963961, 8 pages

Biogenic Synthesis of Silver Nanoparticles Using *Scenedesmus abundans* and Evaluation of Their Antibacterial Activity, Nafe Aziz, Tasneem Fatma, Ajit Varma, and Ram Prasad
Volume 2014, Article ID 689419, 6 pages

Role of Surfactant in the Formation of Gold Nanoparticles in Aqueous Medium, Abhishek Das, Ridhima Chadha, Nandita Maiti, and Sudhir Kapoor
Volume 2014, Article ID 916429, 7 pages

Hindawi Publishing Corporation
Journal of Nanoparticles
Volume 2015, Article ID 754236, 2 pages
http://dx.doi.org/10.1155/2015/754236

Editorial
Nano/Microstructured Materials 2014

Amir Kajbafvala,[1] Hamed Bahmanpour,[2] Ali Moballegh,[1] Mohammad H. Maneshian,[3] and Hamid Reza Zargar[4]

[1]*Department of Materials Science and Engineering, North Carolina State University, 911 Partners Way, Raleigh, NC 27695-7907, USA*
[2]*Department of Chemical Engineering and Materials Science, University of California, Davis, CA 95616, USA*
[3]*Micron Technology Inc., Arlington, VA 22204, USA*
[4]*Department of Metals and Materials Engineering, University of British Columbia, Vancouver, BC, Canada V6T 1Z4*

Correspondence should be addressed to Amir Kajbafvala; akajbaf@ncsu.edu

Received 8 February 2015; Accepted 8 February 2015

Recently, there is a growing interest among materials scientists and chemists to generate a diverse range of organic and inorganic molecules and compounds using eco-friendly synthesis routes, including low-cost and short synthesis times. Therefore, a primary driver of synthetic chemistry is the development of efficient and environmentally benign synthetic protocols. Most recently, many works have been published on the synthesis and characterization of various multidimensional micro/nanostructured materials by use of different synthesis methods. However, complex conditions and long synthesis time were required for most of these technologies. The main purpose of this special issue was to investigate facile and rapid synthesis methods of organic and inorganic micro/nanostructured materials, in order to maximize the efficient use of safer and cheaper raw materials, and to reduce waste for fabrication of various micro/nanostructured materials.

Original review and research articles including experimental, theoretical, or simulations works were invited. Some of the potential proposed topics were rapid, low-cost, and eco-friendly synthesis routes of micro/nanostructured materials, utilizing advanced characterization techniques for studying nanostructured materials, microwave assisted synthesis methods, green synthesis methods for fabrication of zero-, one-, and two-dimensional nanomaterials, their benefits, and their capabilities for mass production. It is worth to mention that this special issue was first lunched in 2013 and received a high number of articles. Due to its initial success, it was launched again in 2014 and it has been selected as an annual issue for Journal of Nanoparticles. This 2014 annual issue contains six articles including one review and five research articles.

In their paper, "Role of Surfactant in the Formation of Gold Nanoparticles in Aqueous Medium," A. Das et al. stabilized L-tryptophan reduced gold nanoparticles in aqueous solution by use of sodium dodecyl sulphate (SDS). Their results revealed that SDS plays an important role in the formation mechanism of the gold nanoparticles. Moreover, the reaction kinetics of the gold nanoparticles is easily observable by a steady-state spectroscopic method such as UV-Vis spectroscopy unlike $NaBH_4$ where the reaction is too fast and citrate method where heating is required to initiate the reaction. The kinetic details of the formation processes of gold nanoparticles reveal the bimodal mechanism. The observation of formation of gold nanoparticles of two different sizes, spaced over a time gap of about 30 minutes during the process of synthesis, opens up the prospect of utilizing the same reaction to tune nanoparticles size. The authors have summarized that this study guides attentions towards the potential usage of anionic surfactants in tuning the size of gold nanoparticles along with their stabilization.

In their research article "Biogenic Synthesis of Silver Nanoparticles Using *Scenedesmus abundans* and Evaluation of Their Antibacterial Activity," N. Aziz et al. synthesized silver nanoparticles (AgNPs) using the cell free extract of *Scenedesmus abundans* with $AgNO_3$. They concluded that the synthesized AgNPs through in vitro bioreduction system from unicellular microalga *Scenedesmus abundans* produced

significant amount of nanoparticles when it is exposed to 1 mM silver nitrate solution. These nanoparticles show a broad spectrum of antimicrobial activity against both Gram-positive and Gram-negative bacteria.

In the review article, "Synthesis of Silver Nanoparticles in Photosynthetic Plants," R. Prasad focused on the synthesis of nanoparticles with special emphasis on the use of plants parts for the synthesis process, its applications, and future prospectus. As one main conclusion, the author stated that the antimicrobial activity of the nanoparticles had a wide scope in the preparation of target based drug delivery and clinical diagnostics system. The identification of the specific mechanism of the AgNPs inhibition of the microbial growth or the lethal effect provides major application in the medicine, environment, soil fertility, and water quality. Moreover, the synthesis of nanoparticles with different sizes and shapes is the basic challenging task in the green synthesis of nanoparticles; this requires a basic understanding of the nuclei formation and the influence of reaction species in nuclei morphology, but still there is dormancy about the actual mechanism of the nanoparticles synthesis from the biological mode of synthesis.

In "Plasmonic and Thermooptical Properties of Spherical Metallic Nanoparticles for Their Thermoplasmonic and Photonic Applications," V. K. Pustovalov et al. investigated the influence of nanoparticles parameters (type of metal, radii, optical indexes, density, and heat capacity of nanoparticle material), characteristics of radiation (wavelength and pulse duration), and ambient parameters on plasmonic and thermophysical properties of nanoparticles. Based on this study, it was established that the maximum value of thermooptical parameter (maximum nanoparticle temperature) can be achieved with the use of absorption efficiency factor of nanoparticle which is smaller than its maximum value.

In their research article, "Structured Pd/γ-Al_2O_3 Prepared by Washcoated Deposition on a Ceramic Honeycomb for Compressed Natural Gas Applications," M. Adamowska and P. Da Costa studied the preparation of a coating procedure, from the washcoating with γ-alumina to the deposition of palladium by excess solvent or incipient wetness impregnation. The powder and the washcoat layers were studied by different characterization techniques such as SEM, BET surface area, and XRD. Vibration-resistance and heat-resistance were also evaluated. It was shown that the alumina layer is quite well deposited on the channel walls. However, a detachment of the washcoat layer was observed after ultrasound treatment. It was proved that the monolith Pd impregnation method by incipient wetness impregnation is more efficient. The presence of palladium was confirmed using HRTEM, the palladium was present under the Pd (II) oxidation state, and the size of PdO particles varies between 2.5 and 3.1 nm. The catalytic properties of the monolith catalyst were carried out using temperature programmed surface reaction (TPSR).

In, "Modulatory Effect of Citrate Reduced Gold and Biosynthesized Silver Nanoparticles on α-Amylase Activity," K. Saware et al. described a novel approach to study the interaction of amylase enzyme with gold nanoparticles (AuNPs) and silver nanoparticles (AgNPs) and checked its catalytic function. AuNPs were synthesized using citrate reduction method and AgNPs were synthesized using biological route employing *Ficus benghalensis* and *Ficus religiosa* leaf extract as a reducing and stabilizing agent to reduce silver nitrate to silver atoms. A modulatory effect of nanoparticles on amylase activity was observed. Gold nanoparticles are excellent biocompatible surfaces for the immobilization of enzymes. Immobilized amylase showed 1- to 2-fold increase of activity compared to free enzyme. The biocatalytic activity of amylase in the bioconjugate was marginally enhanced relative to the free enzyme in solution. The bioconjugate material also showed significantly enhanced pH and temperature stability. The results indicate that the present study paves way for the modulator degradation of starch by the enzyme with AuNPs and biogenic AgNPs, which is a promising application in the medical and food industry.

Acknowledgments

At the end, the guest editors would like to express sincere appreciation to all the authors who have contributed in this 2014 annual issue. Moreover, our thanks are also extended to all of the reviewers for their valuable time and for enhancing the quality of these articles.

Amir Kajbafvala
Hamed Bahmanpour
Ali Moballegh
Mohammad H. Maneshian
Hamid Reza Zargar

Hindawi Publishing Corporation
Journal of Nanoparticles
Volume 2015, Article ID 829718, 9 pages
http://dx.doi.org/10.1155/2015/829718

Research Article

Modulatory Effect of Citrate Reduced Gold and Biosynthesized Silver Nanoparticles on α-Amylase Activity

Kantrao Saware,[1] Ravindra Mahadappa Aurade,[2] P. D. Kamala Jayanthi,[2] and Venkataraman Abbaraju[1,3]

[1]*Materials Chemistry Laboratory, Department of Materials Science, Gulbarga University, Gulbarga, Karnataka 585106, India*
[2]*Indian Institute of Horticultural Research, Hessaraghatta Lake Post, Bengaluru, Karnataka 5600 89, India*
[3]*Department of Chemistry, Gulbarga University, Gulbarga, Karnataka 585106, India*

Correspondence should be addressed to Venkataraman Abbaraju; raman_chem@rediffmail.com

Received 28 July 2014; Accepted 5 October 2014

Academic Editor: Amir Kajbafvala

Amylase is one of the important digestive enzymes involved in hydrolysis of starch. In this paper, we describe a novel approach to study the interaction of amylase enzyme with gold nanoparticles (AuNPs) and silver nanoparticles (AgNPs) and checked its catalytic function. AuNPs are synthesized using citrate reduction method and AgNPs were synthesized using biological route employing *Ficus benghalensis* and *Ficus religiosa* leaf extract as a reducing and stabilizing agent to reduce silver nitrate to silver atoms. A modulatory effect of nanoparticles on amylase activity was observed. Gold nanoparticles are excellent biocompatible surfaces for the immobilization of enzymes. Immobilized amylase showed 1- to 2-fold increase of activity compared to free enzyme. The biocatalytic activity of amylase in the bioconjugate was marginally enhanced relative to the free enzyme in solution. The bioconjugate material also showed significantly enhanced pH and temperature stability. The results indicate that the present study paves way for the modulator degradation of starch by the enzyme with AuNPs and biogenic AgNPs, which is a promising application in the medical and food industry.

1. Introduction

Nanoparticles are defined as particulate dispersions with a size in the range of 10–100 nm [1]. The nanostructures have also a great potential in biotechnological processes taking into account that each may be used as carriers for enzymes during different biocatalytic transformations [2]. Different types of biomolecules such as proteins, enzymes, antibodies, and anticancer agents can be immobilized on these nanoparticles.

Interaction of metal nanoparticles with biomolecules has received much attention in the recent years for the development of diagnostics, for sensors, and for targeted drug delivery. Further, nanoparticles also have promising medical applications for wound healing, diagnostics, biosensing, and drug delivery [3–6]. Increased activity of glucose oxidase was noticed when immobilized onto AgNPs [7]. AgNPs, a potential nanocatalyst for the rapid degradation of starch hydrolysis by α-amylase, were studied by researchers [8]. The functionlised AuNPs have been extensively used for the detection of various enzymes and also for measurement of their activity [9–11]. For example, chemical or electrostatic attachment of enzymes to functionlised AuNPs may alter the catalytic properties either by increasing or by decreasing the affinity for enzyme-substrate formation [12–14]; enhancing its stability [12, 13]; enhancing the rate of product formation (although significant report in this regard is still lacking) [12, 13] or retention [15]; and even having some loss of activity of the enzyme [16]. Similarly, interaction with AuNPs has been found to enhance the stability of peptides [17]. Their unique property arises specifically from higher surface to volume ratio and increased percentage of atoms at the grain boundaries. They represent an important class of materials in the development of novel devices that can be used in various physical, biological, biomedical, and pharmaceutical applications [18–20]. Nanotechnology has a wide application in

pest management as nanocapsules for herbicide delivery, vector/pest control, and nanosensors for pest detection [21]. Synthesized silver or gold nanoparticles also help to produce new insecticides and insect repellants.

AuNPs and biointeractions studies are now widely accepted as protein corona rapidly forms on AuNPs surfaces when introduced into a biological medium [22]. The adsorption of proteins to the surface of the AuNPs can significantly change the surface charge of the AuNPs, which has important consequences for nanoparticle fate and transport in biological systems. Therefore, the composition of the protein corona largely defines the biological identity of the nanoparticle. In addition, because of their extremely large surface area to volume ratios, a significant number of proteins can be adsorbed and "trapped" on AuNPs surfaces when they are introduced into biological entities [22–27]. Gold nanoparticles present an alternate and advantageous synthetic scaffold for targeting protein surfaces [28] and have been demonstrated to bind biomacromolecules, [29] facilitate DNA transfection [30], and reversibly inhibit enzymes [31]. The binding of albumin protein on the surfaces of silver and gold nanoparticles has been studied for surface adhesion by researchers to understand the effect on its structural changes [32, 33]. Biointeraction studies with AgNPs and protein and its SPR effect, surface charge effect was studied for various applications in biological sciences by various researchers [34, 35].

Enzymes are biological catalysts that speed up reactions in the presence or absence of cofactors without any change in their activity. α-Amylase is one of the chief digestive enzymes present in all living organisms and amylases in saliva/the pancreas of animals break down the long-chain polysaccharide starch into maltose and glucose. Amylases are the most important in food industry and medicinal applications.

So in this study, we used silver and gold nanoparticles for the interaction and catalytic action of α-amylase. The present study aims to investigate enzyme-catalyzed starch hydrolysis in the presence of AuNPs and green AgNPs. This forms a basis for nanoparticle-bimolecular interaction that may be potentially applied in the medical and food industry. Thus, we report here the modulation of enzymatic activity in the presence of AuNPs and AgNPs. Absorbance, fluorescence spectroscopic measurements, and other chemical tests were done to establish that the enzymes were attached to the NPs.

2. Materials and Methods

2.1. Chemicals and Reagents. α-Amylase (ex-porcine extrapure), soluble starch, $AgNO_3$, $HAuCl_4$, and ammonium molybdate purchased from Himedia, Bangalore, India, and all other chemicals used were of high purity and analytical grade. For all the experiments, ultrafiltered Milli-Q water (Millipore, USA) was used.

2.2. Synthesis of Gold Nanoparticles. Gold nanoparticles of 10–20 nm diameter were prepared by the citrate reduction route [36]. Briefly the method involves reducing 5×10^{-4} M Au^{+3} by 1.2×10^{-3} M citrate in water by refluxing for 30 min. The cluster solution was red wine for gold [37].

2.3. Biosynthesis of Silver Nanoparticles. Biosynthesis of silver nanoparticles is according to our previous report [38]. The *Ficus benghalensis* (FB) and *Ficus religiosa* (FR) leaf extracts are used for synthesis of silver nanoparticles. Fresh, healthy, and green leaves from FR and FB plants were collected from the Gulbarga University campus, Gulbarga, India. In this experiment, 5 mL of leaf extract was added to 95 mL of a 10^{-3} M aqueous $AgNO_3$ (silver nitrate) solution and exposed for 3 min in microwave oven. Periodically aliquots of the reaction solution were removed and subjected to UV-Vis spectroscopy measurements for surface Plasmon resonance study of AgNPs synthesis. Controls containing leaf extract (without silver nitrate) as positive controls and pure silver nitrate solution (without leaf extract) as negative controls were also run simultaneously along with the experimental flask in three replicates.

2.4. UV-Visible Spectral Studies. The measurement of maximum absorbance peak of AuNPs and AgNPs was carried out using U-3010 spectrophotometer. UV-visible absorbance spectrum was measured between 200 and 800 nm in 1 cm quartz cuvette containing 2 mL of nanoparticle solution at room temperature. Interactions of silver and gold nanoparticles with amylase were measured spectrophotometrically. UV-visible absorbance spectrum was measured between 200 and 800 nm in 1 cm quartz cuvette containing protein (50 μg/mL) in 50 mM Tris-HCl buffer, with pH 7.4 at room temperature. Amylase in Tris-HCl buffer is titrated with increasing concentrations (0, 5, 10, 20, 30, and 50 μL) of silver and gold nanoparticles.

2.5. Tryptophan Fluorescence Emission Spectra. The interaction of binding of silver and gold nanoparticles to pure α-amylase was determined by Trp fluorescence quenching titrations as described previously [39]. Briefly, amylase (50 μg/2 mL) was titrated in 50 mM Tris-HCl buffer, with pH 7.4 with increasing concentrations of silver and gold nanoparticles (0, 5, 10, 20, 30, 40, and 50 μL), respectively. However, quenching of Trp fluorescence emission of amylase was monitored at 335 nm following excitation at 280 nm (slit width for both, 5 nm) using Varian spectrofluorometer.

2.6. Morphological Studies Using AFM for AgNPs and FESEM for AuNPs. Samples of silver nanoparticles were synthesized using leaf extracts of FB and FR. Atomic force microscopy (AFM) was prepared by solution casting onto silicon wafers to make thin films. These films were analysed in noncontact mode using a Pacific Nanotechnology Nano-R2 instrument with SiN probes at a scan rate of 0.5 Hz in the air. The morphology of the gold nanoparticles synthesized by citrate reduction method and AuNPs with amylase enzyme was examined using Field Emission Scanning Electron Microscopy (FESEM, FEI Nova nano 600, Netherlands), and for this the images were operated at 15 KV on a 0° tilt position.

2.7. Immobilization of Amylase. Amylase-silver and gold nanoparticles bioconjugates were prepared according to [40]. Briefly, the AgNPs/AuNPs solution prepared was diluted by a factor of 3 with a glycine buffer (75 mM, pH 8.0). Amylase (mg/mL) was added with stirring to a portion of the diluted solution containing the AgNPs/AuNPs (50 mL; 50 mM glycine buffer, pH 8.0). The solution was equilibrated for 1 h before being centrifuged at 18,000 rpm for 20 min to remove the uncoordinated amylase remaining in solution. The precipitate obtained was subjected to three repeated wash cycles involving rinsing with 50 mM glycine buffer (50 mL) and centrifuging at 18.000 rpm for 20 min. Finally, the AgNP-amylase and AuNPs-amylase bioconjugates were suspended in the 50 mM glycine buffer, with pH 8 (5 mL) for further experiments.

2.8. Amylase Activity by DNS Method. The amylase activity was measured in presence of silver and gold nanoparticles as reported earlier [41]. Amylase activity was measured in presence of different concentrations of silver and gold nanoparticles by DNS method. We also assay the effect of nanoparticles on amylase activity with increasing concentrations of starch. Briefly, the activity was estimated by DNS method, enzyme-AuNPs bionanoconjugates was added to various test tubes each containing 0, 0.25, 5, 10, 20, 30, 40, and 50 mg mL^{-1} of starch solution. All of these test tubes were then incubated in a water bath at 37°C for 20 min. The UV-Vis spectrum was recorded at 570 using a U-3010 spectrophotometer (Tokyo, Japan). The released sugar in the test sample was quantified and the enzyme activity was calculated (expressed in μg/mL/min). We also assayed stabilities of the free and immobilized α-amylase which was studied according to [42]. All the experiments were performed at least three times.

3. Results and Discussion

The present study reveals the modulatory effect of AuNPs and biosynthesized AgNPs on enzyme activity during the hydrolysis of starch. The solution turned pale yellow after 2 min, and the colour change confirmed the presence of AgNPs. The organic moiety of soluble leaf extract is assumed to reduce silver nitrate, thus acting as both stabilizing and reducing agent [43]. The Plasmon peak observed at 435 and 440 nm confirmed the presence of AgNPs (Figures 1(a) and 1(b)). The absorbance peaks that occurred at around 400 nm are the characteristic SPR signature of AgNPs [44]. The $HAucl_4$ reduced by citrate reduction showing red wine color after 10 min confirmed the formation of gold nanoparticles and the SPR peak is observed at 510 nm (Figure 2). The absorbance peak around 526 nm with the peak position remaining practically constant also indicates the production of gold nanoparticles [45]. We observed a faint pink coloration of the solution after several pulses of the experiment. In the solutions absorption spectra, the surface Plasmon peak (around 510–530 nm) could be clearly distinguished which was consistent with the presence of small 3–30 nm particles in the colloid [46]. It was also noted that the resulting AuNPs and AgNPs nanoparticle solutions were found to be stable for more than a month without agglomeration of particles.

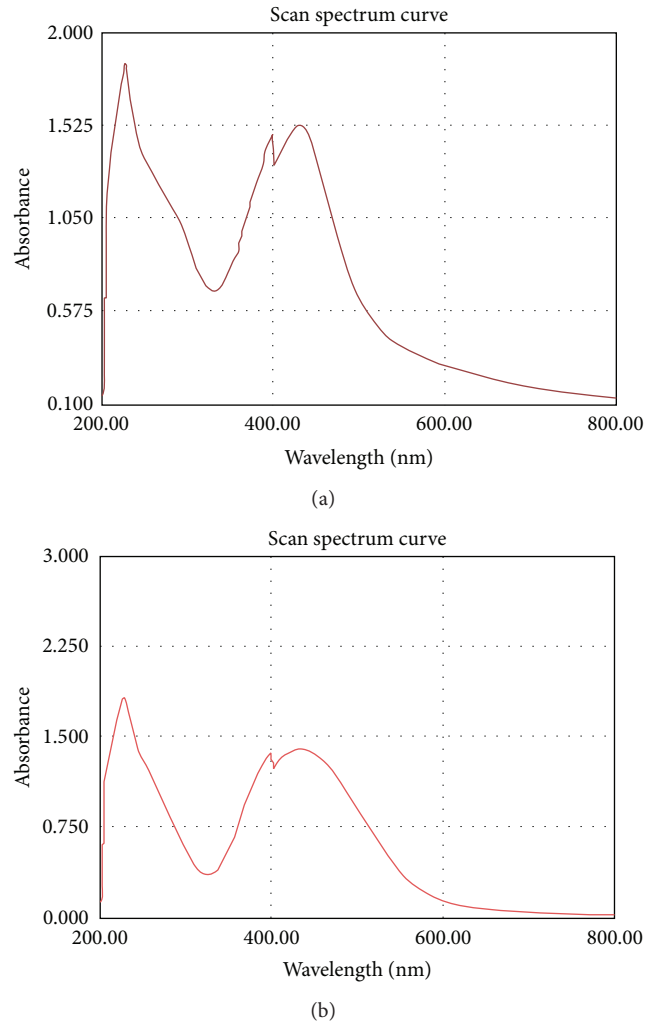

Figure 1: Absorbance spectra of silver nanoparticles. (a) Spectra of FR nanoparticles; (b) spectra of FB silver nanoparticles.

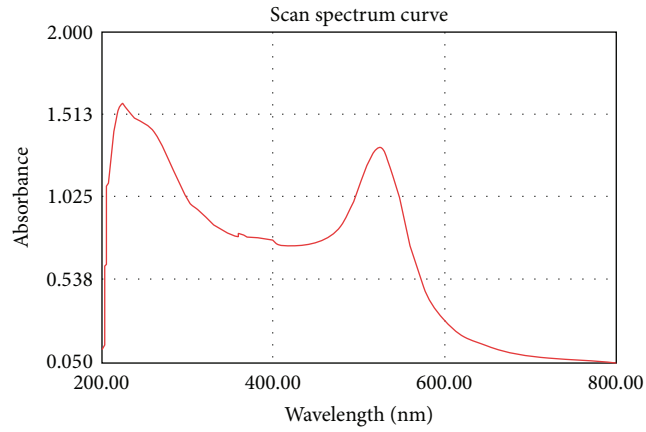

Figure 2: Absorbance spectra of gold nanoparticles.

Atomic force microscopy (AFM) was used to probe the sample's surface morphology and roughness. Figure 3 shows the typical three-dimensional (3D) height image of silver

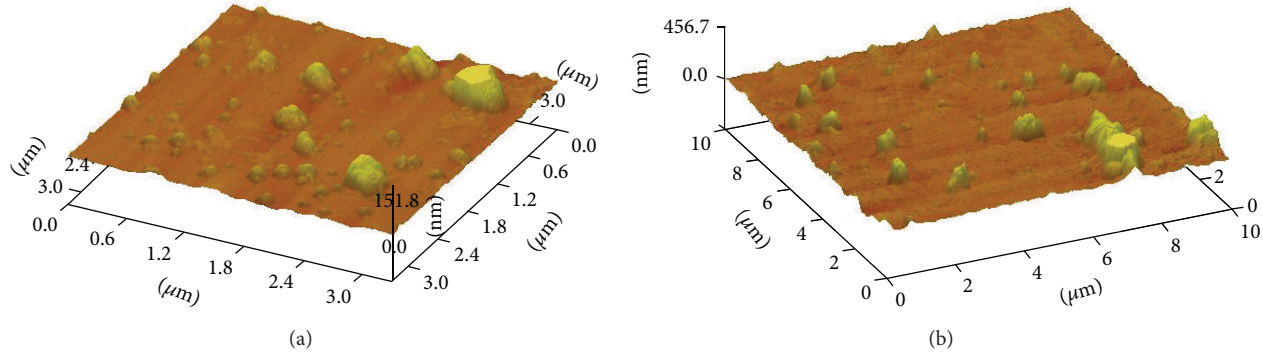

(a) (b)

Figure 3: 3D image of AgNPs using atomic force microscopy. (a) AgNPs of *Ficus benghalensis* and (b) *Ficus religiosa.*

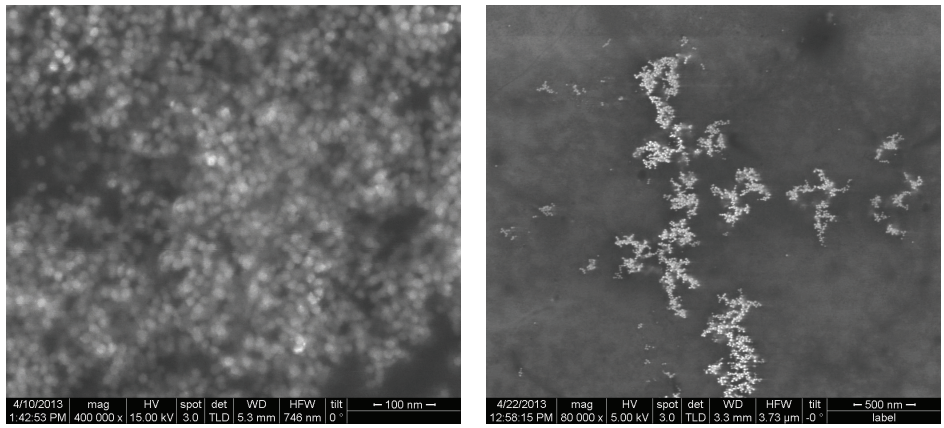

(a) (b)

Figure 4: (a) FESEM image of citrate reduced gold nanoparticles 10–15 nm. (b) Citrate reduced gold nanoparticles with α-amylase enzyme.

nanoparticles with surface having spherical particles with grains sized between 20 and 75 nm in diameter with mean size of about 35 nm. This magnification is attributed to the convolution of true particle size with that of the AFM tip (the size and shape of the features observed by AFM can be influenced by the effects of tip-sample convolution) and also to the preparation of samples for AFM. Wider scans covering a few micrometers yielded a root mean square (RMS) roughness of 10 nm with a maximum peak-to-valley distance of 65 nm.

To understand the core-shell morphology of the synthesized AuNPs- and AuNPs-amylase bioconjugate FESEM technique was employed. Figure 4 shows the FESEM images of the AuNPs synthesized using citrate reduction method. On careful observation, each individual AuNP is seen as spherical in shape, whereas AuNPs and amylase bioconjugate showed a fine capping on each particle and the same may also be responsible for interparticle binding. It is observed from this image that the nanoparticles are isolated and are surrounded by a layer of organic matrix at some places which acts as capping. Almost all of the AuNPs are spherical in shape and are in the size range of 10–15 nm indicating monodispersity.

The UV-Vis absorbance spectra were recorded from the α-amylase solution before (spectrum 1) and after (spectra 2–5) addition of AgNPs of FR (Figure 5(a)) and FB (Figure 5(b)) silver colloidal solution (0, 5, 10, 20, 30, and 50 μL). With the addition of silver nanoparticles, an increase was noticed in absorbance spectra. The blue shift of α-amylase (2–8 nm) was seen for both FB and FR nanoparticles, respectively. The results indicate that these silver nanoparticles interacted with amylase and affect its folding changes toward native structure. Similarly gold nanoparticles also interacted with amylase and enhanced the absorbance spectra of amylase with the addition of increasing concentration of AuNPs (Figure 5(c)) and a slight conformational change of α-amylase with interaction of AuNPs was observed.

Tryptophan fluorescence quenching measurement results showed that AgNPs and AuNPs interacted and bound with high affinity to amylase. The Trp emission spectra were decreased with addition of increasing concentrations of FB and FR nanoparticles (Figures 6(a) and 6(b)). The Trp fluorescence emission of amylase was quenched almost 30–60% by FR and FB AgNPs, respectively. However, there is no emission shift with addition of AgNPs.

Similarly, the Trp emission spectra were decreased with addition of increasing concentrations of AuNPs (Figure 6(c)). AuNPs interacted with high affinity with amylase and a small blue shift was observed. The results indicate that AuNPs interacted and bound with amylase with high affinity causing conformational changes of amylase. Earlier, Deka et al. [41] reported that gold nanoparticles interacted with α-amylase.

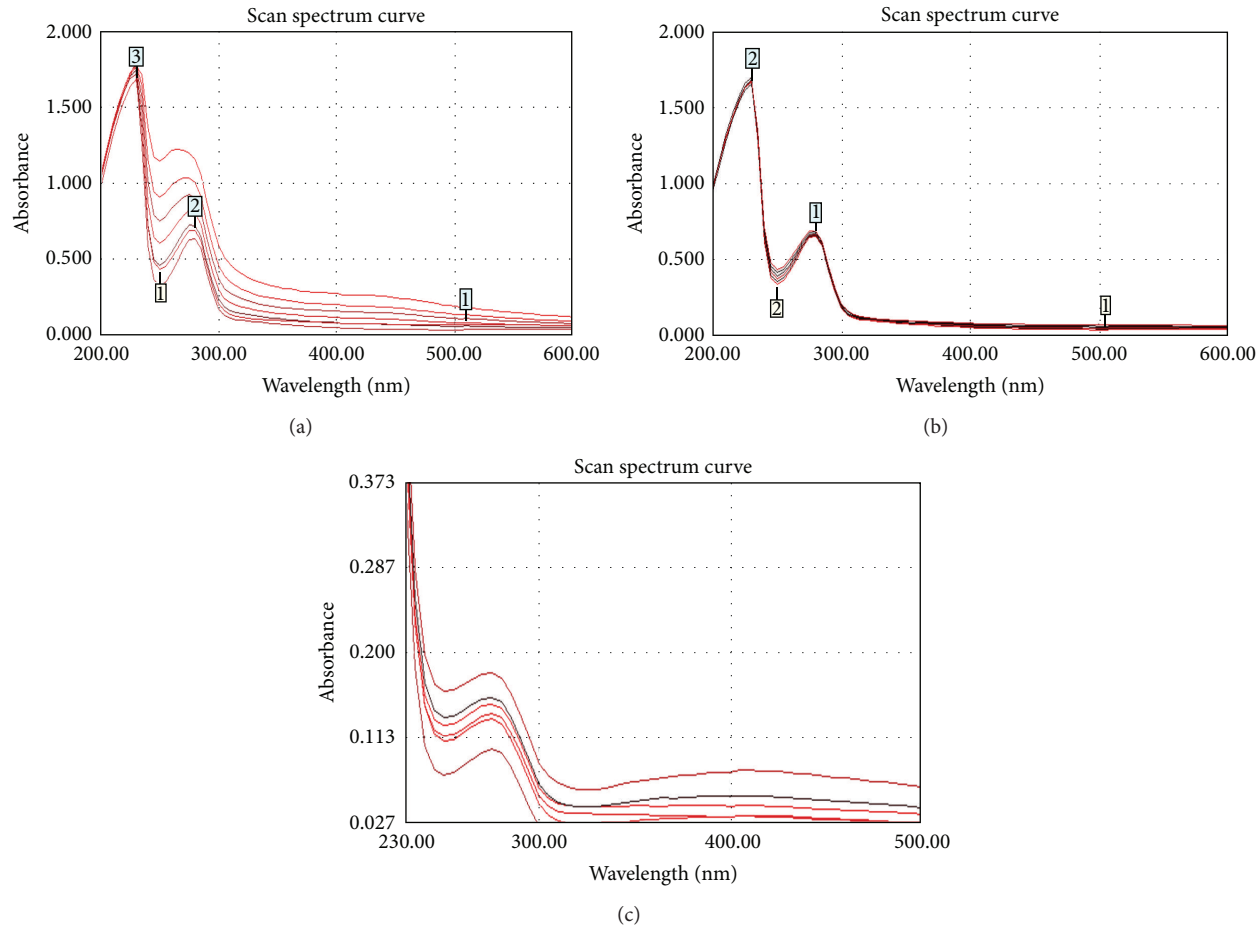

FIGURE 5: Measurement of absorbance spectrum of α-amylase in presence of nanoparticles. Absorbance spectra of α-amylase at pH 7.4. Absorbance spectra were increasing with addition of (a) FR silver nanoparticles; (b) FB silver nanoparticles (5, 10, 20, 30, 40, and 50 μL), respectively; and (c) gold nanoparticles.

Ernest et al. reported that AgNPs enhance amylase activity [8]. We also observed that FR silver nanoparticles stimulate amylase activity at lower concentrations and inhibited it at higher concentration as shown in Figure 7. Similarly, FB nanoparticles also stimulated amylase activity at lower concentration and inhibited it at higher concentration. Silver nanoparticles demonstrated activator effect on the cholinesterase and monoamine oxidase activities, and these effects increased with increasing concentrations of the nanoparticles [47]. The enzyme was attached to the nanoparticle following the degradation of starch from the composite and not to the reducing sugars although the enzymatic activity was retained [48]. We also found that gold nanoparticles increased amylase activity up to 2-fold. The rate of reaction was found to be increased in the presence of gold nanoparticles (Figure 7(b)). There is an increase of 2-fold reducing sugar formation suggesting that the gold nanoparticles have a significant role as a nanocatalyst in rapidly degrading the complex polysaccharide starch to reducing sugars, while at higher concentrations of gold particles amylase activity was decreased. Deka et al. [41] also reported similar modulatory effect on amylase where the results have been explained based on a model that considered the presence of enzyme bound to NP and that available for enhanced catalysis, enzyme bound to NP but unavailable due to being buried inside the agglomerate and the free enzyme.

The immobilization of α-amylase takes places on the surface of the FR and FB AgNPs or AuNPs. Immobilized amylase activity was increased by 60–90%, (Figure 8(a)) with FR and FB AgNPs, respectively, when compared to the free enzyme. AgNPs generally have the tendency to agglomerate faster in any biological medium and sediment at the bottom. To our surprise, no such agglomeration was seen during the reaction and thus we confirm that the AgNPs have the chances of being stabilized by the protein molecule through the thiol linkages, and thus the enzyme molecule is immobilized [48]. A well-known fact is that, upon a solid support, the efficiency of the enzyme is increased compared to its free form [49]. This may possibly act as a nanocatalyst in the hydrolysis of starch catalyzed by an amylase. Thus, the reaction rate is increased in the presence of AgNPs although the exact binding mechanism remains to be explored. Similarly, Figure 8(b) shows that immobilized amylase on gold nanoparticles activity was increased by 100% when compared

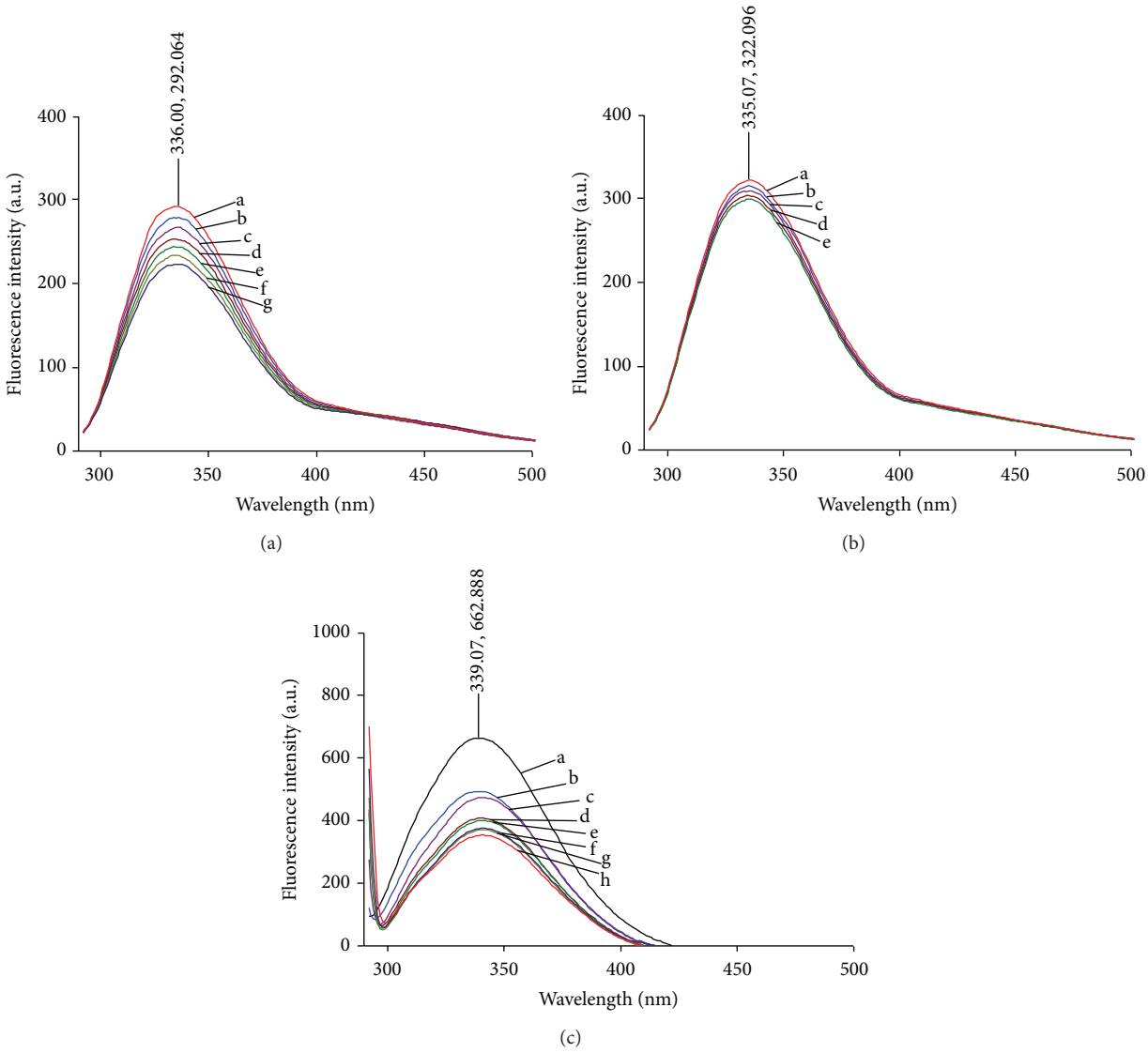

FIGURE 6: Tryptophan fluorescence quenching spectra of α-amylase with nanoparticles. Line (a) corresponds to amylase alone; Line (b-g) with nanoparticles. (a) Amylase + FB AgNPs; (b) amylase + FR AgNPs; (c) amylase + gold nanoparticles. Decreasing of Trp fluorescence spectra with increasing (5, 10, 15, 20, and 30 μL) concentration of silver and gold nanoparticles. Amylase titrated with increasing concentration of nanoparticles excitation at 280 nm followed emission at 335 nm (slit width for both 5 nm).

with free enzymes. In our present study, biosynthesized AgNPs and citrate reduced AuNPs upon interaction with α-amylase were capable of breaking down the starch complex with the attachment of the enzyme over its surface, thereby being immobilized and degrading starch much faster than when compared to free enzyme. Because the collision frequency between the soluble (free) enzyme, the substrate molecule and their steric orientations form the basis of the enzyme activity and the constraint is overcome by the immobilized enzyme with the support of a solid nanoparticle whereas it does not occur in the case of free starch. Therefore, the reaction velocity is high and the breakdown of starch to smaller molecules as monosaccharides and disaccharides is faster. Amylase activity was increased with increasing concentration of starch in presence of nanoparticles as shown in Figure 9. It indicates that nanoparticles enhance the basal amylase activity.

Pepsin immobilized on AuNPs surface was more stable when compared with the free enzyme [50]. Similarly we observed that AgNPs and AuNPs were increasing the stability of amylase activity. Free amylase and amylase mixed with AuNPs or AgNPs solutions were kept at room temperature for 5 days and the comparison of the activities was determined every 12 hours. The results showed a slight enzyme activity retained in all tests; this kind of stability increase is time dependent (Figure 10). This means that the longer the enzymes are kept at room temperature, the more activity increase can be detected in the sample of amylase mixed with

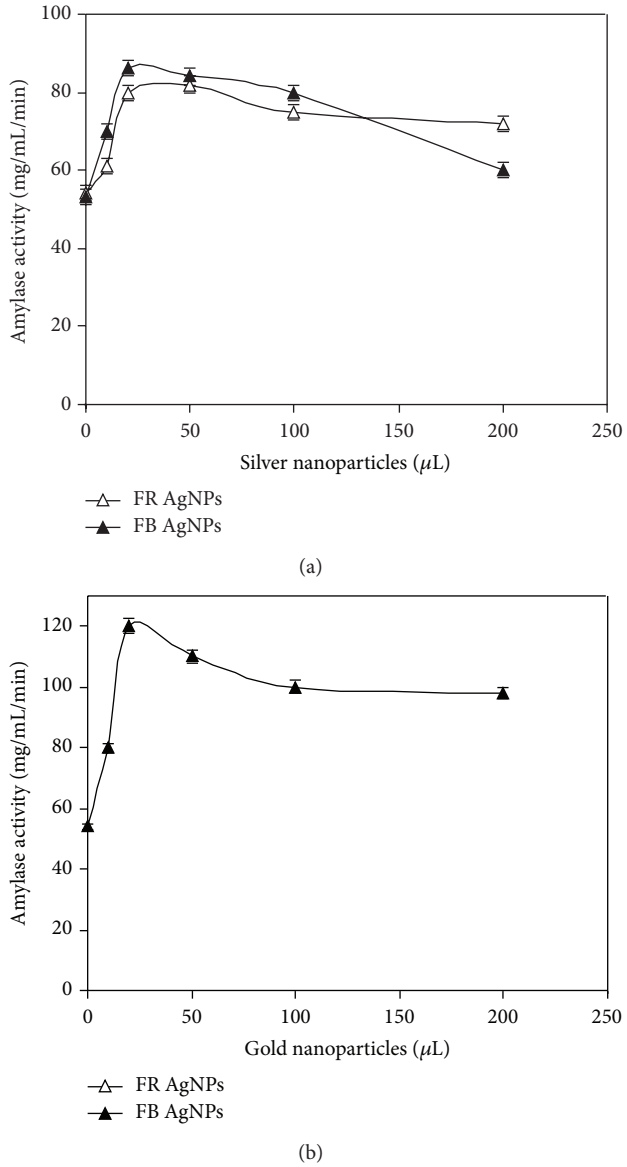

Figure 7: Modulatory effect of silver and gold nanoparticles on α-amylase activity. (a) (▲): effect of FB AgNPs on amylase; (△): effect of FR AgNPs on amylase; (b) effect of gold nanoparticles. Data points represent the mean of at least three determinations.

AuNPs or AgNPs solutions. This result clearly demonstrated that the AuNPs or AgNPs can stabilize the activity of amylase, when compared with the free enzyme.

4. Conclusion

In summary, biosynthesized AgNPs and AuNPs showed an increased rate of reaction with α-amylase. The degradation of starch digestion kinetics in the presence of AgNPs/AuNPs rapidly produced larger amounts of reducing sugars. This study showed that the nanoparticle may have a significant effect in the field of nanocatalysis, promising their potential use in industries for rapid degradation of the complex

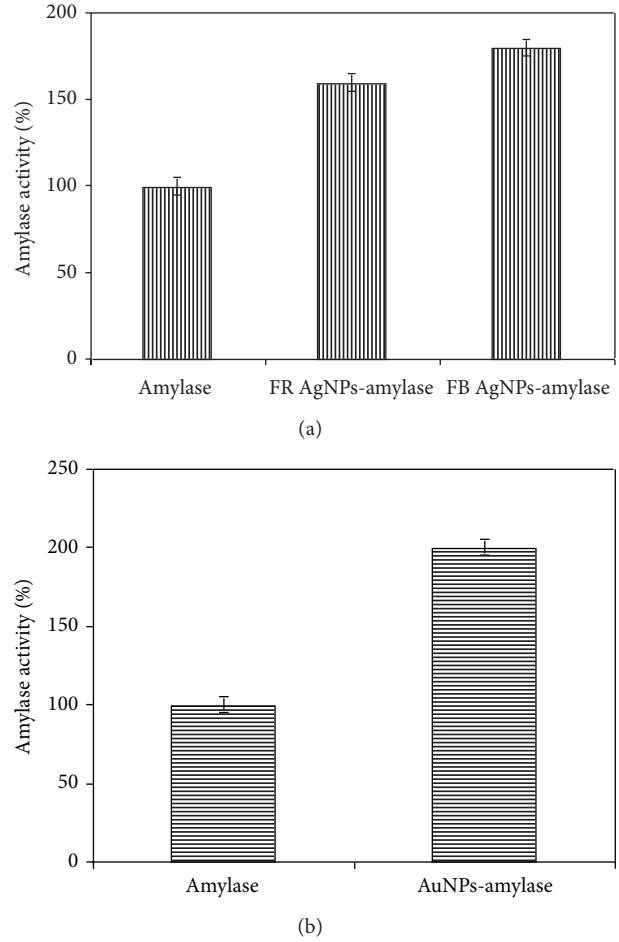

Figure 8: Assay of immobilized amylase activity. (a) Amylase + silver nanoparticles; (b) amylase + gold nanoparticles. Data points represent the mean of at least three determinations.

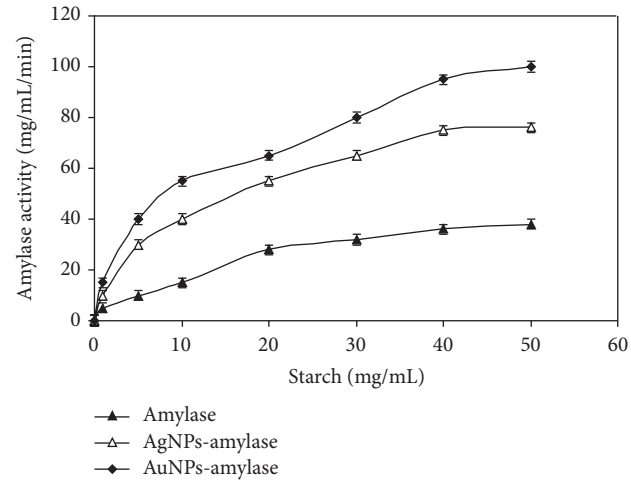

Figure 9: Effect of substrate concentrations on α-amylase activity in the presence of nanoparticles as compared to the control (enzyme in absence of NPs). Legend represents the respective concentration of starch at which the experiments were carried out. The concentration of AgNPs/AuNPs was same for all of the above. Data points represent the mean of at least three determinations.

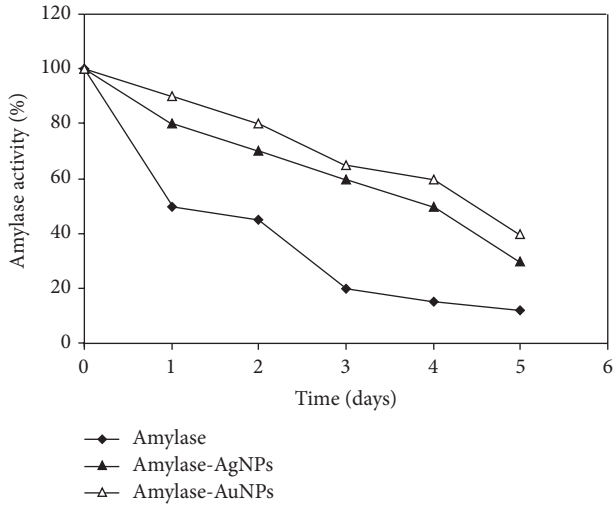

Figure 10: Comparison of storage stabilities of the free and immobilized α-amylase at room temperature. Data points represent the mean of at least three determinations.

molecule to simpler ones by immobilizing the enzymes onto the surface of nanoparticles. They could also be possibly used in assay kits as they are less time consuming and for biomedical applications such as drug delivery and sensing.

Conflict of Interests

The authors report no conflict of interests. The authors alone are responsible for the content and writing of the paper.

Authors' Contribution

Kantrao Saware and Ravindra Mahadappa Aurade contributed equally to the paper.

Acknowledgments

The author Kantrao Saware thanks Professor G. U. Kulkarni for fruitful guidance and Selvi Rajan, JNCASR Bangalore, for FESEM measurements. Venkataraman Abbaraju thanks UGC, New Delhi, Government of India, for financial support in the form of project. Kantrao Saware thanks Dr. Shivashankar KS, IIHR, Bangalore, for providing fluorescence spectrophotometer.

References

[1] S. P. Gubin, Y. A. Koksharov, G. B. Khomutov, and G. Y. Yurkov, "Magnetic nanoparticles: preparation, structure and properties," *Russian Chemical Reviews*, vol. 74, no. 6, pp. 489–520, 2005.

[2] K. J. Dussán, O. H. Giraldo, and C. A. Cardona, "Application of magnetic nanostructures in biotechnological processes: biodiesel production using lipase immobilized on magnetic carriers," in *Proceedings of the European Congress of Chemical Engineering*, Copenhagen, Denmark, September 2007.

[3] D. Roe, B. Karandikar, N. Bonn-Savage, B. Gibbins, and J.-B. Roullet, "Antimicrobial surface functionalization of plastic catheters by silver nanoparticles," *Journal of Antimicrobial Chemotherapy*, vol. 61, no. 4, pp. 869–876, 2008.

[4] C.-F. Chau, S.-H. Wu, and G.-C. Yen, "The development of regulations for food nanotechnology," *Trends in Food Science and Technology*, vol. 18, no. 5, pp. 269–280, 2007.

[5] F. Furno, K. S. Morley, B. Wong et al., "Silver nanoparticles and polymeric medical devices: a new approach to prevention of infection?" *Journal of Antimicrobial Chemotherapy*, vol. 54, no. 6, pp. 1019–1024, 2004.

[6] M. Das, C. Mohanty, and S. K. Sahoo, "Ligand-based targeted therapy for cancer tissue," *Expert Opinion on Drug Delivery*, vol. 6, no. 3, pp. 285–304, 2009.

[7] X. Ren, X. Meng, D. Chen, F. Tang, and J. Jiao, "Using silver nanoparticle to enhance current response of biosensor," *Biosensors and Bioelectronics*, vol. 21, no. 3, pp. 433–437, 2005.

[8] V. Ernest, P. J. Shiny, A. Mukherjee, and N. Chandrasekaran, "Silver nanoparticles: a potential nanocatalyst for the rapid degradation of starch hydrolysis by α-amylase," *Carbohydrate Research*, vol. 352, pp. 60–64, 2012.

[9] Z. Wang, R. Lévy, D. G. Fernig, and M. Brust, "Kinase-catalyzed modification of gold nanoparticles: a new approach to colorimetric kinase activity screening," *Journal of the American Chemical Society*, vol. 128, no. 7, pp. 2214–2215, 2006.

[10] M. R. Choi, K. J. Stanton-Maxey, J. K. Stanley et al., "A cellular trojan horse for delivery of therapeutic nanoparticles into tumors," *Nano Letters*, vol. 7, no. 12, pp. 3759–3765, 2007.

[11] R. Bonomi, A. Cazzolaro, A. Sansone, P. Scrimin, and L. J. Prins, "Detection of enzyme activity through catalytic signal amplification with functionalized gold nanoparticles," *Angewandte Chemie: International Edition*, vol. 50, no. 10, pp. 2307–2312, 2011.

[12] P. Pandey, S. P. Singh, S. K. Arya et al., "Application of thiolated gold nanoparticles for the enhancement of glucose oxidase activity," *Langmuir*, vol. 23, no. 6, pp. 3333–3337, 2007.

[13] K. G. Kouassi, J. Irudayaraj, and G. McCarthy, "Examination of cholesterol oxidase immobilization onto magnetic nanoparticles," *BioMagnetic Research and Technology*, vol. 3, article 1, 2005.

[14] B. J. Jordan, R. Hong, G. Han, S. Rana, and V. M. Rotello, "Modulation of enzyme-substrate selectivity using tetraethylene glycol functionalized gold nanoparticles," *Nanotechnology*, vol. 20, no. 43, Article ID 434004, 2009.

[15] G. K. Ahirwal and C. K. Mitra, "Direct electrochemistry of horseradish peroxidase-gold nanoparticles conjugate," *Sensors*, vol. 9, no. 2, pp. 881–894, 2009.

[16] L. M. Rossi, A. D. Quach, and Z. Rosenzweig, "Glucose oxidase-magnetite nanoparticle bioconjugate for glucose sensing," *Analytical and Bioanalytical Chemistry*, vol. 380, no. 4, pp. 606–613, 2004.

[17] M. M. Varma, D. D. Nolte, H. D. Inerowicz, and F. E. Regnier, "Spinning-disk self-referencing interferometry of antigen-antibody recognition," *Optics Letters*, vol. 29, no. 9, pp. 950–952, 2004.

[18] J.-M. Nam, C. S. Thaxton, and C. A. Mirkin, "Nanoparticle-based bio-bar codes for the ultrasensitive detection of proteins," *Science*, vol. 301, no. 5641, pp. 1884–1886, 2003.

[19] A. G. Tkachenko, H. Xie, Y. Liu et al., "Cellular trajectories of peptide-modified gold particle complexes: comparison of nuclear localization signals and peptide transduction domains," *Bioconjugate Chemistry*, vol. 15, no. 3, pp. 482–490, 2004.

[20] L. R. Hirsch, R. J. Stafford, J. A. Bankson et al., "Nanoshell-mediated near-infrared thermal therapy of tumors under magnetic resonance guidance," *Proceedings of the National Academy of Sciences of the United States of America*, vol. 100, no. 23, pp. 13549–13554, 2003.

[21] G. Scrinis and K. Lyons, "The emerging nano-corporate paradigm: nanotechnology and the transformation of nature, food and agri-food systems," *International Journal of Sociology of Agriculture and Food*, vol. 15, no. 2, pp. 22–44, 2007.

[22] I. Lynch and K. A. Dawson, "Protein-nanoparticle interactions," *Nano Today*, vol. 3, no. 1-2, pp. 40–47, 2008.

[23] I. Lynch, T. Cedervall, M. Lundqvist, C. Cabaleiro-Lago, S. Linse, and K. A. Dawson, "The nanoparticle-protein complex as a biological entity; a complex fluids and surface science challenge for the 21st century," *Advances in Colloid and Interface Science*, vol. 134-135, pp. 167–174, 2007.

[24] P. Ghosh, G. Han, M. De, C. K. Kim, and V. M. Rotello, "Gold nanoparticles in delivery applications," *Advanced Drug Delivery Reviews*, vol. 60, no. 11, pp. 1307–1315, 2008.

[25] A. E. Nel, L. Mädler, D. Velegol et al., "Understanding biophysicochemical interactions at the nano-bio interface," *Nature Materials*, vol. 8, no. 7, pp. 543–557, 2009.

[26] A. Lesniak, F. Fenaroli, M. P. Monopoli, C. Åberg, K. A. Dawson, and A. Salvati, "Effects of the presence or absence of a protein corona on silica nanoparticle uptake and impact on cells," *ACS Nano*, vol. 6, no. 7, pp. 5845–5857, 2012.

[27] L. Lartigue, C. Wilhelm, J. Servais et al., "Nanomagnetic sensing of blood plasma protein interactions with iron oxide nanoparticles: impact on macrophage uptake," *ACS Nano*, vol. 6, no. 3, pp. 2665–2678, 2012.

[28] A. Verma and V. M. Rotello, "Surface recognition of biomacromolecules using nanoparticle receptors," *Chemical Communications*, no. 3, pp. 303–312, 2005.

[29] C. M. McIntosh, E. A. Esposito III, A. K. Boal, J. M. Simard, C. T. Martin, and V. M. Rotello, "Inhibition of DNA transcription using cationic mixed monolayer protected gold clusters," *Journal of the American Chemical Society*, vol. 123, no. 31, pp. 7626–7629, 2001.

[30] M. Thomas and A. M. Klibanov, "Conjugation to gold nanoparticles enhances polyethylenimine's transfer of plasmid dna into mammalian cells," *Proceedings of the National Academy of Sciences of the United States of America*, vol. 100, no. 16, pp. 9138–9143, 2003.

[31] N. O. Fischer, A. Verma, C. M. Goodman, J. M. Simard, and V. M. Rotello, "Reversible "irreversible" inhibition of chymotrypsin using nanoparticle receptors," *Journal of the American Chemical Society*, vol. 125, no. 44, pp. 13387–13391, 2003.

[32] P. Kumari and P. Majewski, "Adsorption of albumin on silica surfaces modified by silver and copper nanoparticles," *Journal of Nanomaterials*, vol. 2013, Article ID 839016, 7 pages, 2013.

[33] S. P. Boulos, T. A. Davis, J. A. Yang et al., "Nanoparticle-protein interactions: a thermodynamic and kinetic study of the adsorption of bovine serum albumin to gold nanoparticle surfaces," *Langmuir*, vol. 29, no. 48, pp. 14984–14996, 2013.

[34] V. Banerjee and K. P. Das, "Interaction of silver nanoparticles with proteins: a characteristic protein concentration dependent profile of SPR signal," *Colloids and Surfaces B: Biointerfaces*, vol. 111, pp. 71–79, 2013.

[35] L. Shang, L. Yang, J. Seiter et al., "Nanoparticles interacting with proteins and cells: a systematic study of protein surface charge effects," *Advanced Materials Interfaces*, vol. 1, no. 2, Article ID 1300079, 2014.

[36] J. Turkevich, P. C. Stevenson, and J. Hillier, "A study of the nucleation and growth processes in the synthesis of colloidal gold," *Discussions of the Faraday Society*, vol. 11, pp. 55–75, 1951.

[37] P. V. Kamat, *Nanoparticles and Nanostructured Films*, John Wiley & Sons, New York, NY, USA, 1998.

[38] K. Saware and A. Venkataraman, "Biosynthesis and characterization of stable silver nanoparticles using *Ficus religiosa* leaf extract: a mechanism perspective," *Journal of Cluster Science*, vol. 25, no. 4, pp. 1157–1171, 2014.

[39] R. Liu, A. Siemiarczuk, and F. J. Sharom, "Intrinsic fluorescence of the P-glycoprotein multidrug transporter: sensitivity of tryptophan residues to binding of drugs and nucleotides," *Biochemistry*, vol. 39, no. 48, pp. 14927–14938, 2000.

[40] S.-H. Huang, M.-H. Liao, and D.-H. Chen, "Direct binding and characterization of lipase onto magnetic nanoparticles," *Biotechnology Progress*, vol. 19, no. 3, pp. 1095–1100, 2003.

[41] J. Deka, A. Paul, and A. Chattopadhyay, "Modulating enzymatic activity in the presence of gold nanoparticles," *RSC Advances*, vol. 2, no. 11, pp. 4736–4745, 2012.

[42] A. Rangnekar, T. K. Sarma, A. K. Singh, J. Deka, A. Ramesh, and A. Chattopadhyay, "Retention of enzymatic activity of α-amylase in the reductive synthesis of gold nanoparticles," *Langmuir*, vol. 23, no. 10, pp. 5700–5706, 2007.

[43] D. Raghunandan, M. D. Bedre, S. Basavaraja, B. Sawle, S. Y. Manjunath, and A. Venkataraman, "Rapid biosynthesis of irregular shaped gold nanoparticles from macerated aqueous extracellular dried clove buds (*Syzygium aromaticum*) solution," *Colloids and Surfaces B: Biointerfaces*, vol. 79, no. 1, pp. 235–240, 2010.

[44] X. P. Zhu, T. Suzuki, T. Nakayama, H. Suematsu, W. Jiang, and K. Niihara, "Underwater laser ablation approach to fabricating monodisperse metallic nanoparticles," *Chemical Physics Letters*, vol. 427, no. 1–3, pp. 127–131, 2006.

[45] N. V. Tarasenko, A. V. Butsen, E. A. Nevar, and N. A. Savastenko, "Synthesis of nanosized particles during laser ablation of gold in water," *Applied Surface Science*, vol. 252, no. 13, pp. 4439–4444, 2006.

[46] F. Mafuné, J.-Y. Kohno, Y. Takeda, and T. Kondow, "Full physical preparation of size-selected gold nanoparticles in solution: laser ablation and laser-induced size control," *Journal of Physical Chemistry B*, vol. 106, no. 31, pp. 7575–7577, 2002.

[47] S. A. R. Abbas, "The effects of gold and silver nanoparticles on choline estrase and Monoamino oxidase enzymes activities," *International Journal of Chemistry*, vol. 3, no. 4, pp. 61–68, 2011.

[48] J. Deka, A. Paul, A. Ramesh, and A. Chattopadhyay, "Probing Au nanoparticle uptake by enzyme following the digestion of a starch-Au-nanoparticle composite," *Langmuir*, vol. 24, no. 18, pp. 9945–9951, 2008.

[49] X. Jiang, J. Jiang, Y. Jin, E. Wang, and S. Dong, "Effect of colloidal gold size on the conformational changes of adsorbed cytochrome *c*: probing by circular dichroism, UV-visible, and infrared spectroscopy," *Biomacromolecules*, vol. 6, no. 1, pp. 46–53, 2005.

[50] A. Gole, C. Dash, C. Soman, S. R. Sainkar, M. Rao, and M. Sastry, "On the preparation, characterization, and enzymatic activity of fungal protease-gold colloid bioconjugates," *Bioconjugate Chemistry*, vol. 12, no. 5, pp. 684–690, 2001.

Hindawi Publishing Corporation
Journal of Nanoparticles
Volume 2015, Article ID 601941, 9 pages
http://dx.doi.org/10.1155/2015/601941

Research Article

Structured Pd/γ-Al_2O_3 Prepared by Washcoated Deposition on a Ceramic Honeycomb for Compressed Natural Gas Applications

Małgorzata Adamowska and Patrick Da Costa

Institut Jean le Rond d'Alembert, Université Pierre et Marie, Curie (UPMC Paris 6), CNRS UMR 7190, 2 Place de la Gare de Ceinture, 78210 Saint Cyr l'Ecole, France

Correspondence should be addressed to Małgorzata Adamowska; malgorzata.adamowska@wp.pl

Received 27 July 2014; Accepted 30 September 2014

Academic Editor: Amir Kajbafvala

The preparation of a coating procedure was studied, from the washcoating with γ-alumina to the deposition of palladium by excess solvent or incipient wetness impregnation. The powder and the washcoat layers were studied by different characterisation techniques such as SEM, BET surface area, and XRD. Vibration-resistance and heat-resistance were also evaluated. It was shown that the alumina layer is quite well deposited on the channel walls (SEM images). However, a detachment of the washcoat layer was observed after ultrasound treatment. It was proved that the monolith Pd impregnation method by incipient wetness impregnation is more efficient. The presence of palladium was confirmed using HRTEM, the palladium was present under the Pd (II) oxidation state, and the size of PdO particles varies between 2.5 and 3.1 nm. The catalytic properties of the monolith catalyst were carried out using temperature programmed surface reaction (TPSR). The efficiency of the procedure of the monolith catalyst preparation was confirmed by comparing the activity of the prepared catalyst with the one of a model catalyst.

1. Introduction

Automobile exhaust constitutes an important source of air pollution. The compounds emitted in the exhaust can be divided into two categories: those that are regulated by law, that is, carbon monoxide (CO), nitrogen oxides (NOx), hydrocarbons (HC), and particulate, and unregulated constituents. The pollutant emissions from road vehicles are regulated separately for light-duty vehicles (cars and light vans) and for heavy-duty vehicles (trucks and buses). European emission standards such as Euro 6 (2014), Euro 6.2 (2017), and Euro 7 (2018) define the acceptable limits for exhaust emissions of new vehicles sold in EU member states [1, 2].

Natural gas (NG) is a favorable alternative automotive fuel due to its availability, low price, high hydrogen to carbon ratio, and lower CO_2 emission compared to conventional fuelled vehicles. However, a major disadvantage of using natural gas is the unburned CH_4 emission (effective greenhouse gas). Therefore, to comply with future legislation, highly efficient catalysts for the complete abatement of the unburned methane are needed [3]. Such catalysts are mainly composed by palladium deposited on typical supports [4].

For such an application in stoechiometric conditions, the use of three-way catalytic converters to minimise air pollution caused by automotive exhaust gases is already well established [5–7] for vehicles fuelled by gasoline. The typical three-way catalysts (TWC) contain noble metals (Pt, Pd, and Rh) deposited together with a washcoat (alumina modified with low loadings of lanthanum or barium and with ca. 10–20 wt.% ceria and zirconia) on a ceramic or metallic monolith [5]. The air/fuel (A/F) ratio is controlled within a narrow operating window, in which both the oxidation of hydrocarbons and carbon monoxide and the reduction of nitrogen oxides are promoted [8, 9]. However, only few studies deal with the use of catalysts used in simulated exhaust gases from CNG (compressed natural gas) vehicles [4, 10–12].

The monolith parts themselves can be produced in a number of sizes and shapes, typically round or oval cross-sectional areas for automotive applications, or square for stationary emission uses [13]. The number of channels, their

diameters, and wall thickness determine the cell density, expressed as cells per square inch (cpsi), which in turn allows the calculation of the geometric surface area which is the sum of the areas of all the channel walls upon which the catalyst is deposited [14].

The most common material for monolithic structures is cordierite, a ceramic material consisting of magnesia, silica, and alumina in the molar ratio of 2 : 5 : 2. Ceramic materials such as cordierite have high mechanical resistance, high melting temperatures (1465°C), and resistance to oxidation and can be made to have excellent thermal shock resistance (low expansion coefficients: $\leq 5 \times 10^{-6}\ K^{-1}$) [14–17]. Nevertheless, the monolithic ceramic catalyst has a low specific surface area (typically $0.7\ g{\cdot}m^{-2}$). This is the reason why a layer of oxide material with a high surface area (e.g., for γ-alumina, typically $200\ g{\cdot}m^{-2}$), called washcoat, is generally coated on the inner walls of the honeycomb support. The slurry coating of different materials was discussed by Addiego et al. [18]. Moreover, the preparation of monolithic catalysts has been reviewed in detail by Nijhuis et al. [19]. Alumina is always chosen because of its high surface area and relatively good thermal stability under hydrothermal conditions of the exhausts. However, it should be noted that γ-alumina can be transformed to α-alumina at high temperature (above 1000°C) which can be encountered in the three-way catalysis. Recrystallization to α-alumina leads to sintering and consequently to a severe drop of the surface area ($10\ g{\cdot}m^{-2}$) [20]. So the γ-alumina should be thermally stabilized by addition of stabilising agents such as lanthanum, barium, strontium, cerium, and, more recently, zirconium oxides [21, 22].

The washcoat is usually applied by impregnation of the honeycomb in slurry of the powder and subsequent drying and calcination. The last step is very important since the calcination binds the washcoat to the monolith walls and is usually done at temperatures of 550°C or higher [15].

The quality of the deposited washcoat depends on the slurry properties such as properties of the solid particles (nature and particle size) [23], properties of the solvent (nature and concentration) [24], and the amount of solids in the slurry [25].

An active element can be incorporated into the layer either during the washcoating step or after the washcoat step, using well-known techniques (wet impregnation, ion exchange, or deposition-precipitation) [19, 26].

In the present work, we first developed a simple procedure leading to a reproducible alumina washcoat. Secondly, we elaborated a procedure of Pd/Al_2O_3/cordierite monoliths preparation. We started our studies using only a Pd active phase to confirm the procedure efficiency by comparing the activity of our catalyst with the one of a model catalyst. The main objective of our work is to develop a new catalyst for natural gas vehicle (GNV) applications which will be more durable (activity stabilisation) and less expensive. So this procedure will be able to design and prepare any catalyst in the laboratory scale in the future. The thermal resistance studies of the new catalyst composition which corresponds to the different ageing processes will be also one of the objectives of our future work. The preliminary studies on the effects of thermal ageing on the structural and textural evolution of γ-alumina and the first correlation between the thermal ageing and a mathematical model have already been published [27].

2. Materials and Methods

2.1. Simple Washcoating Procedure. A commercial monolithic cordierite provided by Corning with a cell density of 400 cpsi was used as the support. The boehmite γ-AlOOH (SASOL DISPAL 23N4-80) was chosen as starting material for the washcoat preparation. The γ-alumina was obtained by the dehydration of γ-AlOOH during calcination. The powder of the starting material was milled to obtain particles of similar size as the macropores in the cordierite and then mixed with the necessary amount of binding agent (20 wt.% of colloidal alumina) and demineralised water in order to prepare the slurry. The slurry stabilization was obtained by nitric acid addition (68 wt.%). This step is not easy because of the complex influence of the acid concentration on the gelation process. Two different processes, namely, surface charging and dissolution, can take place [28].

The monoliths (37 mm length, 23 mm diameter) were dipped vertically into the slurry for 2 minutes. The excess of slurry was shaken out of the monolith and the blocked channels were cleared using pressurized air. Then the monolith was dried horizontally in air while being continuously rotated around its axis. Finally, the monolith was dried at 110°C for 2 hours and calcined at 550°C for 4 hours. This high temperature calcination step permitted to fix the coating to the monolith walls. The monolith was coated again before the calcination step using the same slurry composition. The washcoat loading was determined by weighting.

2.2. Procedure of Monolith Pd Impregnation. The palladium (1 wt.% referred to as the washcoat layer) was incorporated into the layer either by excess solvent impregnation or by incipient wetness impregnation.

In the first case, the aluminium washcoated monolith was dipped into the palladium solution. The impregnation was carried out using an evaporator (60°C, 180 rotations per minute). The wet impregnated monoliths were dried at 110°C for 2 hours and calcined at 550°C for 4 hours in air with a heating rate of $10°C{\cdot}min^{-1}$.

In the second case, the monolith was dipped into the Pd catalyst slurry always using the same washcoating procedure in Section 2.1. Supported Pd catalyst, prepared by incipient wetness impregnation, was employed as starting material for the washcoat preparation. The Pd catalyst precursor was dried at 110°C for 2 hours and calcined at 550°C for 4 hours in air with temperature ramp of $10°C{\cdot}min^{-1}$.

In both cases, an aqueous solution of tetramine palladium nitrate solution ($Pd(NH_3)_4(NO_3)_2$) was used as palladium precursor.

2.3. Physicochemical Characterizations. The powder X-ray diffraction patterns were recorded with a SIEMENS D500 diffractometer using monochromatised CuKα radiation.

Measurements were carried out for 2θ ranging from 10° up to 70°.

The specific surface areas were measured by nitrogen adsorption at −196°C using the multipoint method (Micromeritics ASAP 2010). The samples were previously treated at 110°C under vacuum (2×10^{-3} torr) for 3 hours.

The starting material was milled using a planetary micro mill Pulverisette 7 and the particle size distributions of milled powder were measured by a laser particle size analyzer (ANALYSETTE 22-COMPACT) with a measurement range from 0.3 to 300 μm. The analysis of the scattered light information in the analysette 22 was based on Fraunhofer or Mie theory. A volume distribution based on the equivalent diameter of the laser diffraction was obtained.

The washcoat quality of the coated honeycombs was studied by a JEOL JSM-5510 LV scanning electron microscope (SEM) equipped for EDS (energy dispersive spectroscopy) analysis. SEM images of the alumina washcoats were obtained on pieces cut from monolith after metallization of theses samples under an Au film.

The Pd species were studied by HRTEM on a JEOL-JEM 2011 HR (LaB) device equipped for EDS analysis. During the same analyses, EDS measurements were performed to verify the presence of palladium in the analyzed zone. The interplanar spacing was measured directly on the HRTEM images. The identification of Pd species was realized using JCPDS patterns [29].

Resistance to mechanical vibrations was evaluated using ultrasonic vibrations. A piece of the prepared monolith was treated in an ultrasound water bath (power 220 W, frequency 35 kHz). Finally the sample was dried and weighted. The adhesion properties between the catalyst and ceramic surface were determined by weight loss of the monolith as a function of time. The weight loss of sample after ultrasonic vibration was defined as follows:

$$\Delta W = \left[\frac{(W_1 - W_2)}{W_1} \right] \times 100\%, \quad (1)$$

where W_1 is the washcoat weight before ultrasonic vibration and W_2 is the washcoat weight after ultrasonic vibration.

Resistance to high temperature was studied using a piece of the loaded monolith in order to simulate an ageing process. This ageing process was performed in an oven at 950°C for 4 hours with a heating rate of 10°C·min^{-1} using 10 vol.% of water in air. These conditions correspond to the cracking and detaching state of a layer after using a vehicle for 50000 km.

2.4. Catalytic Activity Tests. The evaluation of the catalytic performance was carried out using temperature programmed surface reaction (TPSR). The TPSR was performed from room temperature (RT) to 570°C with a heating rate of 10°C·min^{-1} using the following gas mixture: 2500 ppm NO, 1700 ppm CH_4, 4800 ppm O_2, 4700 ppm CO, 3400 ppm H_2, 9.25% CO_2, and 18% H_2O which is representative of a real CNG exhaust gases mixture. This composition corresponds to a richness of 1.0005. The hour space velocity (GHSV) was 40,000 h^{-1}.

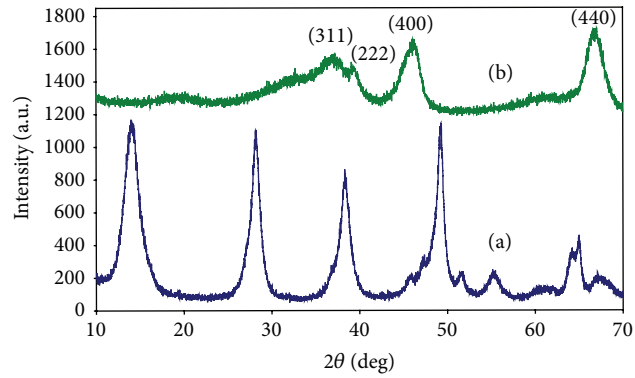

Figure 1: XRD powder patterns of samples: (a) pseudoboehmite and (b) γ-alumina.

To be close to industrial conditions, our apparatus showed a preheater in which the gases are heated up to 790°C. These heated gases flowed through the catalytic bed composed by the monolith sample. Three thermocouples were available to follow the reaction temperature. The first one was placed prior to the catalyst, the second one close to the catalyst, and the third one at the exit of the reactor.

The reactor outflow was analyzed using a set of specific detectors. An Eco Physics NO_x L Chemiluminescence's analyzer (for NO and total NO_x) allowed the simultaneous detection of both NO, NO_2 and NO_x (0–2500 ppm). An IR analyser was used to monitor N_2O and CH_4 (0–2500 ppm). The CO was analyzed by two specific IR analyzers dedicated to low (0–2000 ppm) and high CO concentrations (1–5%). The CO_2 was monitored by Rosemount analytical detector (0–20%).

3. Results and Discussion

3.1. Characterization of Starting Material. The γ-alumina was obtained by the γ-AlOOH dehydration during calcination step. The temperatures at which these transitions have been observed are somewhat variable, apparently dependent on the crystallinity and previous history of the boehmite and on the conditions of heat treatment [30, 31].

The dehydration of γ-AlOOH to γ-Al_2O_3 was realized at 500°C for 4 hours. The XRD patterns of the boehmite and γ-alumina are presented in Figure 1. Some of the peaks of the boehmite sample are broad and well defined (14.3°, 28.3°, 38.5°, 49.3°, and 55.5°). The broad diffraction lines of the boehmite reveal that the crystallites are very small. The boehmite structure corresponds to an orthorhombic unit cell. The boehmite sample was classified as a pseudoboehmite since the peaks are not sharp and intense [32].

The diffraction peaks of the calcined sample (37.3°, 39.6°, 46.2°, and 67°) can be indexed to a face-centered cubic phase of γ-Al_2O_3 (JSPDS n° 00-010-0425). We can observe a decrease of the peak intensity and the appearance of the main peaks characteristic of γ-alumina after pseudoboehmite calcination.

The specific surface area, total pore volume, and mean pore diameter results of the samples are reported in Table 1.

Table 1: BET surface area, total pore volume, and mean pore diameter of the pseudoboehmite and γ-Al_2O_3 (fresh and aged).

Sample	S_{BET} [$m^2 \cdot g^{-1}$]	Total pore volume [$cm^3 \cdot g^{-1}$]	Mean pore diameter [nm]
γ-AlOOH	293	0,35	4,6
γ-Al_2O_3	201	0,42	8,4
γ-Al_2O_3 aged	115	0,43	14,9

Recrystallization to γ-alumina leads to sintering and consequently to a severe drop of boehmite specific surface area. Average pore diameter ranges from 4.6 nm for the boehmite to 8.4 nm for the γ-alumina. Thus, according to the IUPAC classification, the starting materials studied show mesoporosity.

The specific surface area considerably decreased after the hydrothermal ageing process. This phenomenon is explained by water vapour presence which not only accelerates crystallization but also causes structural change in the oxide support [33].

3.2. Washcoating of Cordierite Monolith

3.2.1. γ-Al_2O_3 Coating. The washcoated monolith contains 23 wt.% (134 $g \cdot L^{-1}$) of the alumina layer after two impregnations.

The SEM images (Figures 2(a)-2(b)) of the washcoated monolith, obtained by secondary electrons detection (SEM-SEI images), show that the alumina layer is well deposited on the channel walls and the washcoat is observed in all the corners. However, we can also observe cracks in the coat layer. The cracks in the corners of the channels can be formed most likely because of a difference in thermal expansion between the cordierite and the alumina, while the cracks in the coat layer can be formed during a too fast drying step. Forzatti et al. [34] indicate that the drying step requires a careful control of temperature and moisture and the steps must be slow enough to prevent ruptures and cracks. It is evident that the problem of an inhomogeneous moisture distribution during drying step must be solved in the future studies.

The thickness of the alumina washcoat varies from 25 μm in the middle of the channels up to 85 μm in the corners (Figure 2(b)). The results obtained showed that the washcoat layer is well deposited over the whole channels length. However, the layer thickness is not homogeneous since the chemical elements distribution studied by EDS cartography is not uniform (results not shown). As it was mentioned previously, the main components of the cordierite are Al, Si, and Mg. Some silicon, which is not an element of the washcoat composition, was detected in the middle of some channels suggesting that the layer thickness is less important.

Thermal and mechanical treatments were realized to determine the initial resistance of the prepared catalyst. This information is necessary to develop more resistant catalytic material in the future. Resistance to mechanical vibrations and resistance to high temperature of the alumina washcoat were determined to simulate the conditions occurring in vehicles. The severe conditions (hot exhaust gases of high velocity and mechanical vibrations) can lead to detachment of the washcoat layer. Therefore, the adhesion of the substrate is a very important requirement. This study was carried out for samples before (fresh catalyst) and after ageing process (ageing catalyst). The weight loss curves of the washcoat are shown in Figure 3.

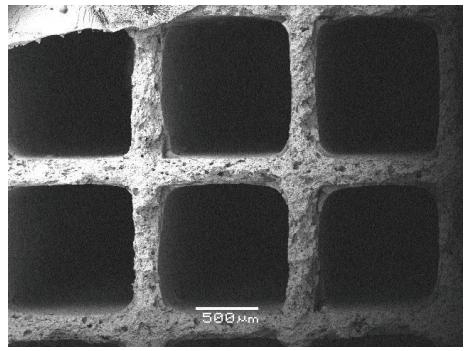

(a)

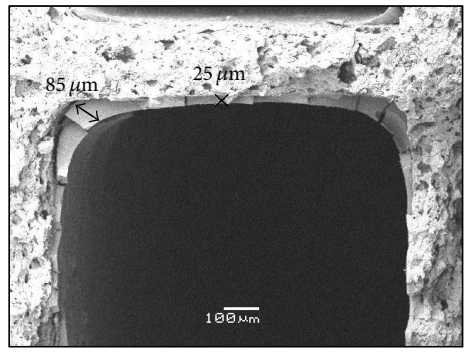

(b)

Figure 2: SEM images of the γ-Al_2O_3 washcoat layer on the cordierite monolith: (a) general view of the monolith piece and (b) view of one channel.

It can be observed that the washcoat exhibits a weight loss in both cases. However, this phenomenon is more significant for the sample exposed to a high temperature treatment. In the case of the fresh catalyst, the washcoat stabilisation is achieved after 2 hours of ultrasound treatment (the total weight loss around 9 wt.%). However, the layer stabilisation of ageing catalyst is observed after 15 hours (the total weight loss around 20 wt.%).

The cracks formation and propagation, as a result of the thermal stress during the drying and the high temperature treatments, have an influence directly on the washcoat detachment [35]. The numerical analysis of the wet body deformation by drying (an increase of the cohesive force, decohesion of the structure) was studied in detail by Kowalski et al. [36, 37].

The present works only show the elaboration of a simple washcoat procedure. However, it will be interesting in the future to modify the γ-alumina coating (Ce, Zr, La, or Ba addition) to improve the washcoat properties toward the thermal stress [20, 25].

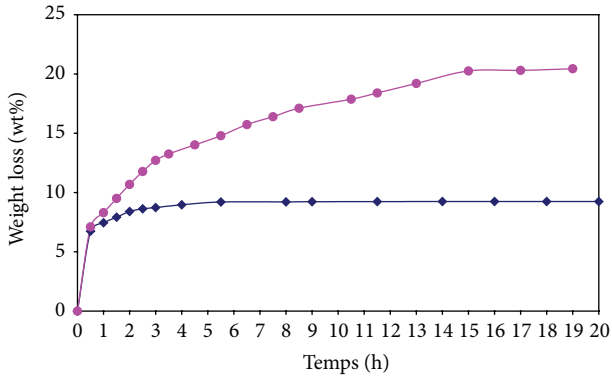

FIGURE 3: Weight loss of washcoat, as function of time (◆: before ageing, ●: after ageing).

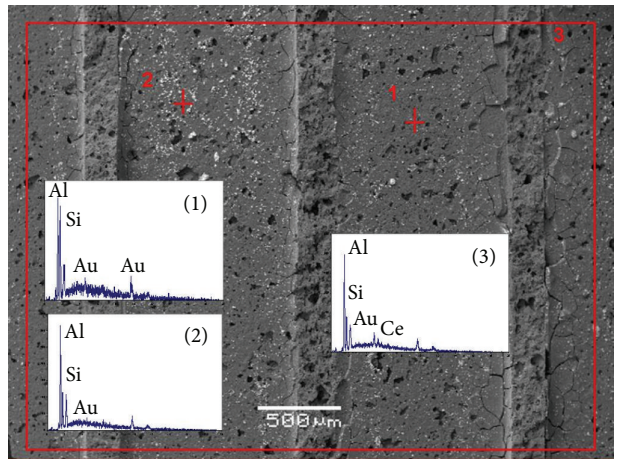

FIGURE 4: Internal surface studies of Pd-impregnated coating (Pd deposited by excess solvent impregnation) by EDS analysis.

3.2.2. Pd Catalyst Coating. The excess solvent impregnation and incipient wetness impregnationwere used to prepare the Pd-impregnated monoliths.

Excess Solvent Impregnation. The alumina washcoated quality was determined by SEM. The results show that the alumina layer is well deposited on the channel walls (results not shown). The efficiency of the Pd impregnation method was determined by EDS analysis.

The different zones were studied to obtain more precise information on the Pd distribution. Figure 4, one of the recorded spectra on the sample surface (different areas), shows the chemical elements present on the channel walls. Only aluminium, silicon, and gold peaks were observed during the EDS analysis. The Pd presence was not confirmed in the analysis zones. It was found that the majority of the palladium was deposited on the external surface of the impregnated monolith (Figure 5). It was concluded that the Pd impregnation of monolith method by excess solvent impregnation is unsuitable.

Incipient Wetness Impregnation. The washcoat quality was determined by SEM. SEM-SEI images (Figure 6) show that the cordierite support is completely covered. The thickness of the alumina washcoat varies from 21 μm in the middle of channel up to 72 μm in the corners. The EDS analysis (Figure 6) confirmed palladium presence on the channel walls. We can conclude that the method of palladium impregnation is efficient. The distribution of the Al and Si elements on the sample surface was determined by cartographies. Figure 6(a) shows that the washcoat layer is well deposited on the external parts of the monolith sample. The presence of silicon in the middle of the channel in the case of the internal part of the monolith sample (Figure 6(b)) indicates that the layer thickness is not homogeneous.

The Pd species was determined by HRTEM (Figure 7). The presence of palladium in each analyzed area was confirmed by EDS analysis. The lattice fringes were measured directly on the image using high magnifications view. The palladium species were then identified using a database of powder diffraction patterns. The results show that palladium is present under the PdO oxidation state and the size of these particles varies between 2.5 and 3.1 nm.

3.3. Catalytic Activity Tests. The commercial honeycomb converter is mainly composed by the palladium oxide (2.55 wt.%) and a small amount of rhodium (0.18 wt.%) and platinum (0.07 wt.%) [4]. Salaün et al. [4] concluded that the palladium is deposited on the alumina whereas rhodium is deposed on the ceria-zirconia.

For CNG applications, methane, which is the major component of natural gas, is the main pollutant. The palladium in PdO form is presented as the more active phase for methane oxidation [4]. In order to evaluate the performance of the washcoating procedure, we prepared a catalyst containing 2.5 wt.% of palladium to compare its activity with a model catalyst which contains the same amount of palladium provided by an international catalyst manufacturer.

In Figure 8, NO_x, CH_4, and CO conversions are reported as a function of the reaction temperature for the prepared (a) and the model (b) Pd monolith catalysts. At low temperatures, we observe the evolution of the NO_x concentration which is correlated to the N_2O formation. This phenomenon is observed for both catalysts; however, the amount of N_2O formed is more important in the case of the model catalyst.

According to the literature [4, 11], at low temperature, NO can be reduced by hydrogen or carbon monoxide, whereas at high temperature the methane is the reducing agent of NO. Salaün et al. [11] investigated the role of CO and H_2 in NO reduction removing the hydrogen or the oxygen from the feed. In absence of H_2, the NO conversion was decreased significantly and the light off temperature was shifted to higher temperature. In absence of CO, the global trends of the plots of NO reduction and CH_4 oxidation were comparable with those obtained for the total gas mixture. These authors showed that the major reducing agent for NO reduction at low temperature is hydrogen.

At low temperature, we can also observe the carbon monoxide conversion which is oxidized by oxygen (Figure 8). Salaün et al. [4] proposed that the CO oxidation and the

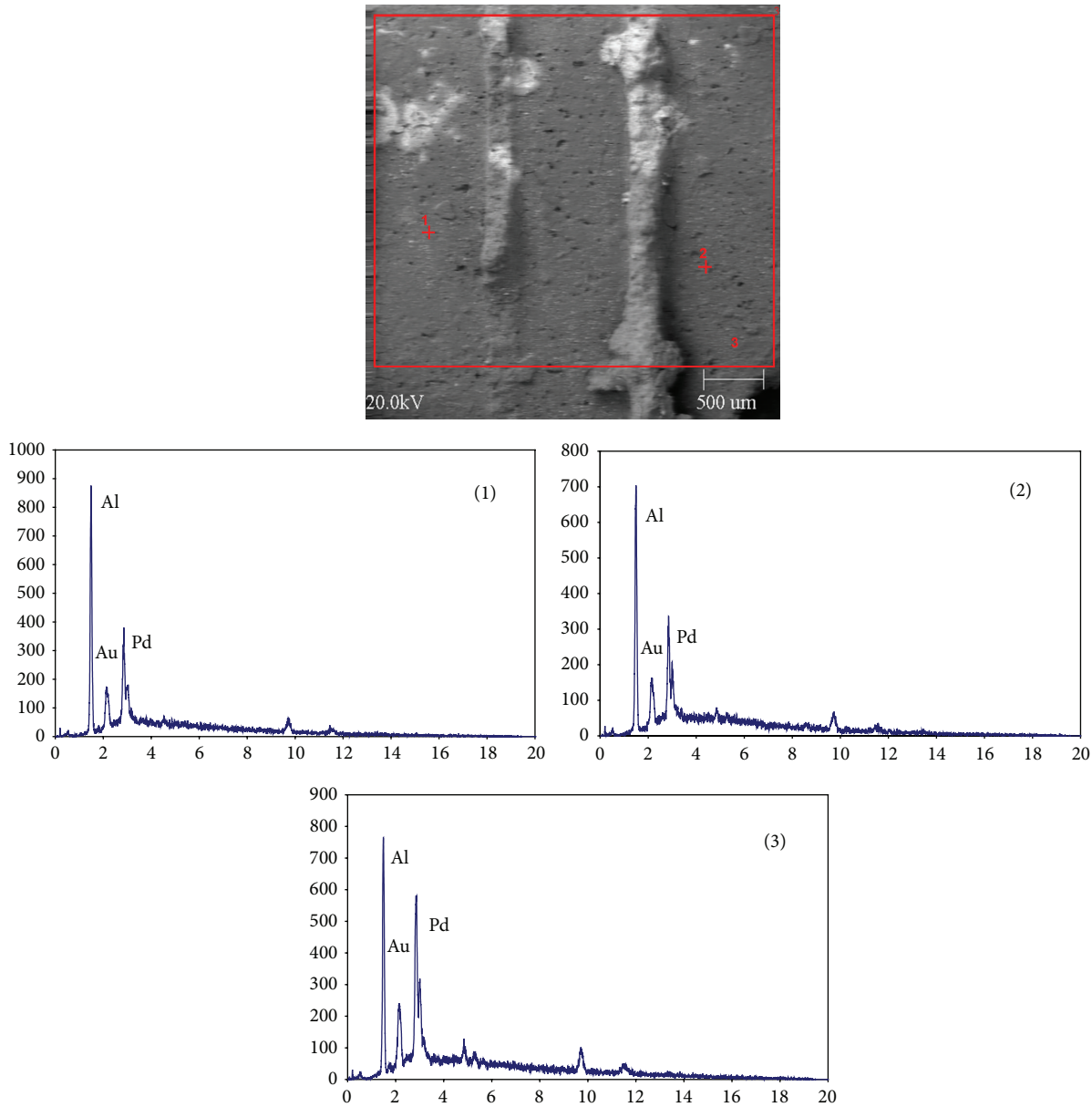

Figure 5: External surface studies of Pd-impregnated coating (Pd deposited by excess solvent impregnation) by EDS analysis.

NO reduction do not take place on the same catalytic site (rhodium and palladium sites, respectively). Furthermore, these authors supposed that a reaction between CO and N_2O (product of NO decomposition or reduction at low temperature) is possible since less N_2O quantity is detected. However, at high temperature, CO could be consumed during the water gas shift reaction. We observed that in the case of the prepared catalyst, the light off temperature is shifted to lower temperature.

At high temperature, we can also observe simultaneously NO_x and CH_4 conversion. The methane is completely converted below 560°C. Salaün et al. [4] showed that the main oxidizing agent of methane is NO. However, these authors suggest that, at high temperature, the steam effects are not negligible. We can observe that the evolution of the methane concentration was the same for model and prepared catalysts. The results obtained show that our catalyst is as good as the model catalyst and that the procedure of our monolith preparation is efficient.

The prepared catalyst is active in the methane oxidation reaction. However, it is evident that its composition must be optimised to reinforce its catalytic action and to stabilise the alumina transformation.

4. Conclusions

The washcoat layer is well deposited on the channel walls and in the corners. However, the layer thickness is not homogeneous. The cracks observed on the coat layer and in the corners of the channels were formed most likely because

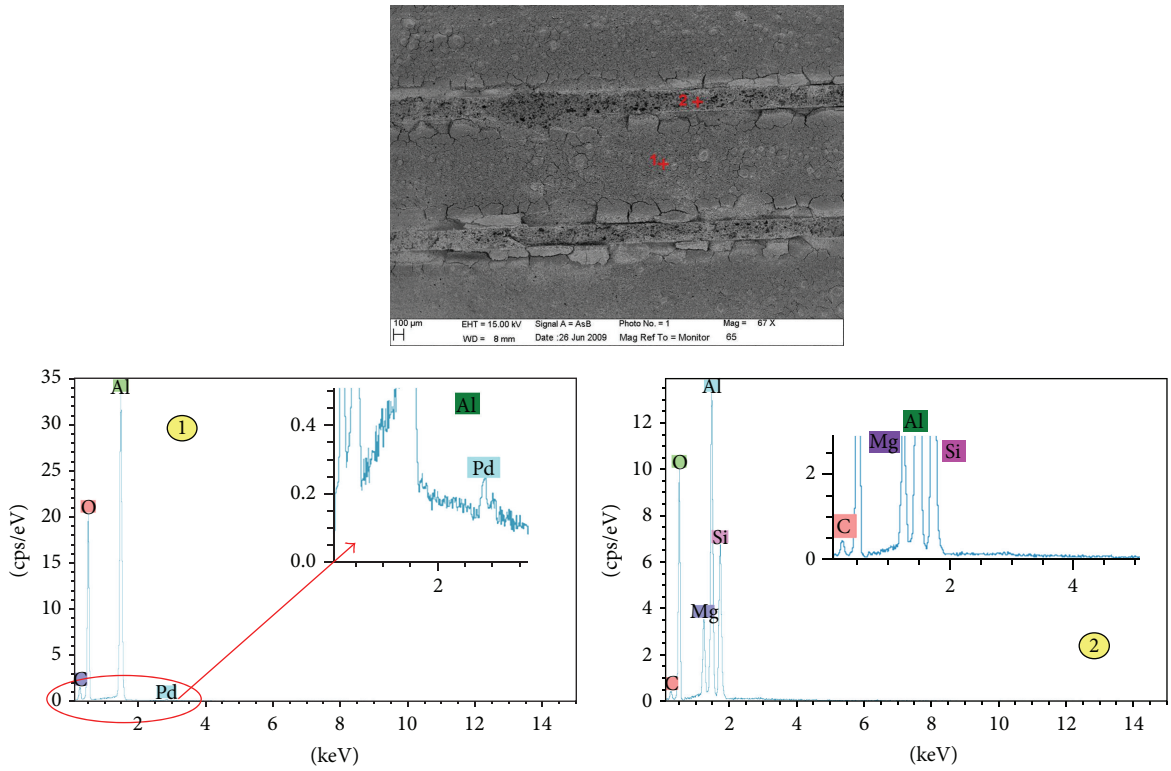

FIGURE 6: EDS analysis of Pd-impregnated coating (Pd deposited by incipient wetness impregnation).

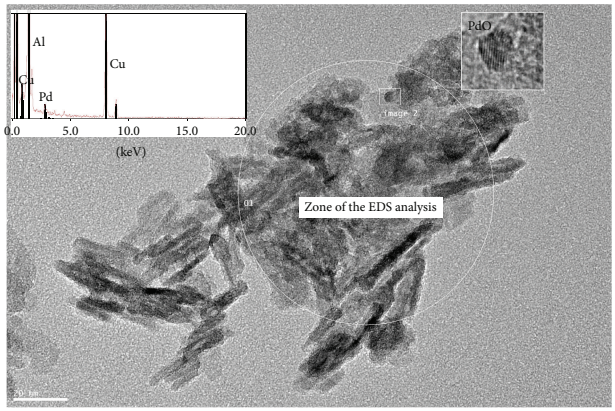

FIGURE 7: Transition electron microscopy of Pd-impregnated monoliths, coupled with EDS spectroscopy.

of a difference in thermal expansion and during a too fast drying step. Obviously, the drying step (temperature and moisture control) has to be optimized.

A detachment of the washcoat layer was observed after ultrasound treatment for fresh and aged catalysts. However, this phenomenon is more significant for the sample exposed to a high temperature treatment. The washcoating procedure must be optimized to increase the coating adhesion.

The Pd impregnation of monolith by incipient wetness impregnation is more efficient than the excess solvent impregnation method. The Pd is present under the Pd (II) oxidation state.

The prepared catalyst is active in the methane oxidation reaction. The results obtained show that our catalyst is as good as the model catalyst and that the procedure of our monolith preparation is efficient.

The main goal of our research is to develop a new catalyst for GNV applications. The know-how of the washcoating procedure allows us to optimize the catalyst composition, such as the active phase and the stabilizing agent of alumina. The objective is to improve the catalytic performance and to decrease the price of the catalyst. This monolithic catalyst will be also applied for the methane oxidation and the selective catalytic reduction of NO_x by methane.

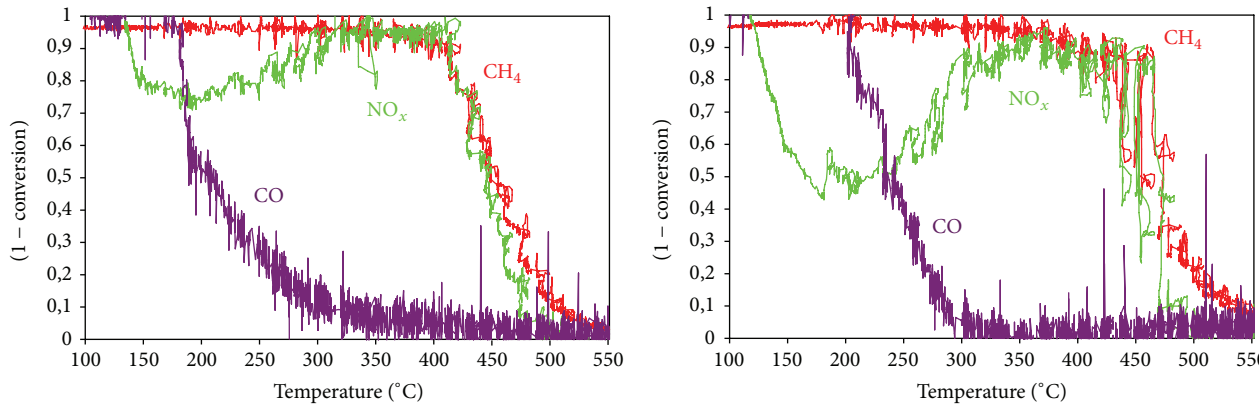

FIGURE 8: TPSR profile of NO_x, CH_4, and CO for (a) prepared catalyst and (b) model catalyst. Feed gas: 2500 ppm NO, 1700 ppm CH_4, 4800 ppm O_2, 4700 ppm CO, 3400 ppm H_2, 9.25% CO_2, and 18% H_2O and balance N_2 (GHSV 40,000 h^{-1}).

Conflict of Interests

The authors declare that there is no conflict of interests regarding the publication of this paper.

Acknowledgments

This study was carried out in the framework of ANR CARAVELLE. The authors are grateful to ADEME for the financial support and Mrs. Sandra Casale and M. Stéphane Borenstein for TEM and SEM studies.

References

[1] P. Bielaczyc, J. Woodburn, and A. Szczotka, "An assessment of regulated emissions and CO_2 emissions from a European light-duty CNG-fueled vehicle in the context of Euro 6 emissions regulations," *Applied Energy*, vol. 117, pp. 134–141, 2014.

[2] G. A. Rhys-Tyler, W. Legassick, and M. C. Bell, "The significance of vehicle emissions standards for levels of exhaust pollution from light vehicles in an urban area," *Atmospheric Environment*, vol. 45, no. 19, pp. 3286–3293, 2011.

[3] A. M. Venezia, G. di Carlo, G. Pantaleo, L. F. Liotta, G. Melaet, and N. Kruse, "Oxidation of CH_4 over Pd supported on TiO_2-doped SiO_2: effect of Ti(IV) loading and influence of SO_2," *Applied Catalysis B: Environmental*, vol. 88, no. 3-4, pp. 430–437, 2009.

[4] M. Salaün, A. Kouakou, S. da Costa, and P. da Costa, "Synthetic gas bench study of a natural gas vehicle commercial catalyst in monolithic form: on the effect of gas composition," *Applied Catalysis B: Environmental*, vol. 88, no. 3-4, pp. 386–397, 2009.

[5] J. K. Hochmuth, K. Wassermann, and R. J. Farrauto, "Car exhaust cleaning," in *Reference Module in Chemistry, Molecular Sciences and Chemical Engineering*, vol. 7 of *Comprehensive Inorganic Chemistry*, pp. 505–523, 2013.

[6] K. A. Subramanian, V. C. Mathad, V. K. Vijay, and P. M. V. Subbarao, "Comparative evaluation of emission and fuel economy of an automotive spark ignition vehicle fuelled with methane enriched biogas and CNG using chassis dynamometer," *Applied Energy*, vol. 105, pp. 17–29, 2013.

[7] G. Karavalakis, M. Hajbabaei, T. D. Durbin, K. C. Johnson, Z. Zheng, and W. J. Miller, "The effect of natural gas composition on the regulated emissions, gaseous toxic pollutants, and ultrafine particle number emissions from a refuse hauler vehicle," *Energy*, vol. 50, no. 1, pp. 280–291, 2013.

[8] M. Shelef and H. S. Gandhi, "Ammonia formation in catalytic reduction of nitric oxide by molecular hydrogen: II. Noble metal catalysts," *Industrial & Engineering Chemistry Product Research and Development*, vol. 11, no. 4, pp. 393–396, 1972.

[9] Y.-F. Y. Yao, "The oxidation of CO and hydrocarbons over noble metal catalysts," *Journal of Catalysis*, vol. 87, no. 1, pp. 152–162, 1984.

[10] P. da Costa, M. Salaün, G. Djéga-Mariadassou, S. da Costa, and G. Brecq, "Comparative study of natural gas vehicles commercial catalysts in monolithic form," SAE Technical Paper 2007-01-0039, 2007.

[11] M. Salaün, S. Capela, S. Da Costa, L. Gagnepain, and P. Da Costa, "Enhancement of 3-way CNG catalyst performance at high temperature due to the presence of water in the feed: on the role of steam reforming of methane and on the influence of ageing," *Topics in Catalysis*, vol. 52, no. 13–20, pp. 1972–1976, 2009.

[12] M. Adamowska, V. Lauga, and P. da Costa, "Elaboration of an accelerated oven CNG heavy duty vehicles catalyst ageing for road ageing simulation," *Topics in Catalysis*, vol. 56, no. 1–8, pp. 267–272, 2013.

[13] J. L. Williams, "Monolith structures, materials, properties and uses," *Catalysis Today*, vol. 69, no. 1–4, pp. 3–9, 2001.

[14] R. M. Heck, S. Gulati, and R. J. Farrauto, "The application of monoliths for gas phase catalytic reactions," *Chemical Engineering Journal*, vol. 82, no. 1–3, pp. 149–156, 2001.

[15] A. Pedro, M. Montes, and E. E. Miró, "Monolithic reactors for environmental applications: a review on preparation technologies," *Chemical Engineering Journal*, vol. 109, no. 1, pp. 11–36, 2005.

[16] M. Valáškováa, J. Zdrálkováa, J. Tokarskýa, G. Simha Martynkováa, M. Ritzc, and S. Študentová, "Structural characteristics of cordierite/steatite ceramics sintered from mixtures containing pore-forming organovermiculite," *Ceramics International*, vol. 40, pp. 15717–15725, 2014.

[17] T. Zhou, L. Li, J. Cheng, and Z. Hao, "Preparation of binary washcoat deposited on cordierite substrate for catalytic applications," *Ceramics International*, vol. 36, no. 2, pp. 529–534, 2010.

[18] W. P. Addiego, I. M. Lachman, M. D. Patil, J. L. Williams, and K. E. Zaun, "High surface area washcoated substrate and method for producing same," US Patent 5,212,130, 1993.

[19] T. A. Nijhuis, A. E. W. Beers, T. Vergunst, I. Hoek, F. Kapteijn, and J. A. Moulijn, "Preparation of monolithic catalysts," *Catalysis Reviews: Science and Engineering*, vol. 43, no. 4, pp. 345–380, 2001.

[20] J. Kašpar, P. Fornasiero, and N. Hickey, "Automotive catalytic converters: current status and some perspectives," *Catalysis Today*, vol. 77, no. 4, pp. 419–449, 2003.

[21] P. Alphonse and B. Faure, "Thermal stabilization of alumina modified by lanthanum," *Microporous and Mesoporous Materials*, vol. 196, pp. 191–198, 2014.

[22] H. Firouzghalb and C. Falamaki, "Fabrication of asymmetric alumina membranes: I. Effect of SrO addition on thermal stabilization of transition aluminas," *Materials Science and Engineering B*, vol. 166, no. 2, pp. 163–169, 2010.

[23] C. Agrafiotis and A. Tsetsekou, "The effect of powder characteristics on washcoat quality. Part I: alumina washcoats," *Journal of the European Ceramic Society*, vol. 20, no. 7, pp. 815–824, 2000.

[24] C. Agrafiotis and A. Tsetsekou, "The effect of processing parameters on the properties of γ-alumina washcoats deposited on ceramic honeycombs," *Journal of Materials Science*, vol. 35, no. 4, pp. 951–960, 2000.

[25] P. Jiang, G. Lu, Y. Guo, S. Zhang, and X. Wang, "Preparation and properties of a γ-Al_2O_3 washcoat deposited on a ceramic honeycomb," *Surface and Coatings Technology*, vol. 190, no. 2-3, pp. 314–320, 2005.

[26] M. Campanati, G. Fornasari, and A. Vaccari, "Fundamentals in the preparation of heterogeneous catalysts," *Catalysis Today*, vol. 77, no. 4, pp. 299–314, 2003.

[27] M. Adamowska, O. Haddad, D. Leguillon, and P. Da Costa, "On the comprehension of mechanical, thermal and chemical evolution of exhaust gases aftertreatment catalysts," *Materials Science Forum*, vol. 783-786, pp. 1979–1985, 2014.

[28] C. Cristiani, M. Valentini, M. Merazzi, S. Neglia, and P. Forzatti, "Effect of ageing time on chemical and rheological evolution in γ-Al_2O_3 slurries for dip-coating," *Catalysis Today*, vol. 105, no. 3-4, pp. 492–498, 2005.

[29] JCPDS patterns of PdO (00-041-1107,00-043-1024).

[30] S. J. Wilson, "The dehydration of boehmite, γ-AlOOH, to γ-Al_2O_3," *Journal of Solid State Chemistry*, vol. 30, no. 2, pp. 247–255, 1979.

[31] X. Krokidis, P. Raybaud, A.-E. Gobichon, B. Rebours, P. Euzen, and H. Toulhoat, "Theoretical study of the dehydration process of boehmite to γ-alumina," *The Journal of Physical Chemistry B*, vol. 105, no. 22, pp. 5121–5130, 2001.

[32] P. de Souza Santos, A. C. V. Coelho, H. de Souza Santos, and P. K. Kiyohara, "Hydrothermal synthesis of well-crystallised boehmite crystals of various shapes," *Materials Research*, vol. 12, no. 4, pp. 437–445, 2009.

[33] A. Kalantar Neyestanaki, F. Klingstedt, T. Salmi, and D. Y. Murzin, "Deactivation of postcombustion catalysts, a review," *Fuel*, vol. 83, no. 4-5, pp. 395–408, 2004.

[34] P. Forzatti, D. Ballardini, and L. Sighicelli, "Preparation and characterization of extruded monolithic ceramic catalysts," *Catalysis Today*, vol. 41, no. 1–3, pp. 87–94, 1998.

[35] T. Defraeye, "Advanced computational modelling for drying process—a review," *Applied Energy*, vol. 131, pp. 323–344, 2014.

[36] S. J. Kowalski, K. Rajewska, and A. Rybicki, "Destruction of wet materials by drying," *Chemical Engineering Science*, vol. 55, no. 23, pp. 5755–5762, 2000.

[37] S. J. Kowalski and C. Strumłło, "Moisture transport, thermodynamics, and boundary conditions in porous materials in presence of mechanical stresses," *Chemical Engineering Science*, vol. 52, no. 7, pp. 1141–1150, 1997.

Hindawi Publishing Corporation
Journal of Nanoparticles
Volume 2014, Article ID 893459, 15 pages
http://dx.doi.org/10.1155/2014/893459

Research Article

Plasmonic and Thermooptical Properties of Spherical Metallic Nanoparticles for Their Thermoplasmonic and Photonic Applications

Victor K. Pustovalov,[1] Liudmila G. Astafyeva,[2] and Wolfgang Fritzsche[3]

[1] *Belarusian National Technical University, Nezavisimosti Prospect 65, 220013 Minsk, Belarus*
[2] *B.I. Stepanov Institute of Physics, National Academy of Sciences of Belarus, Nezavisimosti Prospect 68, 220072 Minsk, Belarus*
[3] *Leibniz Institute of Photonic Technology, 07702 Jena, Germany*

Correspondence should be addressed to Victor K. Pustovalov; pustovalovv@mail.ru
and Wolfgang Fritzsche; fritzsche@ipht-jena.de

Received 15 July 2014; Accepted 3 August 2014; Published 14 October 2014

Academic Editor: Amir Kajbafvala

Investigations and use of nanoparticles (NPs) as photothermal (PT) agents in laser and optical nanotechnology are fast growing areas of research and applications. The potential benefits of NPs applications include possibility for thermal imaging and treatment of materials containing of NPs, applications of NPs for light-to-thermal energy conversion, in catalysis, laser nanomedicine, and chemistry. Efficiency of applications of metallic NPs for laser and optical nanotechnology depends on plasmonic and thermophysical properties of NPs, characteristics of radiation, and surrounding medium. Here we present the results of comparative analysis of NP properties (plasmonic, thermooptical, and others) allowing selecting their parameters for thermoplasmonic and photonic applications. Plasmonic and thermooptical properties of several metallic (aurum, silver, platinum, cobalt, zinc, nickel, titanium, cuprum, aluminum, molybdenum, vanadium, and palladium) NPs are theoretically investigated and analysis of them is carried out. Investigation of the influence of NPs parameters (type of metal, radii, optical indexes, density, and heat capacity of NP material), characteristics of radiation (wavelength and pulse duration), and ambient parameters on plasmonic and thermophysical properties of NPs has been carried out. It was established that maximum value of thermooptical parameter (maximum NP temperature) can be achieved with the use of absorption efficiency factor of NP smaller than its maximum value.

1. Introduction

Recent advances in photothermal nanotechnology based on the use of nanoparticles (NPs) and optical (laser) radiation have been demonstrated for their great potential. In recent years, the laser-NP interaction, absorption, and scattering of radiation energy by NP have become of great interest and an increasingly important for topic in photonic and laser nanotechnology [1–27] (also see the references in these papers). There are many reasons for this interest including application of NPs in different fields, such as catalysis [1, 2], laser nanobiomedicine [3–11], nanooptics and nanoelectronics [12–15], laser processing of metallic NPs in nanotechnology [16–23], and light-to-heat conversion [24–27].

Most of these technologies rely on the position and strength of the surface plasmon on a nanosphere and the fact that NP will absorb and scatter radiation energy well at resonance wavelength. Successful applications of NPs in photonics and thermoplasmonics are based on appropriate plasmonic and optical properties of NPs. High absorption of radiation by NPs can be used for conversion of absorbed energy into NP thermal energy, heating of NP itself and ambient medium, and following photothermal phenomena in laser and optical nanotechnology and nanomedicine. High scattering of radiation is essential for optical diagnostics and imaging applications based on light scattering.

Metallic NPs are mostly interesting for different nanotechnologies among other NPs. First investigations of optical

properties of metallic NPs were carried out in [28, 29]. The attempts to search for the "ideal" plasmonic NPs were carried out in many papers. Optical absorption efficiency of some metallic NPs was investigated in [28–33]. Thermooptical analysis and selection of the properties of gold NPs for laser applications in nanotechnology were carried out in [8, 26, 34]. Searching for better plasmonic materials (metals) was carried out in [13, 32, 35, 36] based on investigations of quality factors of each metal. Different metallic NPs (gold, silver, platinum, zinc, etc.) were used in [1–36]. Gold and silver NPs were considered as the most appropriate ones and widely used in experiments. Methods of chemical synthesis of metallic NPs have been developed and presented in [37–39].

On the other side, a comparative analysis of optimal parameters of different metallic NPs for using them as PT agents in thermoplasmonics and laser nanotechnology is still missing. Here we propose the results for analysis of the NP properties for their photonic and thermoplasmonic applications.

Plasmonic and thermooptical properties of metallic NPs were theoretically investigated and compared in this paper based on computer modeling. We carry out complex investigation of the plasmonic and thermooptical properties of spherical metallic NPs for their interaction with optical (laser) radiation placed (embedded) in some ambient medium. We investigated the influence of the parameters of radiation, NP, and ambient medium on the properties of this interaction.

2. Plasmonic and Thermooptical Parameters of Nanoparticles

Among different characteristics of NPs, laser radiation, and ambient medium that will determine NP plasmonic and thermooptical properties we can note the following ones:

(1) laser (optical) radiation—(a) pulse duration t_P, (b) wavelength λ, and (c) radiation (laser) exposure (energy density) E_0, intensity $I_0 = E_0/t_P$;

(2) spherical nanoparticle—(a) type of NP metal with its values of density ρ_0, heat capacity c_0, optical indexes of refraction $n_{0\lambda}$, and absorption $\chi_{0\lambda}$ of NP metal and (b) NP radius r_0;

(3) nonabsorbing surrounding medium—(a) coefficient of thermal conductivity k_∞ = const and (b) optical indexes of refraction n_λ.

Consider the parameters that characterize the transformation of radiation energy in the processes of NP-radiation interaction.

Efficiency factors of absorption K_{abs}, scattering K_{sca}, and extinction K_{ext} of radiation by NP [29] determine the optical properties of NP.

Parameter P_1 describes the correlation between absorption and scattering of radiation by NP. Parameter P_1 characterizes the contribution of the processes of absorption and scattering to the general energy balance of the NP:

$$P_1 = \frac{K_{\text{abs}}}{K_{\text{sca}}}. \tag{1}$$

The efficiency factor of absorption of laser radiation by NPs K_{abs} can be greater or smaller than the factor of scattering of radiation by NP K_{sca} in the cases of predominant role of absorption or scattering in the process of radiation interaction with NP:

$$K_{\text{abs}} > K_{\text{sca}}, \qquad P_1 > 1, \tag{2a}$$

$$K_{\text{abs}} < K_{\text{sca}}, \qquad P_1 < 1. \tag{2b}$$

The parameter $\Delta T_0/E_0$ [6–8] can be used for determination of thermooptical properties of NPs

$$\frac{\Delta T_0}{E_0} = \frac{K_{\text{abs}} r_0}{4 k_\infty t_P}\left[1 - \exp\left(-\frac{t_P}{\tau_0}\right)\right], \tag{3}$$

$\tau_0 = \rho_0 c_0 {r_0}^2/3k_\infty$—characteristic time for heating and cooling of NP. This parameter determines the increase of NP temperature $\Delta T_0 = T_{\max} - T_\infty$ under action of radiation energy density with value $E_0 = 1\,\text{J/cm}^2$, $T_{\max}$, maximum temperature of NP at $t = t_P$, and T_∞, initial NP temperature.

Parameter $\Delta T_0/E_0$ (3) may be viewed as NP heating efficiency under action of radiation energy with energy density E_0. For $t_P < \tau_0$ and $t_P > \tau_0$ the parameter $\Delta T_0/E_0$ will be approximately determined by the following (see (3)):

$$t_P < \tau_0, \quad \frac{\Delta T_0}{E_0} \approx \frac{3K_{\text{abs}}}{4\rho_0 c_0 r_0}, \tag{4a}$$

$$t_P > \tau_0, \quad \frac{\Delta T_0}{E_0} \approx \frac{K_{\text{abs}} r_0}{4 k_\infty t_P}. \tag{4b}$$

In general, the parameter $\Delta T_0/E_0$ ((3), (4a), and (4b)) depends on characteristics of radiation, λ and t_P, metallic NP, $K_{\text{abs}}(\lambda)$, r_0, c_0, and ρ_0, and ambient medium, k_∞, index of medium refraction n_λ. Combinations $K_{\text{abs}}(r_0)/r_0$ and $K_{\text{abs}}(r_0)r_0$ in (4a) and (4b) determine the range of radii r_0 appropriate for the achievement of the maximum value of T_0 under a fixed value of λ, $K_{\text{abs}}(\lambda)$. The combination $1/c_0\rho_0$ determines the influence of NP metal properties on the maximum value of T_0. Values of k_∞ and n_λ determine the influence of surrounding medium on thermooptical properties of NPs. The parameter of $\Delta T_0/E_0$ does not depend on parameters of radiation (t_P) and ambience (k_∞) in (4a). The selection of mentioned parameters in (3), (4a), and (4b) can provide maximum values ΔT_0 for concrete values of E_0.

We will investigate the influence of all characteristics of NPs, laser radiation, and ambient medium mentioned above on plasmonic and thermooptical properties of metallic NPs. Comparative analysis of the properties of metallic NPs and their efficiency for photonic applications in nanotechnology

have to use the following set of plasmonic and thermooptical parameters of the laser-NP interaction processes:

(i) efficiency factors of absorption K_{abs}, scattering K_{sca}, and extinction K_{ext} of radiation by spherical NP;

(ii) parameter of P_1 (1);

(iii) parameter $\Delta T_0/E_0$ ((3), (4a), and (4b)).

3. Plasmonic and Thermooptical Properties of NPs

Calculations and analysis of plasmonic and thermooptical properties of NPs have been carried out in our investigations. We numerically calculated efficiency factors of absorption K_{abs}, scattering K_{sca}, and extinction K_{ext} of radiation with wavelength λ by spherical homogeneous metallic NP based on generalized Mie theory [29]. Values of optical indexes of refraction and absorption of metals and surrounding media were used from [40–42]. After that, we use (1) and (3) for calculation of the parameters P_1 and $\Delta T_0/E_0$. All figures presented describe the dependences of efficiency factors of absorption K_{abs}, scattering K_{sca}, and extinction K_{ext}, parameters P_1 and $\Delta T_0/E_0$ for metallic NPs on wavelength of radiation, NP radii, pulse duration t_P, and characteristics of surrounding media. Simultaneous comparative investigation of the dependences of K_{abs}, K_{sca}, K_{ext}, and $\Delta T_0/E_0$ on λ, r_0, and other characteristics is very complex and hard task. We have divided this task into two steps. A first step is the calculation and investigation of the dependences of K_{abs}, K_{sca}, K_{ext}, P_1, and $\Delta T_0/E_0$ on λ for some fixed values of r_0, t_P, and selected NP metal and surrounding medium. Second one is the investigation of the dependences of K_{abs}, K_{sca}, K_{ext}, P_1, and $\Delta T_0/E_0$ on r_0 for some fixed values of λ, t_P, and selected NP metal and surrounding medium. This allows investigating complex task step by step and present clear dependences of K_{abs}, K_{sca}, K_{ext}, P_1, and $\Delta T_0/E_0$ on one parameter when other parameters are constant. Figures 1–7 present the dependences of K_{abs}, K_{sca}, K_{ext}, P_1, and $\Delta T_0/E_0$ on λ, r_0, t_P, and optical indexes of metals and surrounding media.

The heat flow from NP, placed in liquids, amorphous solids, and so forth, can be well described by the diffusive heat equation, when mean free path of heat transporter (molecule, etc.) is very short, like $\sim 10^{-8}$ cm in mentioned media [43, 44], and this one is much smaller than characteristic NP radii of r_0 ~10–100 nm. In gases at atmospheric pressure the mean free path of molecules is about $\sim 10^{-5}$ cm and diffusive heat equation can be applied to the heat exchange of NP with gaseous medium for $r_0 \geq 100$ nm. Methods of kinetic equation or molecular dynamics should be used for the description of heat exchange of NP in this case. But during ultrashort laser pulse action with $t_P \sim 10^{-10}$–10^{-12} s on NP we can neglect NP heat exchange with surrounding gas during laser action and calculate parameter $\Delta T_0/E_0$ for $t_P = 1 \times 10^{-12}$ s using (4a). The dependence $\Delta T_0/E_0(\lambda)$ for $t_P \sim 1 \times 10^{-10}$ s practically coincides with this one for $t_P = 1 \cdot 10^{-12}$ s and only one dependence $\Delta T_0/E_0(\lambda)$ is presented in Figures 1–6 for ambient air and $t_P = 1 \cdot 10^{-12}$ s. We can note that the values of $\Delta T_0/E_0$ for $t_P \sim 10^{-12}$ s can be used as upper boundaries of NP heating ($\Delta T_0 = T_{max} - T_\infty$) without NP heat exchange.

The positions of maximum values of efficiency factors of K_{abs}^{max}, K_{sca}^{max}, and K_{ext}^{max} on λ axis are denoted in Figures 1–6 by different vertical lines and locations λ_{abs}^{max} of maximum value of absorption factor K_{abs}^{max} on axis λ are denoted by solid lines, K_{sca}^{max}, dashed lines, and λ_{sca}^{max}, K_{ext}^{max}, dashed-dotted lines, and λ_{ext}^{max} in the case of different values of λ_{abs}^{max}, λ_{sca}^{max}, and λ_{ext}^{max}. In the case of equal values of λ_{abs}^{max}, λ_{sca}^{max}, and λ_{ext}^{max} the location of coincident values of K_{abs}^{max}, K_{sca}^{max}, and K_{ext}^{max} is denoted by solid lines. In some cases additional solid lines denote the locations of the formation of new maximums of efficiency factors (see Figures 3(c), 3(g)) or the points of sharp bend of the dependence of K_{abs} on λ (see Figures 4(i) and 4(j)). Horizontal dashed lines in Figures 1(d), 1(h), 1(l)–6(d), 6(h), and 6(l) denote the value of $P_1 = 1$.

Figures 1–3 present the dependences of efficiency factors of K_{abs}, K_{sca}, and K_{ext} of radiation, parameters $\Delta T_0/E_0$ for $t_P = 1 \cdot 10^{-8}$, $1 \cdot 10^{-12}$ s, and P_1 for homogeneous metallic Au (Figure 1), Ag (Figure 2), and Pt (Figure 3) NPs with radii $r_0 = 10$, 25, and 50 nm on wavelengths λ. NPs are placed in silica, water, and air ambient nonabsorbing media. Optical constants (indexes of refraction n_λ and absorption λ) are changed in the ranges for silica $n_\lambda \approx 1.51 - 1.45$, water $n_\lambda \approx 1.39 - 1.33$, air $n_\lambda \approx 1.0$, and $\varkappa_\lambda \approx 0$ for all ambiences with increasing wavelength λ in the spectral interval ~200–1000 nm.

The dependences of efficiency factors of K_{abs}, K_{sca}, and K_{ext} on λ for fixed values of r_0 have complicated forms. Values of K_{abs}^{max} are placed at $\lambda_{abs}^{max} \sim 510$–$530$ nm for Au NPs and $\lambda_{abs}^{max} \sim 380$–$410$ nm for Ag NPs for $r_0 = 10$, 25, and 50 nm and different ambiences. Consequently the absorption of radiation is determined by plasmon resonances of silver and gold NPs in the field of electromagnetic (laser) radiation. Values of K_{abs} are decreased in UV and NIR spectral intervals out of plasmon wavelengths and especially for Ag NPs these values undergo sharp decrease up to 10^2-10^3 times. We can note a slight decrease of K_{abs} for Au NP in the UV spectral interval in comparison with NIR spectral interval. The behavior of dependences of K_{sca} on wavelength λ is analogous for the dependence of $K_{abs}(\lambda)$. Maximum value of K_{sca}^{max} for Ag NPs achieves $K_{sca} \sim 11 \div 15$ in the interval of $\lambda \sim 410 \div 430$ nm and $r_0 = 25$ nm. Dependence of K_{ext} on λ presents itself the sum of the dependences of $K_{abs}(\lambda)$ and $K_{sca}(\lambda)$. The values of K_{abs}^{max} and K_{ext}^{max} for Au, Pt NPs for $r_0 = 10$ and 25 nm and for Ag NPs $r_0 = 10$ nm practically coincide with each other and for different ambiences (see Figures 1–3). But for $r_0 = 50$ nm values of K_{sca}^{max} and K_{ext}^{max} are greater than K_{abs}^{max}. This fact was also noted in [31]. An increase of r_0 may lead to increase or decrease of the maximum values of K_{abs}, K_{sca}, and K_{ext}. Coincidence of different vertical lines in figures means the coincidence of corresponding values of optical parameters. Placements of K_{ext} at $\lambda \sim 292$ nm and 443 nm for NPs in water for $r_0 = 25$ and 50 nm quantitatively coincide with experimental data [45].

Placements of maximum values of K_{abs}, K_{sca}, and K_{ext} on axis λ can be different in some cases (Figures 1(c), 1(g), 1(k)–3(c), 3(g), and 3(k)). The formation of additional maximums

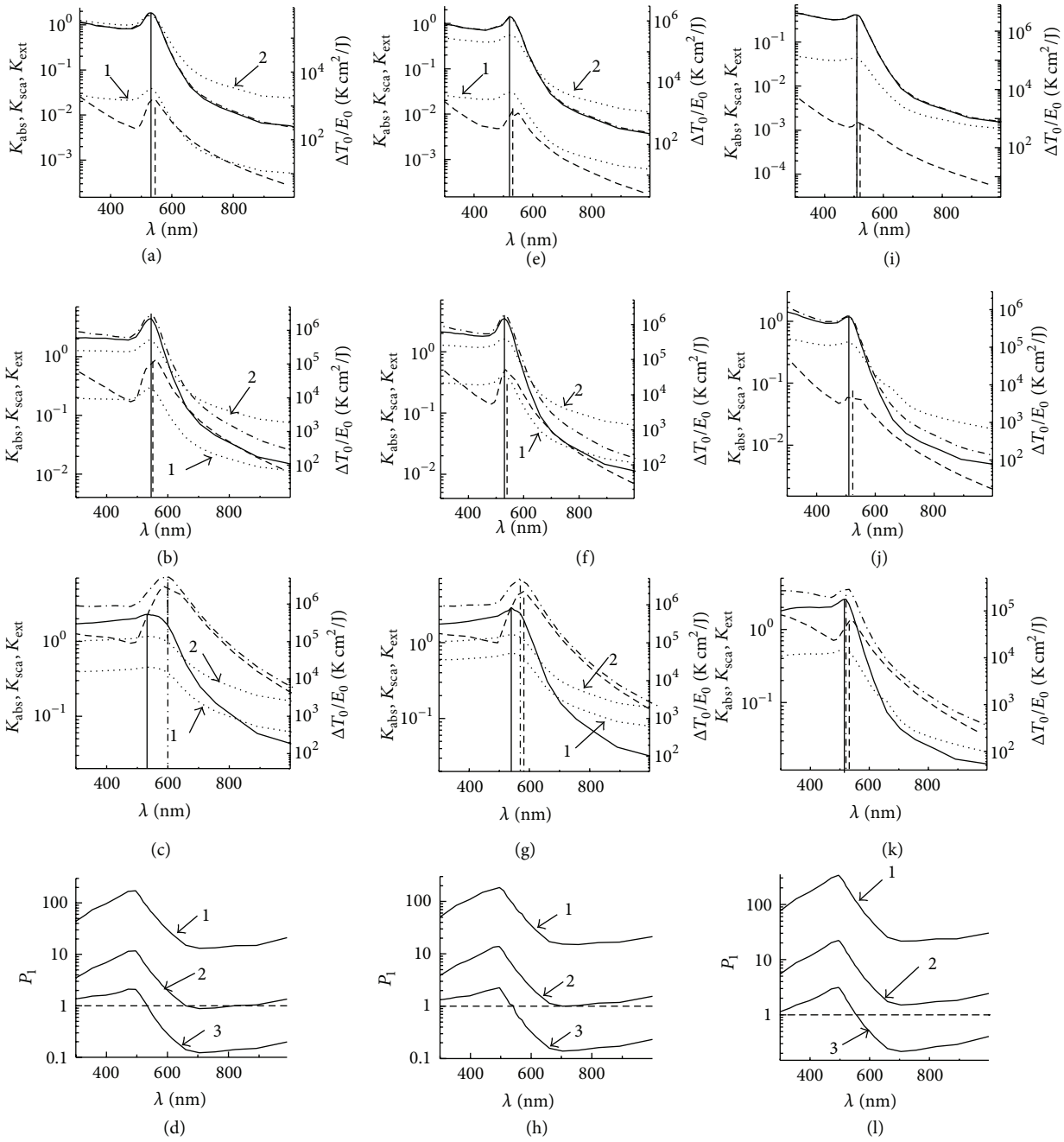

FIGURE 1: Dependences of efficiency factors of absorption K_{abs} (solid), scattering K_{sca} (dashed), and extinction K_{ext} (dashed-dotted) of radiation and parameter $\Delta T_0/E_0$ (dotted) for $t_P = 1 \cdot 10^{-8}$ (1), $1 \cdot 10^{-12}$ (2) s for **Au** NPs with radii $r_0 = 10$ ((a), (e), and (i)), 25 ((b), (f), and (j)), and 50 ((c), (g), and (k)) nm, and the dependences of parameter P_1 ((d), (h), and (l)) for Au NPs with radii $r_0 = 10$ nm (1), $r_0 = 25$ nm (2), and $r_0 = 50$ nm (3) on wavelengths λ. Au NPs are placed in silica ((a)–(d)), water ((e)–(h)), and air ((i)–(l)).

of K_{abs}, K_{sca}, and K_{ext} on axis λ can be connected with possible manifestation of resonances with higher orders (Figures 3(c) and 3(g) Pt NPs). An increase of NP radii to $r_0 = 50$ nm shifts the maximum values of K_{sca} and K_{ext} in the region of greater values of λ. The value of shift of $\Delta\lambda_{max} = \lambda_{max}(K_{abs}) - \lambda_{max}(K_{sca})$ increases with increasing of r_0, for $r_0 = 10$ nm $\Delta\lambda_{max} \sim 5$–13 nm for all surroundings, and for $r_0 = 50$ nm this one achieves values of $\Delta\lambda_{max} \sim 15$–70 nm. These values increase with increasing of n_λ from air to silica for Au, Ag, Pt NPs. But K_{sca}^{max} and K_{ext}^{max} have been shifted compared to the position of $K_{abs}^{max}(\lambda_{abs}^{max})$ up to 80–120 nm (Figures 1(c), 2(c), and 2(g)) to bigger values of λ with increasing of r_0.

Figure 3 shows for **Pt** NPs that maximums of absorption K_{abs}^{max} and scattering K_{sca}^{max} for $r_0 = 10$ nm are accordingly situated at wavelengths $\lambda_{abs}^{max} = 248$ nm and $\lambda_{sca}^{max} = 150$ nm in silica. Increase of r_0 leads to shifting of K_{abs}^{max}, K_{sca}^{max}, and

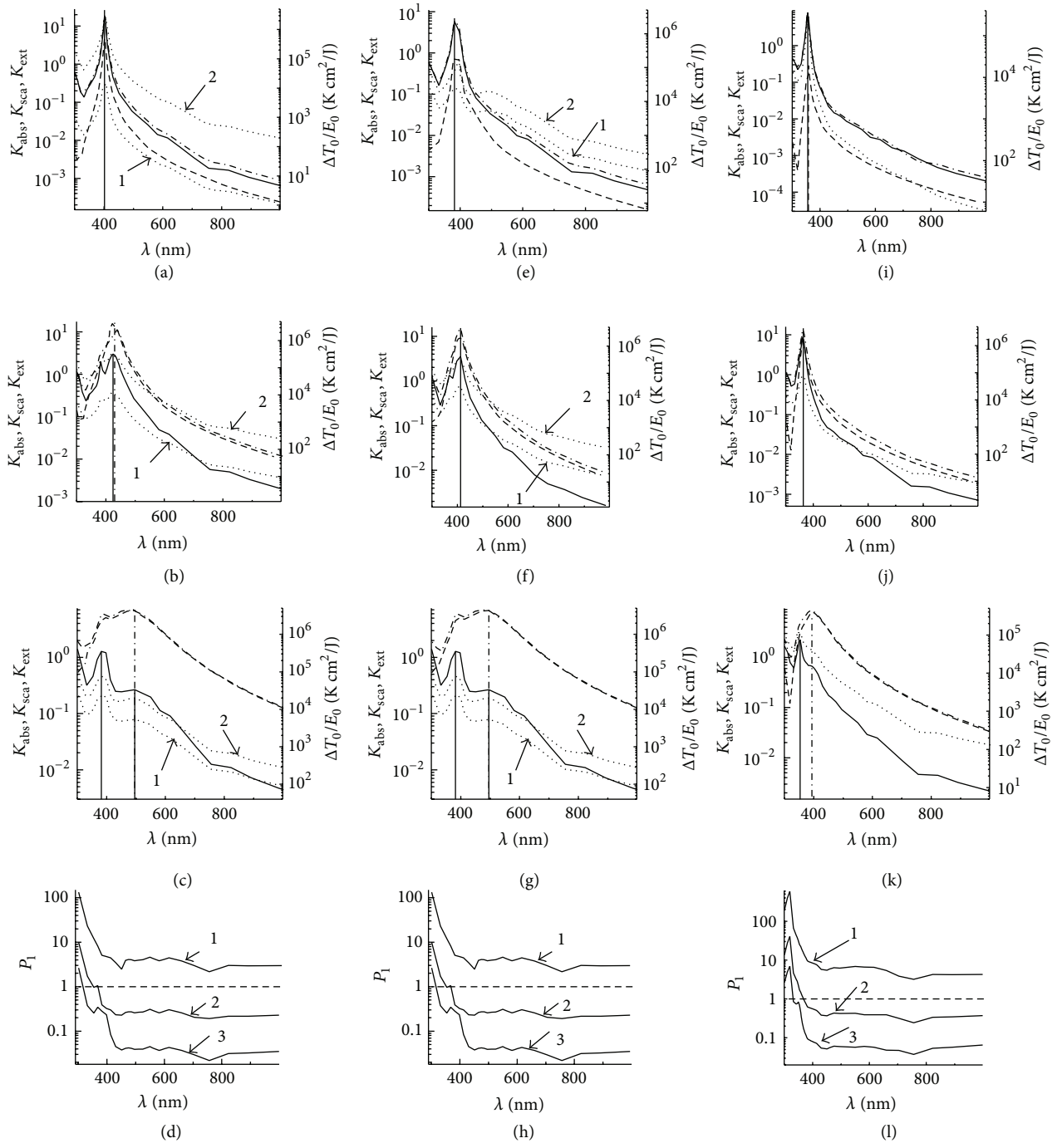

FIGURE 2: Dependences of K_{abs} (solid), K_{sca} (dashed), and K_{ext} (dashed-dotted) of radiation and parameter $\Delta T_0/E_0$ (dotted) for $t_P = 1 \cdot 10^{-8}$ (1), $1 \cdot 10^{-12}$ (2) s for **Ag** NPs with radii $r_0 = 10$ ((a), (e), and (i)), 25 ((b), (f), and (j)), and 50 ((c), (g), and (k)) nm, and the dependences of parameter P_1 ((d), (h), and (l)) for Ag NPs with radii $r_0 = 10$ nm (1), $r_0 = 25$ nm (2), and $r_0 = 50$ nm (3) on wavelengths λ. Ag NPs are placed in silica ((a)–(d)), water ((e)–(h)), and air ((i)–(l)).

K_{ext}^{max} to bigger values of λ; for example, K_{abs}^{max} is shifted from $\lambda_{abs}^{max} \sim 220$–$250$ nm for $r_0 = 10$ nm to $\lambda_{abs}^{max} \sim 450$–$480$ nm for $r_0 = 50$ nm in silica and water. But for air this shift is from $\lambda_{abs}^{max} \sim 220$ nm for $r_0 = 10$ nm to $\lambda_{abs}^{max} \sim 310$ nm for $r_0 = 50$ nm. Maximum values of K_{abs}^{max}, K_{sca}^{max}, and K_{ext}^{max} are at the values of λ_{abs}^{max}, λ_{sca}^{max}, and λ_{ext}^{max} for $r_0 = 50$ nm. Moreover two maximum values of K_{abs}^{max} are formed for $r_0 = 50$ nm in silica at $\lambda_{abs}^{max} = 317.9$ and 495.9 nm and in water at $\lambda_{abs}^{max} = 290$ and 477 nm.

For Au NPs, dependences of P_1 on λ are determined by the dependences of K_{abs} and K_{sca} on λ. Increase of r_0 from $r_0 = 10$ nm to $r_0 = 50$ nm leads to a decrease of the parameter P_1 from the values of about $P_1 \sim 20$–300 for $\lambda \sim 300$–1000 nm up to values of about $P_1 \sim 0.1$–0.3 for $\lambda \sim 600$–1000 nm.

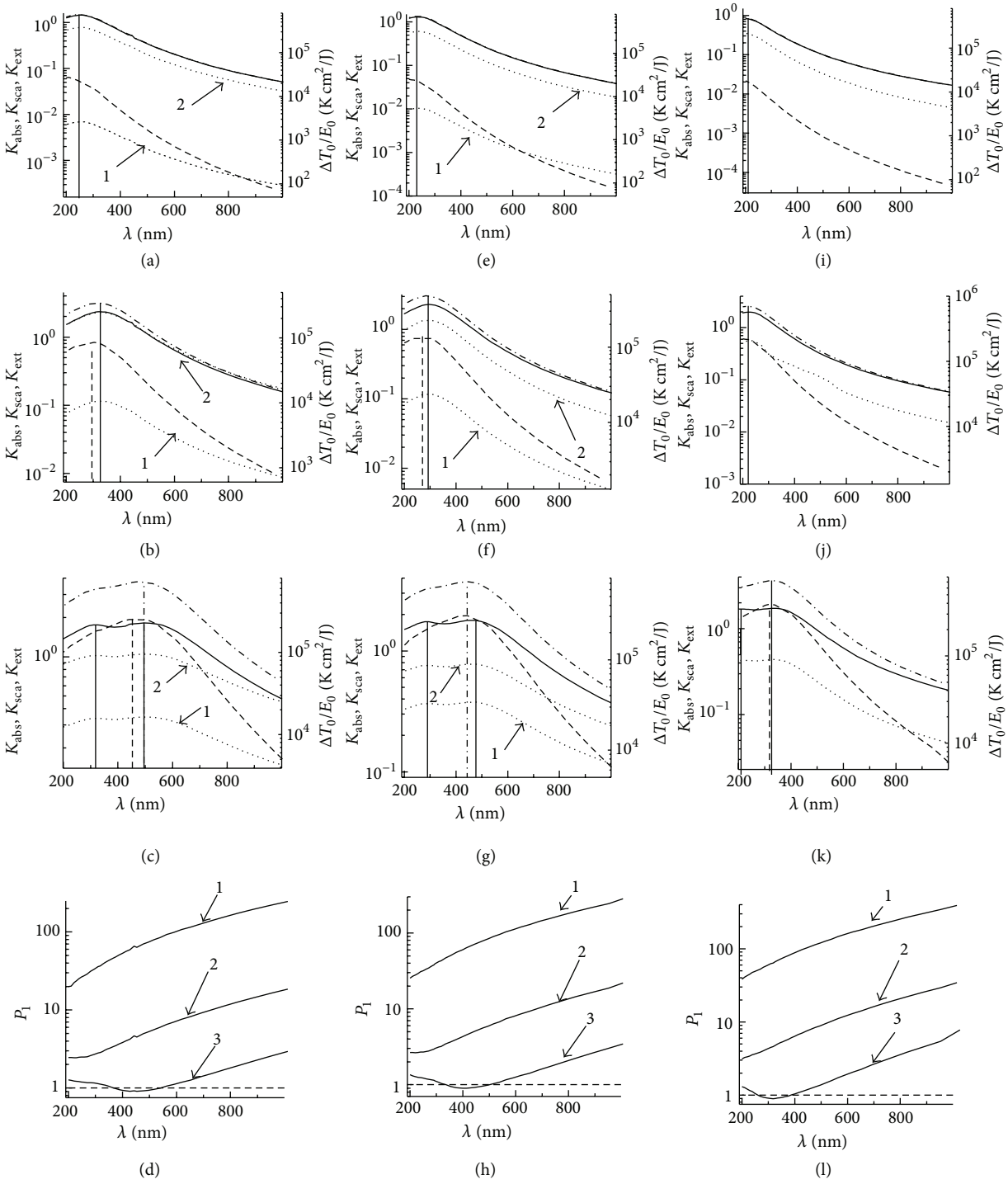

FIGURE 3: Dependences of K_{abs} (solid), K_{sca} (dashed), and K_{ext} (dashed-dotted) of radiation and parameter $\Delta T_0/E_0$ (dotted) for $t_P = 1 \cdot 10^{-8}$ (1), $1 \cdot 10^{-12}$ (2) s for **Pt** NPs with radii $r_0 = 10$ ((a), (e), and (i)), 25 ((b), (f), and (j)), and 50 ((c), (g), and (k)) nm, and the dependences of parameter P_1 ((d), (h), and (l)) for **Pt** NPs with radii $r_0 = 10$ nm (1), $r_0 = 25$ nm (2), and $r_0 = 50$ nm (3) on wavelengths λ. Pt NPs are placed in silica ((a)–(d)), water ((e)–(h)), and air ((i)–(l)).

It means sharp increase of radiation scattering by NPs with an increase of NP r_0. For Ag NPs, a sharp decrease with increasing of λ in the spectral interval $\lambda \sim 300$–400 nm is observed and is approximately constant in the interval $\lambda \sim 300$–1000 nm. General feature for all presented dependences of $P_1(\lambda, r_0)$ is the decrease of P_1 with increasing of r_0 for the whole spectral interval $\lambda \sim 200$–1000 nm.

The dependences of P_1 on λ for Pt NPs increase with increasing λ for $r_0 = 10$ and 25 nm and achieve values of $P_1 \sim 3$–200 for the whole spectral interval because of

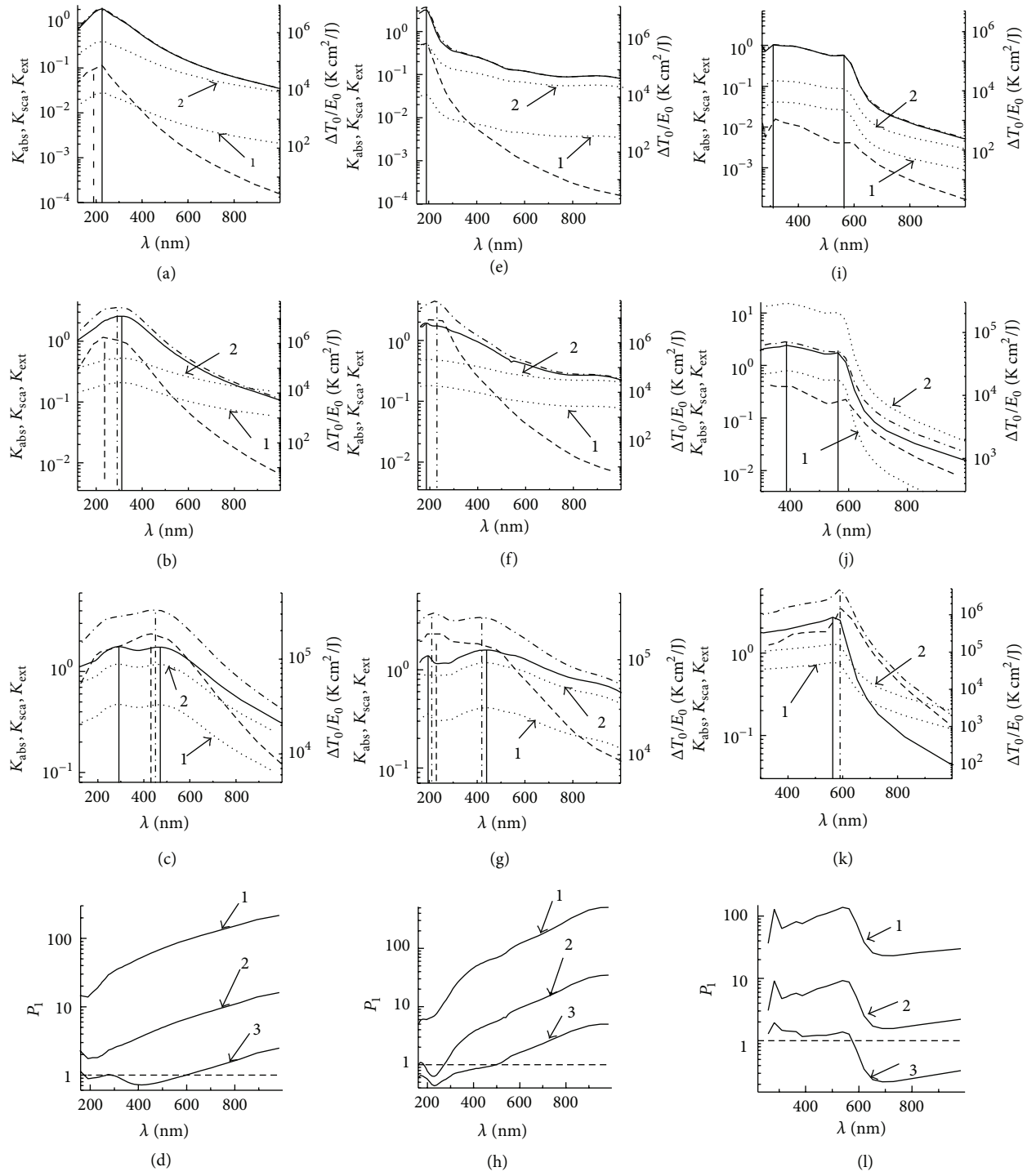

FIGURE 4: Dependences of factors K_{abs} (solid), K_{sca} (dashed), and K_{ext} (dashed-dotted) of radiation for homogeneous metallic **Pd** ((a), (b), (c), and (d)), **Cu** ((e), (f), (g), and (h)), and **Mo** ((i), (j), (k), and (l)) NPs, placed in water, with radii $r_0 = 10$ ((a), (d), and (g)), 25 ((b), (e), and (h)), and 50 ((c), (f), and (i)) nm, parameter $\Delta T_0/E_0$ (dotted) for $t_P = 1 \cdot 10^{-8}$ (1), $1 \cdot 10^{-12}$ (2) s, and dependences of parameter P_1 ((d), (h), and (l)) for 10 (1), 25 (2), and 50 (3) nm on wavelengths λ.

sharp decreasing of K_{sca} with increase of λ (see Figure 3). The parameter P_1 is smaller than 1, $P_1 < 1$, for $r_0 = 50$ nm and the narrow wavelength interval ~350–500 nm for different surroundings.

Figures 1–3 describe the influence of the medium refraction indexes and thermal properties on plasmonic and thermooptical properties of Au, Ag, and Pt NPs. Concrete values of K_{abs}^{max} and k_∞ determine the influence of different

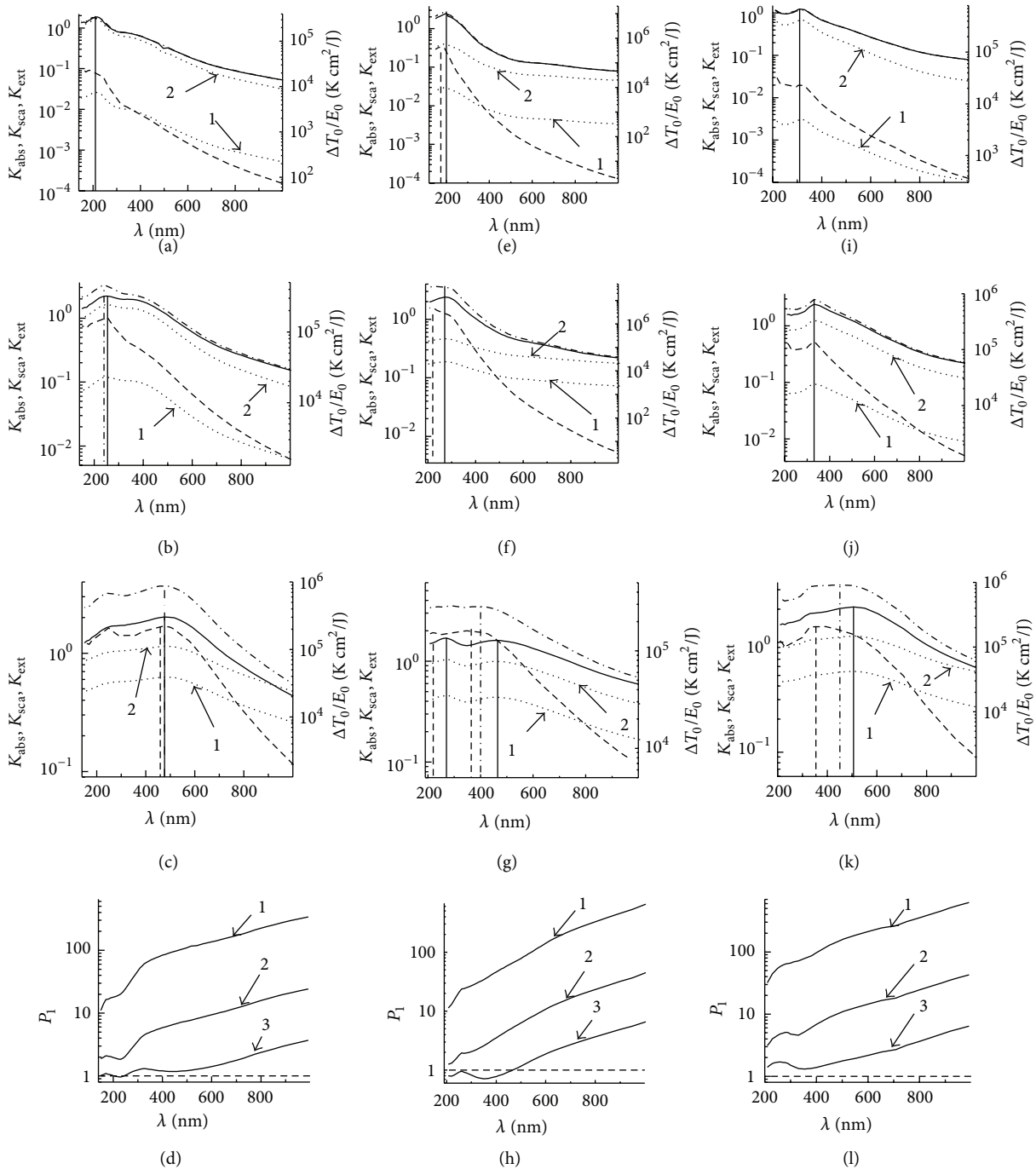

FIGURE 5: Dependences of factors K_{abs} (solid), K_{sca} (dashed), and K_{ext} (dashed-dotted) of radiation for homogeneous metallic **Ni** ((a), (b), (c), and (d)), **V** ((e), (f), (g), and (h)), and **Ti** ((i), (j), (k), and (l)) NPs, placed in water, with radii r_0 = 10 ((a), (d), and (g)), 25 ((b), (e), and (h)), and 50 ((c), (f), and (i)) nm, parameter $\Delta T_0/E_0$ (dotted) for $t_P = 1 \cdot 10^{-8}$ (1), $1 \cdot 10^{-12}$ (2) s, and dependences of parameter P_1 ((d), (h), and (l)) for 10 (1), 25 (2), and 50 (3) nm on wavelengths λ.

surroundings on the value of $\Delta T_0/E_0$ for different t_P (see (3)). The wavelength shift $\Delta\lambda_{max}$ exists between maximums of K_{abs}^{max} from one side and maximums of K_{sca}^{max} and K_{ext}^{max} from a second side for silica and water. Maximum values and dependences of K_{abs}, K_{sca}, and K_{ext} on wavelength are qualitatively close to each other for r_0 = 10, 25, and 50 nm.

The decrease of refraction index from n_λ = 1.51 for silica to n_λ = 1.00 for air leads to shifting of λ_{max} for all efficiency factors for K_{abs} from ~545 nm to ~510 nm and for K_{sca} and K_{ext} from 600 nm to 510 nm. Decrease of n_λ for silica to n_λ = 1.00 (air) leads to decrease of values of K_{abs}, K_{sca}, and K_{ext} up to 4 times for r_0 = 10 and 25 nm, but for r_0 = 50 nm

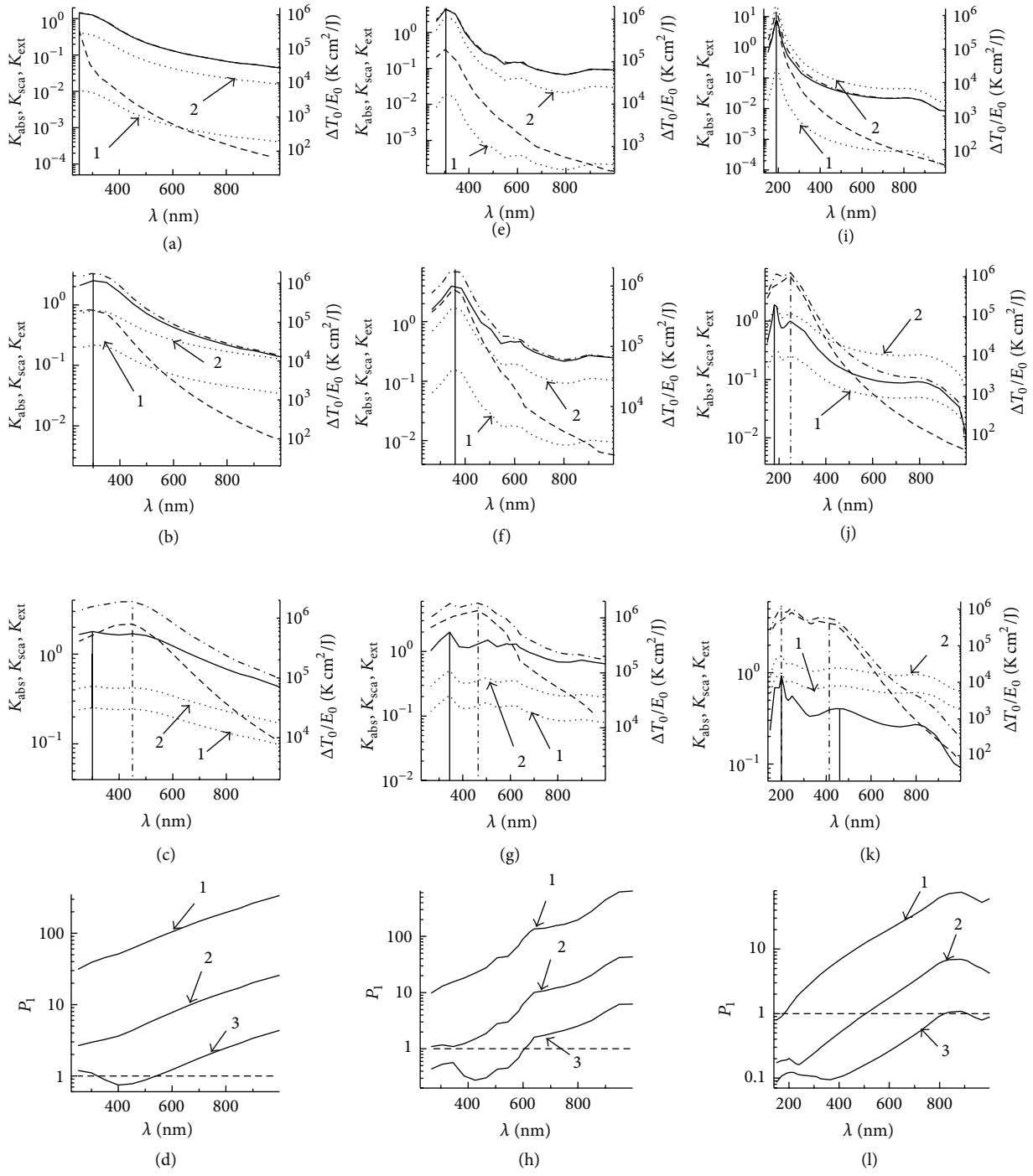

FIGURE 6: Dependences of factors K_{abs} (solid), K_{sca} (dashed), and K_{ext} (dashed-dotted) of radiation for homogeneous metallic **Co** ((a), (b), (c), and (d)), **Zn** ((e), (f), (g), and (h)), and **Al** ((i), (j), (k), and (l)) NPs, placed in water, with radii $r_0 = 10$ ((a), (d), and (g)), 25 ((b), (e), and (h)), and 50 ((c), (f), and (i)) nm, parameter $\Delta T_0/E_0$ (dotted) for $t_P = 1 \cdot 10^{-8}$ (1), $1 \cdot 10^{-12}$ (2) s, and dependences of parameter P_1 ((d), (h), and (l)) for 10 (1), 25 (2), and 50 (3) nm on wavelengths λ.

the dependence of maximum values of K_{abs}, K_{sca}, and K_{ext} is rather weak and leads to the smoothing of plasmonic peaks of the dependences of $K(\lambda)$, first of all, for $r_0 = 10, 25$ nm.

The spectral dependence of $\Delta T_0/E_0(\lambda)$ is determined by the dependence of $K_{abs}(\lambda)$ for all values of r_0, because of dependence $\Delta T_0/E_0 \sim K_{abs}(\lambda)$ in (3), (4a), and (4b). The influence of NP radius r_0 is directly realized on the value of $\Delta T_0/E_0$ and it is determined by the dependence of $K_{abs}(r_0)$ and value of r_0 in (3), (4a), and (4b). Parameters of surroundings influence the value of $\Delta T_0/E_0$ by the value of $K_{abs}(n_\lambda)$.

The values of $\Delta T_0/E_0$ for $t_P = 1 \times 10^{-8}$ s are, as a rule, smaller in comparison with other ones for $t_P = 1 \times 10^{-12}$ s. It is determined by the influence of heat exchange of NP with

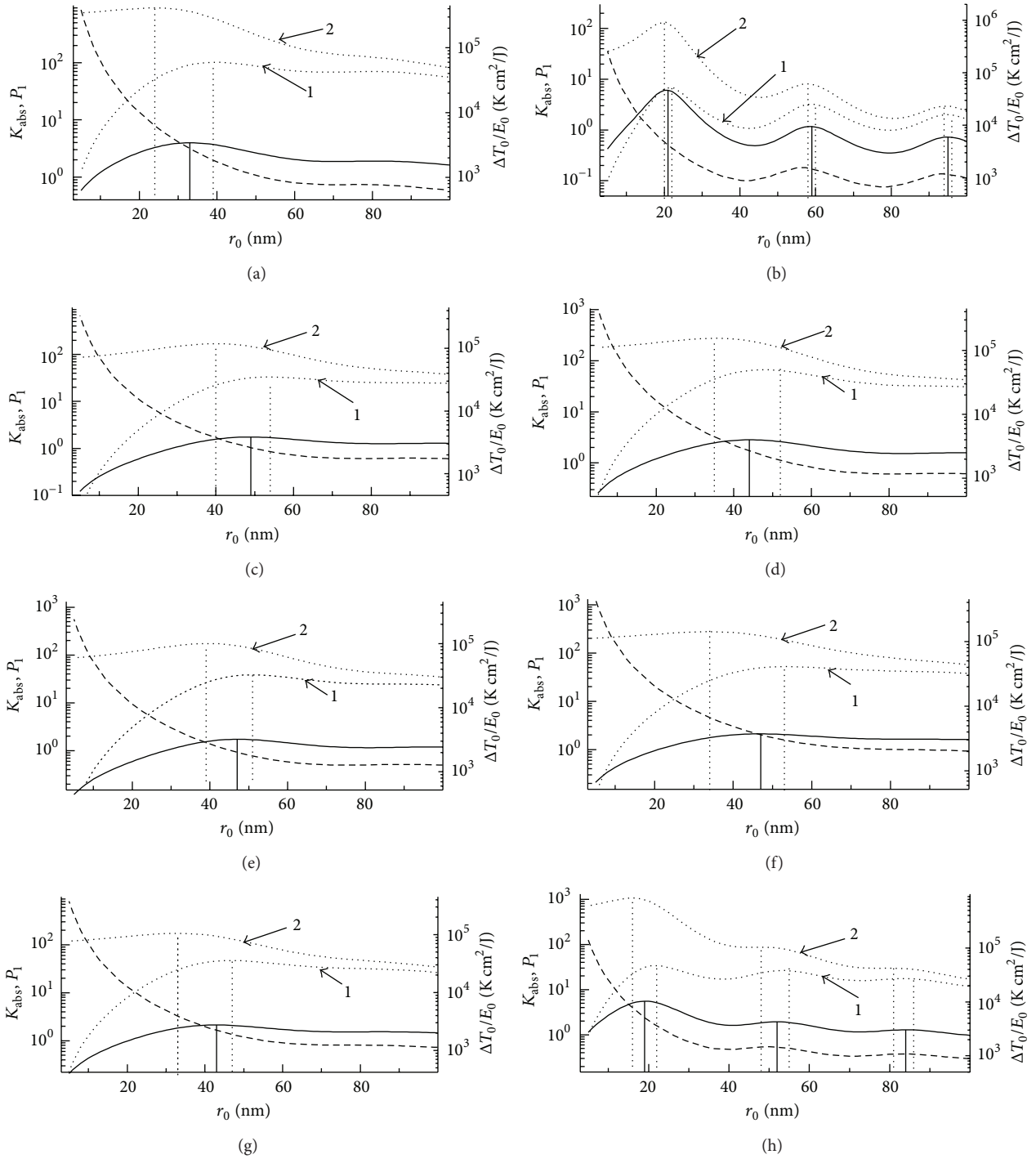

FIGURE 7: Dependences of K_{abs} (solid lines refer to the left axis), parameter P_1 (dashed lines refer to the left axis), and thermooptical parameter $\Delta T_0/E_0$ (dotted lines refer to the right axis) for $t_P = 1 \cdot 10^{-8}$ (1), $1 \cdot 10^{-12}$ (2) s for NPs - Au, $\lambda = 532$ nm (a), Ag, $\lambda = 400$ nm (b), Pt, $\lambda = 500$ nm (c), Cu, $\lambda = 570$ nm (d), Pd, $\lambda = 470$ nm (e), Ti, $\lambda = 500$ nm (f), Ni, $\lambda = 470$ nm (g), and Zn, $\lambda = 350$ nm (h) on r_0.

surrounding medium during radiation pulse action for pulse duration $t_P = 1 \times 10^{-8}$ s and bigger ones.

The maximum value of $(\Delta T_0/E_0)_{max}$ for Au NPs, placed in silica, is equal to $(\Delta T_0/E_0)_{max} = 5.53 \times 10^5$ Kcm^2/J for $r_0 = 10$ nm, $\lambda = 532$ nm, and $t_P = 1 \times 10^{-12}$ s. Maximum values for Ag NPs, placed in different media, of about $(\Delta T_0/E_0)_{max} \sim (2 - 5) \times 10^6$ Kcm^2/J are achieved with $r_0 = 10$ nm and $t_P = 1 \times 10^{-12}$ s among other NPs. For example, Ag NPs with $r_0 = 10$ nm, placed in water, can achieve the heating of $\Delta T_0 = 100$ K under action of laser pulse with $\lambda = 382$ nm,

$t_P = 1 \times 10^{-10}$, 1×10^{-12} s, and $E_0 = 5.6 \times 10^{-5}$ J/cm^2. It is connected with the achievement of maximum values of K_{abs} for Ag NPs in comparison with other presented NPs.

Figures 4–6 present efficiency factors of absorption K_{abs}, scattering K_{sca}, and extinction K_{ext} for radiation with wavelengths λ in the spectral interval 200–1000 nm for homogeneous metallic spherical NPs with radii 10, 25, and 50 nm, placed in water, for nine different metals.

Figure 4 presents factors of K_{abs}, K_{sca}, and K_{ext} of radiation with wavelengths in the range 300–1000 nm by metallic Pd, Mo, and Cu NPs with radii $r_0 = 10$, 25, and 50 nm placed in water.

The spectral dependences of K_{abs} and K_{ext} for Cu NPs are smooth enough for $r_0 = 10$ and 25 nm. An interesting feature of these dependences of K_{abs} and K_{ext} on λ for $r_0 = 10$ and 25 nm is the formation of so called "step" (weak dependence of K_{abs} and K_{ext} on λ) for the spectral interval of $\lambda \approx$ 300–565 nm. There is one weakly defined maximum in these curves for 310 nm ($r_0 = 10$ nm) and for 387 nm ($r_0 = 25$ nm). We see sharp folding of the dependences of K_{abs} and K_{ext} on λ for $r_0 = 10$ and 25 nm at $\lambda \approx 565$ nm. For $r_0 = 10$ and 25 nm values of $K_{abs} \gg K_{sca}$ and dependences of K_{ext} and K_{abs} on λ are close to each other. The factor of scattering K_{sca} monotonously decreases with increasing λ for $r_0 = 10$ and 25 nm.

In the case of $r_0 = 50$ nm spectral dependences of K_{abs}, K_{sca}, and K_{ext} for Cu NPs have one distinct pronounced maximum: $K_{abs}^{max} \approx 2.7$ for $\lambda_{abs}^{max} = 563$ nm and $K_{sca}^{max} \approx 3.5$, $\lambda_{sca}^{max} = 590$ nm and $K_{ext}^{max} \approx 6$ for $\lambda_{ext}^{max} = 590$ nm. Positions of K_{abs}^{max}, K_{sca}^{max}, and K_{ext}^{max} have been separated in Figure 4 for $r_0 = 50$ nm.

Factor $K_{abs} > K_{sca}$ and $P_1 > 1$ for $r_0 = 10$ and 25 nm and for all presented intervals of wavelengths. But for spectral interval $\lambda \approx$ 570–1000 nm, the value of P_1 is smaller than 1, $P_1 < 1$.

Maximum of K_{abs}^{max} for Pd NP is shifted from the position $\lambda_{abs}^{max} = 230$ nm at $r_0 = 10$ nm to bigger values of λ with increasing r_0 up to $\lambda_{abs}^{max} = 310$ nm and with formation of two weakly defined maxima of K_{abs}^{max} at $\lambda_{abs}^{max} = 292$ nm and $\lambda_{abs}^{max} = 470$ nm for $r_0 = 50$ nm. The maximum of K_{sca}^{max} is shifted from the values of $\lambda_{sca}^{max} = 190$ nm for $r_0 = 10$ nm to $\lambda_{sca}^{max} = 230$ nm for $r_0 = 25$ nm, and $\lambda_{sca}^{max} = 435$ nm at $r_0 = 50$ nm. The maximum of K_{ext}^{max} is shifted from the values of $\lambda_{ext}^{max} = 190$ nm for $r_0 = 10$ nm to $\lambda_{ext}^{max} = 450$ nm at $r_0 = 50$ nm. We see that the values of K_{abs}^{max}, K_{sca}^{max}, and K_{ext}^{max} have been placed at different positions on λ axis. Parameter P_1 increases up to values of $P_1 \sim$ 10–100 for $r_0 = 10$, 25, and 50 nm with increasing of λ in the range of $\lambda \sim$ 200–1000 nm. For the spectral interval of $\lambda \sim$ 200–600 nm parameter P_1 is smaller than 1, $P_1 < 1$.

Two maximum values of $(\Delta T_0/E_0)_{max}$ are realized in Figures 4(c) and 4(g), for Cu and Pd NPs because two maxima of K_{abs}^{max} have been formed for $r_0 = 50$ nm.

For Mo NPs (Figures 4(e), 4(f), 4(g), and 4(h)) maxima of K_{abs}^{max} are realized in the spectral region 180 ÷ 200 nm for $r_0 = 10$ and 25 nm. Positions of maxima of K_{sca}^{max} and K_{ext}^{max} are shifted from ~200 for $r_0 = 10$ nm to ~230 nm when increasing NP radius up to 25 nm. When the radius is increased up to 50 nm, two maxima of K_{abs}^{max}, K_{sca}^{max}, and K_{ext}^{max} are formed in all curves in Figure 4 (g). They are localized in the case of K_{abs}^{max} at $\lambda_{abs}^{max} = 200$ nm and 440 nm, K_{sca}^{max} at $\lambda_{sca}^{max} = 230$ and 420 nm, and K_{ext}^{max} at $\lambda_{ext}^{max} = 210$ and 420 nm. Maximum value of absorption of Mo NPs attains $K_{abs}^{max} \approx 3.2$ for $r_0 = 10$ nm and maximum values scattering and extinction attain $K_{sca}^{max} \approx 2.73$ and $K_{ext}^{max} \approx 4.5$ accordingly for $r_0 = 50$ nm. Two maximum values of $(\Delta T_0/E_0)_{max}$ are realized in Figure 5(g) for Mo NPs.

Figure 5 presents spectral dependences of efficiency factors of K_{abs}, K_{sca}, and K_{ext} of radiation in the range 150–1000 nm by metallic Ni, V, and Ti NPs with radii $r_0 = 10$, 25, and 50 nm, placed in water. Spectral dependences of efficiency factors of K_{abs}, K_{sca}, and K_{ext} for Ni, V, and Ti NPs for radii $r_0 = 10$ nm and 25 nm are smooth curves with maxima in the UV region. With increasing wavelength till 1000 nm absorption, scattering, and extinction slowly decrease. In the case of $r_0 = 50$ nm spectral dependences of efficiency factors of K_{abs} and K_{sca} for V NPs have some weakly defined maxima located both in UV and in visible region of spectra.

For Ni, V, and Ti NPs we see general features that were early noted for Figures 1–5. The first feature is the shifting of the values of K_{abs}^{max}, K_{sca}^{max}, and K_{ext}^{max} to bigger values of λ with increasing the NP radius; the second one is the shifting between K_{abs}^{max}, K_{sca}^{max}, and K_{ext}^{max} themselves that means that values of λ_{abs}^{max}, λ_{sca}^{max}, and λ_{ext}^{max} have different values, for example, for Ti NPs with $r_0 = 50$ nm, $\lambda_{abs}^{max} = 505$ nm, $\lambda_{sca}^{max} = 355$ nm, and $\lambda_{ext}^{max} = 450$ nm. The third feature is the formation of second maximums of K_{abs}^{max}; for example, second maximum is formed at $\lambda \approx 480$ nm.

Parameters P_1 for Ni, V, and Ti NPs and for the radiation spectral interval $\lambda \approx$ 150–1000 nm are bigger than 1, $P_1 > 1$, instead of narrow interval $\lambda \approx$ 200–480 nm for V NPs with $r_0 = 50$ nm. Moreover, for $r_0 = 10$ and 25 nm parameters P_1 achieve the values of $P_1 \approx$ 10–500 with increasing λ. It means that Ni, Ti, and V NPs are good absorbers of radiation in wide range of ultraviolet, visible, and infrared optical spectrum.

Figure 6 presents the spectral dependences of K_{abs}, K_{sca}, and K_{ext} for metallic **Co**, **Zn,** and **Al** NPs with radii $r_0 = 10$, 25, and 50 nm, when placed in water. Spectral dependences of efficiency factors of K_{abs}, K_{sca}, and K_{ext} for Co nanoparticles are smooth and have some weakly defined maxima located both in UV and in visible region of spectra for $r_0 = 10$ and 25 nm. In the case of $r_0 = 50$ nm maximum of absorption is in the UV region of spectra and maxima of scattering and extinction are in the visible one. The maximum value of absorption for Co NPs is $K_{abs}^{max} \approx 2.5$ for $r_0 = 25$ nm, $\lambda_{abs}^{max} \approx 300$ nm, and maximum values of scattering and extinction are $K_{sca}^{max} \approx 2.2$ and $K_{ext}^{max} \approx 3.9$ for $r_0 = 50$ nm, $\lambda_{sca}^{max} = \lambda_{ext}^{max} = 450$ nm.

For Zn NPs, maxima of spectral dependences of efficiency factors of K_{abs}, K_{sca}, and K_{ext} are sharply defined, more than for Co NPs, and are shifted in the direction of greater wavelengths. For example, the maximum value of absorption for Zn NPs is $K_{abs}^{max} \approx 4.5$ for $r_0 = 10$ nm, $\lambda_{abs}^{max} \approx 305$ nm, and maximum values of scattering and extinction are $K_{sca}^{max} \approx 4.3$ and $K_{ext}^{max} \approx 5.7$ for $r_0 = 50$ nm, $\lambda_{sca}^{max} \approx 465$ nm. We note the shifting of K_{sca}^{max} and K_{ext}^{max} to bigger values of λ in comparison with position K_{abs}^{max} for Co and Zn NPs.

The spectral dependences of efficiency factors of K_{abs}, K_{sca}, and K_{ext} for Al NPs show strongly defined maxima located mainly in UV. Maximum values of absorption and scattering are close for $r_0 = 10$ nm, and then for $r_0 = 25$ and 50 nm maximum values of scattering are essentially higher than absorption. For example, maximum value of absorption for Al NPs is $K_{abs}^{max} \approx 7.5$ for $r_0 = 10$ nm, $\lambda_{abs}^{max} \approx 190$ nm, and maximum values of scattering and extinction are $K_{sca}^{max} \approx 6$, $K_{ext}^{max} \approx 7$ for $r_0 = 25$ nm, and $\lambda_{sca}^{max} \approx 250$ nm. Factors of K_{sca} and K_{ext} rise to maximum values in the spectral interval 190–500 nm, before decreasing with increasing wavelength in the range 200–1000 nm. Some oscillation structures of the dependences of K_{abs} on λ are formed for Al and Zn NPs with increasing of r_0. It is interesting to note for Al NPs the shifting of K_{sca}^{max} and K_{ext}^{max} to bigger values of λ and the formation of two maximums of K_{sca}^{max} and K_{ext}^{max} with simultaneous formation of oscillation structure of the K_{abs} dependence on λ with increasing of r_0 to $r_0 = 50$ nm.

Zn NPs with $r_0 = 25$ nm are good absorbers and bad scatterers for all spectral interval of $\lambda \approx 200$–1000 nm. The parameter P_1 for Al NPs is smaller than one ($P_1 < 1$) for $r_0 = 25$ nm in the range of $\lambda \approx 200$–500 nm and for $r_0 = 50$ nm, $\lambda \approx 150$–1000 nm.

Figures 1–6 present spectral dependences of the parameter $\Delta T_0/E_0$ (3) for pulse duration $t_P = 1 \cdot 10^{-8}$, $1 \cdot 10^{-12}$ s for NPs with radii $r_0 = 10$, 25, and 50 nm placed in water. The range of pulse duration $t_P = 1 \cdot 10^{-8}$–$1 \cdot 10^{-12}$ s is of great interest for laser applications in nanotechnology. The dependences of parameter $\Delta T_0/E_0$ (3) on λ are analogous to the dependences $K_{abs}(\lambda)$ because of (2a) and (2b). For $\lambda_{abs}^{max} \approx 190$ nm and $r_0 = 10$ nm maximum value of thermooptical parameter for Al NPs achieves value $(\Delta T_0/E_0)_{max} \approx 1.5 \times 10^6$ Kcm^2/J.

Figure 7 presents the dependences of K_{abs}, parameter P_1, and thermooptical parameter $\Delta T_0/E_0$ for $t_P = 1 \cdot 10^{-8}$, $1 \cdot 10^{-12}$ s for metallic NPs, placed in water, and fixed values of λ, for Au NPs, $\lambda = 532$ nm; Ag NPs, $\lambda = 400$ nm; Pt NPs, $\lambda = 500$ nm; Cu NPs, $\lambda = 570$ nm; Ti NPs, $\lambda = 500$ nm; Pd NPs, $\lambda = 470$ nm; Ni NPs, $\lambda = 470$ nm; and Zn NPs, $\lambda = 350$ nm on r_0 in the range of radii $r_0 = 5$–100 nm. The locations of maximum values of $K_{abs}^{max}(r_0)$ and $(\Delta T_0/E_0)_{max}$ (t_P, r_0) are denoted by vertical lines (solid and dotted accordingly). The choice of mentioned wavelengths is determined by their location nearby plasmon wavelengths for these NPs (see Figures 1–6). We consider the results for Au and Ag NPs more closely.

Results for Au NPs are presented in Figure 7(a). The maximum value of $K_{abs}^{max}(r_0, \lambda)$ was calculated and was equal to the next value of r_0: $K_{abs}^{max}(\lambda = 532\,\text{nm}) \approx 3.97$ for $r_0 = 33$ nm. The maximum values of $(\Delta T_0/E_0)_{max}$ for $\lambda = 532$ nm are approximately equal to $(\Delta T_0/E_0)_{max} \approx 4.1 \times 10^5$ Kcm^2/J at $r_0 \approx 23$ nm for $t_P = 1 \cdot 10^{-12}$ s and $(\Delta T_0/E_0)_{max} \approx 6 \times 10^4$ Kcm^2/J at $r_0 \approx 39$ nm for $t_P = 1 \cdot 10^{-8}$ s (see Figure 7(a)). The maximum values of $K_{abs}^{max}(r_0)$ and $(\Delta T_0/E_0)_{max}$ (r_0) have different locations on r_0 axis for $\lambda = 532$ nm in Figure 7(a). The maximum values of $(\Delta T_0/E_0)_{max}$ have been shifted by the value $\Delta r_0 \approx 10$ nm to smaller values of r_0 for $t_P = 1 \cdot 10^{-12}$ s and to bigger values of r_0 by the value $\Delta r_0 \approx 6$ nm for $t_P = 1 \cdot 10^{-8}$ s in comparison with the location of K_{abs}^{max} (r_0) in Figure 7(a).

The maximum values of $(\Delta T_0/E_0)_{max}$ for $\lambda = 532$ nm are achieved for $K_{abs} \approx 3.3$, $t_P = 1 \cdot 10^{-12}$ s, and $r_0 \approx 23$ nm and for $K_{abs} \approx 3.6$, $t_P = 1 \cdot 10^{-8}$ s, and $r_0 \approx 39$ nm. It means that for achievement of the maximum values of $(\Delta T_0/E_0)_{max}$ under minimal values of E_0 we have to use the values of K_{abs} that are smaller than K_{abs}^{max} mentioned above.

The differences between the values of $\Delta T_0/E_0$ for $t_P = 1 \cdot 10^{-8}$ s and $t_P = 1 \cdot 10^{-12}$ s decrease with increasing r_0. These differences are about ~10^2-10^3 times for $r_0 = 10$ nm and are equal to only ~2-3 times for $r_0 = 100$ nm. It can be explained by a sharp increase of $\tau_T \sim r_0^2$ and approaching of τ_0 to $t_P = 1 \cdot 10^{-8}$ s for $r_0 \geq 90$–100 nm and fulfillment of short pulse condition (without heat loss).

The characteristic time τ_T is equal to $\tau_T \sim 1.2 \cdot 10^{-10}$–$3.2 \cdot 10^{-9}$ s for the range $r_0 = 10$–50 nm and for ambient water $k_\infty = 6 \cdot 10^{-3}$ W/cmK, $\tau_T \sim 0.9$ ns for $r_0 = 25$ nm. The fulfillment of the condition $t_P < \tau_T$ (1) for the most interesting range of r_0 : $25 < r_0 < 50$ nm means that the value of t_P will be in the range of pulse durations: $t_P < 1 \cdot 10^{-9}$ s.

The condition of "short" pulses $t_P < \tau_T$ is applicable for $t_P = 1 \cdot 10^{-12}$ s for all values of r_0 : $5 < r_0 < 100$ nm. Under condition of "short" pulses $t_P < \tau_T$, the parameter $\Delta T_0/E_0$ depends on the combination K_{abs}/r_0 and, accordingly, equation (3) describing the increasing and decreasing of $\Delta T_0/E_0$.

The condition of "long" pulses with $t_P = 1 \cdot 10^{-8}$ s is also fulfilled for the interval $r_0 = 5$–100 nm. The use of "long" pulses with $t_P = 1 \cdot 10^{-8}$ s leads to a significant decrease of the value of $\Delta T_0/E_0$ up to 1-2 orders and more in comparison with cases for $t_P = 1 \cdot 10^{-12}$ s for the whole range of $r_0 = 5$–100 nm. It is determined by heat conduction losses from NP during irradiation with this value of t_P and because of the dependence $\Delta T_0/E_0 \sim 1/t_P$ (see (3)).

From (4a) and (4b) we see that

$$t_P < \tau_T, \quad \frac{\Delta T_0}{E_0} \sim \frac{K_{abs}(r_0)}{r_0}, \qquad t_P > \tau_T, \quad \frac{\Delta T_0}{E_0} \sim K_{abs}(r_0)\, r_0. \tag{5}$$

Our results are in accordance with presented dependences (5).

Figure 7(b) presents the dependences of parameter $\Delta T_0/E_0$ (r_0, λ) (3) and K_{abs} (r_0, λ) for Ag NPs and for the pulse durations $t_P = 1 \cdot 10^{-8}$, $1 \cdot 10^{-12}$ s, and $\lambda = 400$ nm on r_0. Maximum values of $(\Delta T_0/E_0)_{max}$ for Ag NPs are equal to $\approx 1.1 \times 10^6$ Kcm^2/J, $t_P = 1 \cdot 10^{-12}$ s, and $r_0 \sim 19$ nm and $\approx 5.1 \times 10^4$ Kcm^2/J, and $t_P = 1 \cdot 10^{-8}$ s at $r_0 \sim 21$ nm in the range 5–100 nm (see Figure 7(b)). Heating of NP with $r_0 \sim 19$ nm and for $t_P \leq 1 \cdot 10^{-10}$ s could achieve $1 \cdot 10^3$ K under radiation energy density $E_0 = 1 \times 10^{-3}$ J/cm^2.

There are three maximums of K_{abs}^{max} and correspondingly three maximum values of $(\Delta T_0/E_0)_{max}$ for $t_P = 1 \times 10^{-12}$ s, placed at $r_0 \approx 19$, 58, and 95 nm, in the range of $r_0 = 5$–100 nm. Oscillated dependences of $\Delta T_0/E_0$ behave in an

analogous manner to the dependences of K_{abs} on r_0 for the presented values of λ (see Figure 7(b)). Values of $\Delta T_0/E_0$ for $t_P = 1\times10^{-8}$ s are smaller than the ones for $t_P = 1\times10^{-12}$ s for the whole range of r_0 = 5–100 nm. The values of shift between the locations of K_{abs}^{max} and $(\Delta T_0/E_0)_{max}$ for Ag NPs are smaller than in the case of Au NPs because of sharp dependences of K_{abs} on r_0, especially for λ = 400 nm (see Figure 7(b)).

The dependences of K_{abs}, P_1, and $\Delta T_0/E_0$ on r_0 for fixed values of λ for Pt, Cu, Pd, Ti, and Ni NPs are generally analogous to the dependences of Au NPs. The dependences of Zn NP parameters on r_0 are analogous to the dependences of Ag NPs. For all metallic NPs maximum values of $(\Delta T_0/E_0)_{max}$ are shifted compared to location K_{abs}^{max} in Figure 7(b) to smaller values of r_0 for "short" pulses $t_P < \tau_T$ and to bigger values of r_0 for "long" pulses $t_P > \tau_T$.

Figures 1–6 present the dependences of P_1 on λ for metallic NPs with radii r_0 = 10, 25, and 50 nm and metals Ag, Al, Au, Co, Cu, Mo, Ni, Pd, Pt, Ti, V, and Zn. Dependences of P_1 on λ are determined by the correlation between dependences of $K_{abs}(\lambda)$ and $K_{sca}(\lambda)$. Dependences of P_1 on λ for different values of r_0 have complicated disposition. For NPs with r_0 = 10 nm all presented metallic NPs exhibit high absorbance and parameter $P_1 \gg 1$ for all metallic NPs and in part $P_1 > 1$ for some spectral intervals. The maximum values reached $P_1 \geq 100$ for Co, Mo, Ni, Pd, Pt, Ti, V, and Zn NPs for interval $600 > \lambda > 1000$ nm and for Au and Cu NPs maximum $P_1 \sim 100$ for $300 > \lambda > 500$ nm for r_0 = 10 nm. All mentioned NPs are the best absorbers with $P_1 \geq 10 \div 100$ for $600 > \lambda > 1000$ nm and r_0 = 10 and 25 nm instead of Au and Cu NPs. Increasing of r_0 leads to an increase in scattering and decrease in absorbance for all presented metallic NPs. Therefore, larger NPs are more suitable for light-scattering based applications. At r_0 = 50 nm instead of spectral interval $600 < \lambda < 1000$ nm for Co, Mo, Ni, Pd, Ti, and Zn NPs all values of P_1 are smaller or much smaller than 1, $P_1 \ll 1$. Best scattering NPs among the studied metallic NPs are Ag NPs for $r_0 > 20$ nm. It is interesting to note that NPs can be used as absorbers in one interval of wavelengths and as scatterers in different intervals of wavelengths. All NPs with r_0 = 25 nm could be the scatterers in the interval $300 < \lambda < 500$ nm and the absorbers in the interval $500 < \lambda < 1100$ nm. Variant with value $P_1 \approx 1$ means approximately equal possibility of using NP as absorber and scatterer simultaneously.

A predominant role of absorption by NP can be used for heating of NP for thermoplasmonic applications. Such NPs can be used as absorbers of radiation. A predominant role of scattering by NPs can be used for the purposes of optical diagnostics and imaging using scattered radiation. The selection of ratio between scattering and absorption with $P_1 < 1$ provides a tool for NP for contrast applications in scattering optical diagnostics.

4. Conclusions

The strongly enhanced absorption and scattering of spherical metallic NPs make them a novel and highly effective class of contrast agents for photothermal applications and imaging-based optical diagnostics. A number of factors need to be optimized for the success in these fields. These ones include the efficiency factors of absorption K_{abs}, scattering K_{sca}, and extinction K_{ext} of radiation by NP, parameters of P_1, and $\Delta T_0/E_0$. There is a need to study the dependence of these parameters on the type of metal and size of NP, radiation wavelength, parameters of surrounding medium, and so forth. Systematic study of all these characteristics is a prerequisite for the successful transition of the research promise of metallic NPs to thermal applications and has been carried out in this paper.

We conducted the investigation and analysis of plasmonic (K_{abs}, K_{sca}, and K_{ext}) and thermooptical ($\Delta T_0/E_0$) characteristics of 12 metallic NPs for radiation wavelengths in the spectral interval 200–1000 nm and in the range of NP radii r_0 = 5–100 nm, especially for r_0 = 10, 25, and 50 nm, based on computer and analytical modeling (Figures 1–7). Different metals were used for NPs, Au, Ag, Cu, Pt, Co, Zn, Al, Ni, Ti, V, Pd, and Mo. Three surrounding NP media were used, silica, water, and air. Value of refractive index of surroundings in the range $n_\lambda = 1.51 - 1.0$ influences the plasmonic properties with the change. The use of silica as surroundings leads to rather small deviations from the dependences with water as ambience. More pronounced deviations of NP optical and thermooptical characteristics have been determined for air surrounding.

The selection of different NPs is based on the investigation of the influence of different parameters of NP itself, radiation pulses, and ambient medium on NP properties.

The data in Figures 1–7 allow estimating the possibility to use different metallic NPs for thermoplasmonics and photonic applications. Maximum values of K_{abs} were achieved for Au, Ag, Zn, and Cu. Transformation of plasmonic (K_{abs}, K_{sca}, and K_{ext}) and thermooptical ($\Delta T_0/E_0$) properties in dependence on λ, r_0 with changing of NP, radiation, and ambience parameters is presented in Figures 1–7. Positions λ_{abs}^{max}, λ_{sca}^{max}, and λ_{ext}^{max} of maximum values of K_{abs}^{max}, K_{sca}^{max}, and K_{ext}^{max} have been determined on λ axis and in some cases the positions of K_{abs}^{max}, K_{sca}^{max}, and K_{ext}^{max} do not coincide.

Parameter of P_1 can be used for determination of the use of NP predominantly as an absorber for $P_1 > 1$ or as a scatterer for $P_1 < 1$. It is interesting to note the achievement of values of $P_1 \geq$ 10–100 for mentioned NPs with r_0 = 10 and 25 nm instead of Ag and Al NPs in some spectral intervals. Larger NPs are more suitable for light-scattering based applications. Best scattering NPs inside presented metallic NPs are Ag NPs for $r_0 > 20$ nm. It is interesting to note Al NPs with r_0 = 25 nm which can be used as absorbers in one wavelength interval ($1100 > \lambda > 500$ nm) and as scatterers in the different one ($500 > \lambda > 300$ nm).

The main goal of light-to-thermal energy conversion and thermoplasmonics is to achieve maximum value of efficiency parameter of $\Delta T_0/E_0$ for NPs at minimal values of E_0. The influence of the parameters of radiation, t_P, λ, and E_0 of NP, ρ_0, c_0, r_0, K_{abs}, and surrounding medium, $k_\infty$and n_λ, reach a maximum value of $\Delta T_0/E_0$ has been established based on an analytical model. It is possible to achieve the values of about $\Delta T_0/E_0 \sim 1\cdot10^6$ Kcm^2/J for NPs and for $t_P \leq 1\cdot10^{-10}$ s under radiation energy density $E_0 = 1\cdot10^{-3}$ J/cm^2 and the heating of such NP could achieve $1\cdot10^3$ K.

The selection of appropriate properties of NPs is based on the choice of value of r_0 for the values of determined λ and t_P and the choice of metallic NPs, λ, and t_P for the determined value of r_0.

It was established that maximum values of $\Delta T_0/E_0$ and of NP temperature can be achieved with the use of the value of absorption efficiency factor K_{abs} smaller than maximum value of $K_{\text{abs}}^{\max}$ taking into account irradiation duration, characteristics of NPs, and their cooling. Shift of the positions of maximum value of $\Delta T_0/E_0$ from the location of maximum value of $K_{\text{abs}}^{\max}$ on axis r_0 is determined by noticeable influence of r_0 on the processes of NP heating and cooling.

Our results allow estimating of optimal characteristics of absorption and scattering radiation by NPs and laser energy conversion into photothermal phenomena by selection of the NP and radiation parameters and ambience properties. We present a platform for selection of the plasmonic and thermooptical properties of metallic NPs, placed in different media, for their photonic and thermoplasmonic applications.

Conflict of Interests

The authors declare that there is no conflict of interests regarding the publication of this paper.

References

[1] J. R. Adleman, D. A. Boyd, D. G. Goodwin, and D. Psaltis, "Heterogenous catalysis mediated by plasmon heating," *Nano Letters*, vol. 9, no. 12, pp. 4417–4423, 2009.

[2] R. Narayanan and M. A. El-Sayed, "Some aspects of colloidal nanoparticle stability, catalytic activity, and recycling potential," *Topics in Catalysis*, vol. 47, no. 1-2, pp. 15–21, 2008.

[3] N. J. Halas, "The photonic nanomedicine revolution: let the human side of nanotechnology emerge," *Nanomedicine*, vol. 4, no. 4, pp. 369–371, 2009.

[4] L. C. Kennedy, L. R. Bickford, N. A. Lewinski et al., "A new era for cancer treatment: gold-nanoparticle-mediated thermal therapies," *Small*, vol. 7, no. 2, pp. 169–183, 2011.

[5] X. Huang, P. K. Jain, I. H. El-Sayed, and M. A. El-Sayed, "Plasmonic photothermal therapy (PPTT) using gold nanoparticles," *Lasers in Medical Science*, vol. 23, no. 3, pp. 217–228, 2008.

[6] V. K. Pustovalov, A. S. Smetannikov, and V. P. Zharov, "Photothermal and accompanied phenomena of selective nanophotothermolysis with gold nanoparticles and laser pulses," *Laser Physics Letters*, vol. 5, no. 11, pp. 775–792, 2008.

[7] V. Pustovalov, L. Astafyeva, and B. Jean, "Computer modeling of the optical properties and heating of spherical gold and silica-gold nanoparticles for laser combined imaging and photothermal treatment," *Nanotechnology*, vol. 20, no. 22, Article ID 225105, 2009.

[8] V. Pustovalov, L. Astafyeva, E. Galanzha, and V. Zharov, "Thermo-optical analysis and selection of the properties of absorbing nanoparticles for laser applications in cancer nanotechnology," *Cancer Nanotechnology*, vol. 1, pp. 35–46, 2010.

[9] A. Csaki, F. Garwe, A. Steinbrück et al., "A parallel approach for subwavelength molecular surgery using gene-specific positioned metal nanoparticles as laser light antennas," *Nano Letters*, vol. 7, no. 2, pp. 247–253, 2007.

[10] J. Wang, J. D. Byrne, M. E. Napier, and J. M. Desimone, "More effective nanomedicines through particle design," *Small*, vol. 7, no. 14, pp. 1919–1931, 2011.

[11] S. Jain, D. Hirst, and J. O'Sullivan, "Gold nanoparticles as novel agents for cancer therapy," *British Journal of Radiology*, vol. 85, no. 1010, pp. 101–113, 2012.

[12] N. Zheludev, "Single nanoparticle as photonic switch and optical memory element," *Journal of Optics A: Pure and Applied Optics*, vol. 8, no. 4, pp. S1–S9, 2006.

[13] M. Pelton, J. Aizpurua, and G. Bryant, "Metal-nanoparticle plasmonics," *Laser and Photonics Reviews*, vol. 2, no. 3, pp. 136–159, 2008.

[14] Y. Sonnefraud, A. L. Leen Koh, D. W. McComb, and S. A. Maier, "Nanoplasmonics: engineering and observation of localized plasmon modes," *Laser and Photonics Reviews*, vol. 6, no. 3, pp. 277–295, 2012.

[15] Y. Jin, Q. Li, G. Li et al., "Enhanced optical output power of blue light-emitting diodes with quasi-aligned gold nanoparticles," *Nanoscale Research Letters*, vol. 9, no. 1, pp. 7–13, 2014.

[16] S. Inasawa, M. Sugiyama, S. Noda, and Y. Yamaguchi, "Spectroscopic study of laser-induced phase transition of gold nanoparticles on nanosecond time scales and longer," *Journal of Physical Chemistry B*, vol. 110, no. 7, pp. 3114–3119, 2006.

[17] H. Muto, K. Miyajima, and F. Mafuné, "Mechanism of laser-induced size reduction of gold nanoparticles as studied by single and double laser pulse excitation," *The Journal of Physical Chemistry C*, vol. 112, no. 15, pp. 5810–5815, 2008.

[18] A. Pyatenko, M. Yamaguchi, and M. Suzuki, "Mechanisms of size reduction of colloidal silver and gold nanoparticles irradiated by Nd:YAG laser," *Journal of Physical Chemistry C*, vol. 113, no. 21, pp. 9078–9085, 2009.

[19] S. Hashimoto, D. Werner, and T. Uwada, "Studies on the interaction of pulsed lasers with plasmonic gold nanoparticles toward light manipulation, heat management, and nanofabrication," *Journal of Photochemistry and Photobiology C: Photochemistry Reviews*, vol. 13, no. 1, pp. 28–54, 2012.

[20] J. Wang, Y. Chen, X. Chen, J. Hao, M. Yan, and M. Qiu, "Photothermal reshaping of gold nanoparticles in a plasmonic absorber," *Optics Express*, vol. 19, no. 15, pp. 14726–14734, 2011.

[21] M. Honda, Y. Saito, N. I. Smith, K. Fujita, and S. Kawata, "Nanoscale heating of laser irradiated single gold nanoparticles in liquid," *Optics Express*, vol. 19, no. 13, pp. 12375–12383, 2011.

[22] A. L. Stepanov, "Nonlinear optical properties of implanted metal nanoparticles in various transparent matrixes: a review," *Reviews on Advanced Materials Science*, vol. 27, no. 2, pp. 115–145, 2011.

[23] A. Stalmashonak, G. Seifert, and A. Abdolvand, *Ultra-Short Pulsed Laser Engineered Metal-Glass Nanocomposites*, Springer, New York, NY, USA, 2013.

[24] V. K. Pustovalov, "Theoretical study of heating of spherical nanoparticle in media by short laser pulses," *Chemical Physics*, vol. 308, no. 1-2, pp. 103–109, 2005.

[25] A. O. Govorov and H. H. Richardson, "Generating heat with metal nanoparticles," *Nano Today*, vol. 2, no. 1, pp. 30–38, 2007.

[26] V. K. Pustovalov, L. G. Astafyeva, and W. Fritzsche, "Selection of thermo-optical parameter of nanoparticles for achievement of their maximal thermal energy under optical irradiation," *Nano Energy*, vol. 2, no. 6, pp. 1137–1141, 2013.

[27] G. Baffou and R. Quidant, "Thermo-plasmonics: using metallic nanostructures as nano-sources of heat," *Laser and Photonics Reviews*, vol. 7, no. 2, pp. 171–187, 2013.

[28] U. Kreibig and M. Vollmer, *Optical Properties of Metal Clusters*, vol. 25 of *Springer Series in Material Science*, Springer, Heidelberg, Germany, 1995.

[29] C. F. Bohren and D. R. Huffman, *Absorption and Scattering of Light by Small Particles*, Wiley, New York, NY, USA, 1983.

[30] V. K. Pustovalov and V. A. Babenko, "Optical properties of gold nanoparticles at laser radiation wavelengths for laser applications in nanotechnology and medicine," *Laser Physics Letters*, vol. 1, no. 10, pp. 516–520, 2004.

[31] P. K. Jain, X. Huang, I. H. El-Sayed, and M. A. El-Sayed, "Review of some interesting surface plasmon resonance-enhanced properties of noble metal nanoparticles and their applications to biosystems," *Plasmonics*, vol. 2, no. 3, pp. 107–118, 2007.

[32] M. G. Blaber, M. D. Arnold, and M. J. Ford, "Search for the ideal lasmonic nanoshell: the effects of surface scattering and alternatives to gold and silver," *Journal of Physical Chemistry C*, vol. 113, no. 8, pp. 3041–3045, 2009.

[33] V. Amendola, O. M. Bakr, and F. Stellacci, "A study of the surface plasmon resonance of silver nanoparticles by the discrete dipole approximation method: effect of shape, size, structure, and assembly," *Plasmonics*, vol. 5, no. 1, pp. 85–97, 2010.

[34] S. A. Joseph, S. Mathew, G. Sharma et al., "Phototermal characterization of nanogold under conditions of resonant excitation and energy transfer," *Plasmonics*, vol. 5, no. 1, pp. 63–68, 2010.

[35] P. R. West, S. Ishii, G. V. Naik, N. K. Emani, V. M. Shalaev, and A. Boltasseva, "Searching for better plasmonic materials," *Laser and Photonics Reviews*, vol. 4, no. 6, pp. 795–808, 2010.

[36] Y. Sonnefraud, A. Koh, D. W. McComb, and S. A. Maier, "Nanoplasmonics: engineering and observation of localized plasmon modes," *Laser and Photonics Reviews*, vol. 6, no. 3, pp. 277–295, 2012.

[37] A. Chen and P. Holt-Hindle, "Platinum-based nanostructured materials: synthesis, properties, and applications," *Chemical Reviews*, vol. 110, no. 6, pp. 3767–3804, 2010.

[38] M. B. Cortie and A. M. McDonagh, "Synthesis and optical properties of hybrid and alloy plasmonic nanoparticles," *Chemical Reviews*, vol. 111, no. 6, pp. 3713–3735, 2011.

[39] M. Rycenga, C. M. Cobley, J. Zeng et al., "Controlling the synthesis and assembly of silver nanostructures for plasmonic applications," *Chemical Reviews*, vol. 111, no. 6, pp. 3669–3712, 2011.

[40] P. B. Johnson and R. W. Christy, "Optical constants of the noble metals," *Physical Review B*, vol. 6, no. 12, pp. 4370–4379, 1972.

[41] E. D. Palik, *Handbook of Optical Constants of Solids*, Academic Press, New York, NY, USA, 1998.

[42] SOPRA N & K database [Electronic resource], http://refractiveindex.info/.

[43] E. Grigor'ev and E. Meilikhov, *Physical Quantities*, Atomizdat, Moscow, Russia, 1991.

[44] F. Kreith and W. Z. Black, *Basic Heat Transfer*, Harper and Row, New York, NY, USA, 1980.

[45] N. C. Bigall, T. Härtling, M. Klose, P. Simon, L. M. Eng, and A. Eychmüller, "Monodisperse platinum nanospheres with adjustable diameters from 10 to 100 nm: synthesis and distinct optical properties," *Nano Letters*, vol. 8, no. 12, pp. 4588–4592, 2008.

Hindawi Publishing Corporation
Journal of Nanoparticles
Volume 2014, Article ID 963961, 8 pages
http://dx.doi.org/10.1155/2014/963961

Review Article

Synthesis of Silver Nanoparticles in Photosynthetic Plants

Ram Prasad

Amity Institute of Microbial Technology, Amity University, Noida, Uttar Pradesh 201303, India

Correspondence should be addressed to Ram Prasad; rpjnu2001@gmail.com

Received 25 July 2014; Accepted 5 August 2014; Published 25 September 2014

Academic Editor: Amir Kajbafvala

Nanobiotechnology is emerging as a field of applied biological science and nanotechnology. Synthesis of nanoparticles is done by various physical and chemical methods but the biological methods are relatively simple, cost-effective, nontoxic, and environmentally friendly methods. The present review focuses on the synthesis of nanoparticles with special emphasis on the use of plants parts for the synthesis process, its applications, and future prospectus.

1. Introduction

Nanotechnology focuses mainly on the design, synthesis and manipulation of structure and size of the particles with dimensions smaller than 100 nm [1]. Nanotechnology combines the principles with physical and chemical procedures to generate nanosized particles with the specific function. Nanotechnology is now creating a growing sense of excitement in the life sciences especially biomedical devices and medicine. Nanoparticles exhibit completely new or improved properties based on specific characteristics such as size, shape, and orientation [2].

The biological synthesis of nanoparticles is a cost-effective and ecofriendly methods and has ability to replace the physical and chemical methods because these methods are toxic and costly. Consequently, nanomaterials have been synthesized using microorganisms and plant extracts. The use of plant extracts for synthesis of nanoparticles is potentially advantageous over microorganisms due to the ease of scaling up the biohazards and elaborate process of maintaining cell cultures [3, 4]. For the last two decades extensive work has been done to develop new drugs from natural products because of the resistance of microorganisms to the existing drugs [1]. Integration of nanoparticles with biological molecules has led to the development of diagnostic devices and important tools in cancer therapy. Biological methods can employ either microorganism cells or plant extracts for nanoparticles production. Biosynthesis of nanoparticles is an exciting recent addition to the large repertoire of nanoparticles synthesis methods and, now, nanoparticles have entered a commercial exploration period. Au, Ag, Zn, and Cu have been used mostly for the synthesis of stable dispersions of nanoparticles, which are useful in areas such as photocatalysis, diodes, piezoelectric devices, fluorescent tubes, laser, sensor, optoelectronics, photography, biological labeling, photonics, and surface-enhanced Raman scattering detection [5–7]. Moreover, the biocompatible and inert nanomaterials have potential applications in cancer diagnosis and therapy. Nowdays, nanotechnology methods are used to enhance the properties of material coatings which are resistant to corrosion, high mechanical, and electrocatalytic properties. These characteristics make nanostructured coatings strong contenders in oil and gas for applications requiring high corrosion protection coupled with high mechanical properties [8, 9].

2. Plants Are Better Synthesizers for Nanoparticles

Biological methods of synthesis have covered the greener synthesis of nanoparticles. These have proven to be better methods due to slower kinetics and they offer better manipulation on control over crystal growth and their stabilization. This has motivated an increase in research on the synthesis routes that allow better control of size and shape for wide variety of nanotechnological applications. The use of environmentally benign materials, namely, plant extract, microorganisms, and

enzymes for the synthesis of AgNPs [10–12] which offer plentiful benefits such as ecofriendliness, biocompatibility, non-toxic, and cost effective method [13].

In the present scenario of the nanotechnology, plants are better synthesizers as compared to the other biological methods due to the abundance of the availability of the plant resources when compared to the other forms of biological resources. Also, plants provide a better platform for nanoparticles synthesis as they are nontoxic chemicals and provide natural capping agents. Additionally, use of plant extracts also reduces the cost of microorganism isolation and culture media enhancing the cost competitive feasibility over nanoparticles synthesis by microorganisms [14, 15]. The advantage of using plants for the synthesis of nanoparticles is that they are easily available and safe to handle and possess a broad variability of secondary metabolites. A number of plants are being currently investigated for their role in the synthesis of nanoparticles. Gold nanoparticles with a size range of 2–20 nm have been synthesized using the live Alfalfa plants. Nanoparticles of Ag, Ni, Co, Zn, and Cu have also been synthesized inside the living plants of *Brassica juncea* (Indian mustard), *Medicago sativa* (Alfalfa), and *Helianthus annuus* (Sunflower). The research group of Gardea-Torresdey from the University of Texas at El Paso first reports on the formation of Ag and Au nanoparticles by living plants *Medicago sativa* and it opened up new and exciting ways to fabricate nanoparticles. It showed connecting link to materials science and biotechnology in the new emerging field of nanobiotechnology [16]. Certain plants are known to accumulate higher concentrations of metals compared to others and such plants are termed as hyperaccumulators. *Brassica juncea* had better metal accumulating ability and later assimilating it as nanoparticles, *Brassica juncea* when hydroponically grown in solution of $AgNO_3$, $Na_3Ag(S_2O_3)_2$, and $Ag(NH_3)_2NO_3$ synthesized AgNPs of 2–35 nm [17]. The concentrations of plant extracts which are aqueous or alcoholic extracts play an important role in maintaining the shape and size of the nanoparticles; for example, an aqueous seed extract of *Jatropha curcas* produced spherical AgNPs of between 15 and 50 nm. The latex of *J. curcas* served as reducing and capping agent in the synthesis of AgNPs of size in between 10 and 20 nm [18]. Ag and AuNPs were synthesized by reducing aqueous solution of $AgNO_3$ and $AuCl_4$ with clove extract, respectively. Sun-dried biomass of *Cinnamomum camphora* leaf extract, when treated with aqueous silver or gold precursors at ambient temperature, produced silver and gold nanoparticles in the range of 55–80 nm. The polyol component and the water-soluble heterocyclic components present in the *C. camphora* were mainly responsible for the reduction and stabilization of silver or chloroaurate in nanoparticles [19]. The reduction of silver ions and stabilization of the AgNPs were thought to occur through the involvement of proteins.

3. Phytofabrication of Nanoparticles

The term phytofabrication indicates the synthesis of the nanoparticles with the help of the plant constituents. Plant constituents include the enzymes and protein contents such as reductases which are involved in the biological reduction of the substrates, such as silver nitrate, aurum chloride, and titanium chloride, into their corresponding nanoparticles such as silver, gold, and titanium. These nanoparticles have a wide range of the applications in the fields of physical, chemical, material, and biological sciences.

Plant extract has been used as reducing and capping agent for the synthesis of nanoparticles. It could be advantageous over microbial synthesis because there is easy culturing and maintenance of the cell. It has been shown that many plants can actively uptake and bioreduce metal ions from soils and solutions during the detoxification process, thereby forming insoluble complexes with the metal ion in the form of nanoparticles. Plant leaf extract had been used for synthesis of silver and gold nanoparticles, which lead to formation of pure metallic nanoparticles of silver and gold [20, 21]. Some of the plant extracts are given in Table 1.

4. Mechanism of Nanoparticles Formation

Still up to date there is no proper mechanism for the synthesis of silver nanoparticles. The proposed hypothetical mechanism behind the synthesis of nanoparticles is an enzymatic reaction in which the plant extract contains the complex of reducing enzymes which reduce the chemicals such as silver nitrate into silver ions and nitrate ions [22].

Plants contain a complex network of antioxidant metabolites and enzymes that work together to prevent oxidative damage to cellular components. It was reported that plants extracts contain biomolecules including polyphenols, ascorbic acid, flavonoids, sterols, triterpenes, alkaloids, alcoholic compounds, polysaccharides, saponins, β-phenylethylamines, glucose and fructose, and proteins/enzymes which could be used as reductant to react with silver ions and therefore used as scaffolds to direct the formation of AgNPs in the solution. Hypothetically, biosynthetic products or reduced cofactors play an important role in the reduction of respective salts to nanoparticles. However, it seems probable that some glucose and ascorbate reduce $AgNO_3$ and $HAuCl_4$ to form nanoparticles [13, 22–24]. In neem leaf broth, terpenoids are the surface active molecules stabilizing the nanoparticles and reaction of the metal ions is possibly facilitated by reducing sugars [25]. *Capsicum annuum* extract also indicated that the proteins which have amine groups played a reducing and controlling role during the formation of AgNPs in the solutions and that the secondary structure of the proteins changed after reaction with silver ions [20]. *Ficus benghalensis* leaf contains antioxidants and polyphenols (flavonoids) and it can also directly scavenge molecular species of active oxygen. Antioxidant action of flavonoids resides mainly in their ability to donate electrons or hydrogen atoms, that is, change keto group to enol form. Proteins, enzymes, phenolics, and other chemicals within plant leaf extract reduce silver salts and also provide excellent tenacity against agglomeration, which can be further studied to understand the mechanism of evolution by biological systems [24, 26].

Table 1: Synthesis of metal nanoparticles by photosynthetic plants.

Plant species	Plant parts	Nanoparticles	Size (nm)	Reference
Sorghum bicolor	Bran	Ag and Fe	—	[3]
Vitex negundo	Leaf	Ag	—	[4]
Ocimum sanctum	Leaf	Ag	—	[15]
Medicago sativa	Leaf	Au and Ag	20–40	[16]
Jatropha curcas	Latex	Ag	10–20	[18]
Cinnamomum camphora	Leaf	Au and Ag	55–80	[19]
Capsicum annuum	Leaf	Ag	15–20	[20]
Allium cepa	Extract	Ag	—	[21]
Azadirachta indica	Leaf	Ag, Au, and Ag/Au bimetallic	50–100	[25]
Avena sativa	Leaf	Au	25–85	[46]
Sesbania drummondii		Au	6–20	[22]
Pelargonium graveolens	Leaf	Ag	16–40	[47]
Aloe vera	Leaf	Ag	15–15.6	[23]
Emblica officinalis	Leaf	Ag and Au	10–20 and 15–25	[48]
Tamarindus indica	Leaf	Au	20–40	[49]
Chilopsis linearis	Leaf	Au	—	[50]
Humulus lupulus	Leaf	Au	—	[51]
Trapa bispinosa	Peel	Ag	—	[52]
Brassica juncea	Leaf	Au	—	[53]
Gliricidia sepium	Leaf	Ag	10–50	[54]
Euphorbia hirta	Leaf and bark	Ag	—	[55]
Argemone mexicana	Leaf	Ag	—	[56]
Boswelliaovali foliolata	Bark and leaf	Ag	—	[57]
Cycas circinalis	Leaf	Ag	2–6	[58]
Nerium indicum	Leaf	Ag	—	[59]
Bacopa monniera	Leaf	Ag	15–120	[60]
Rhizophora apiculata	Leaf	Ag	13–19	[61]
Nicotiana tobaccum	Leaf	Ag	8	[62]
Memecylonedule	Leaf	Ag and Au	50–90 and 10–45	[63]
Saraca indica	Leaf	Ag	13–50	[26]
Bauhinia variegata L.	Leaf	Au	43–145	[64]
Ficus benghalensis	Leaf	Ag	16	[24]
Murraya koenigii	Leaf	Ag	10–25	[65]
Dalbergia sissoo	Leaf	Au and Ag	50–80 and 5–55	[66]
Ipomea carnea	Leaf	Ag	30–130	[67]
Phyllanthus maderaspatensis	Leaf	Ag	59–76	[68]
Santalum album	Leaf	Ag	80–200	[69]
Syzgium cumini	Leaf	Ag	100–160	[70]
Syzgium cumini	Bark	Ag	20–60	[71]

5. Factors Affecting Phytofabrication of Nanoparticles

There is enormous interest in metal nanoparticles because of their unpredicted physical and chemical properties revealed at the nanoscale level. The formation of nanoparticles is depending upon certain physiochemical properties such as temperature, time, pH, optical, concentration of the substrate, and enzyme sources. These factors play an important role in the phytofabrication of nanoparticles such as the shape, size, and distribution. The effect of these factors is explained as follows.

5.1. Effect of Temperature. Temperature is the basic physical factor that affects the formation of the nanoparticles. Vigneshwaran et al. (2006) reported that the silver nanoparticles synthesize by autoclaving the solution of silver nitrate and starch at 15 psi and 121°C temperature [27]. Njagi et al. (2011) reported the synthesis of silver and iron nanoparticles at room temperature using green extracts such as aqueous sorghum bran [3]. Table 2 provides some of the plant extracts which synthesized AgNPs at different temperatures.

The particle size in the solution is performed by several calculations with the computer simulation program "Mie plot v. 3.4" [28]. From the absorbance spectra we can determine

Table 2: Plant extracts which produce AgNPs depending on the temperature.

S. number	Name of the plant	Temperature	Time (hrs)	References
1	*Ocimum sanctum*	Room temperature	48	[27]
2	*Vitex negundo*	Room temperature	48	[4]
3	*Boswellia ovalifoliolata*	50–95°C	1	[57]
4	*Argemone mexicana*	Room temperature	4	[56]
5	*Euphorbia hirta*	Room temperature	7	[59]
6	*Nerium indicum*	Room temperature	7	[59]

size of the particles compared with the one calculated by using Mie theory. One can find the useful information by analyzing the optical spectra; the change in the absorbance shows change of absorbing species in a solution and variations of the quantity of the AgNPs. The position of the peak directly depends upon the size of the nanoparticles [28, 29].

Mie theory:

$$I = I_0 \left(\frac{1 + \cos^2\theta}{2R^2} \right) \left(\frac{2\pi}{\lambda} \right)^4 \left(\frac{n^2 - 1}{n^2 + 2} \right)^2 \left(\frac{d}{2} \right)^6, \quad (1)$$

where R is the distance between the particle and the observer, θ is the scattering angle, n is the refractive index of the particle, and d is the diameter of the particle.

The stability of the nanoparticles also depends on the temperature, the AgNPs which are formed are maintained at the temperature between 18 and 25°C for two to three months, and these solutions are stable at these temperature ranges [28].

5.2. Effect of Concentration of the Substrate and the Reducing Agents. The effect of pH can be better understood by the preparation of nanoparticles from the chemical methods such as preparation by Tollens' reagent, that is, ammoniacal silver nitrate, which reduces the carboxyl group of the sugar substrate, such as glucose and ribose; the size of the nanoparticles depends on the concentration of ammonium; in this reaction $Ag(NH_3)_2^+$ is a stable complex ion resulting from ammonia's strong affinity for Ag^+; therefore the ammonia concentration and nature of the reductant must play a major role in controlling the AgNPs [30].

5.3. Effect of pH. pH is physical factor that affects the size and the distribution of the nanoparticles [30, 31]. The difference in structure of monosaccharide and disaccharides influences the particle size with disaccharides giving on average smaller particles than monosaccharide at pH 11.5. Furthermore, particles obtained at pH 11.5 were smaller than those at pH 12.5. Polydispersity also decreased by lowering the pH [31].

5.4. Effect of Time. The synthesis of nanoparticles depends upon the rate of the reaction and the stability of the nanoparticles depends upon the reaction time. Synthesis of AgNPs revealed that glucose was able to reduce Ag^+ ions to Ag^0 and through this reaction, glucose can be oxidized to gluconic acid. The gradual formation of AgNPs was investigated by UV visible spectroscopy, which has proven to be a useful spectroscopic method for the detection of prepared NPs over time. In UV visible spectra, the AgNPs can be shown by a SPR peak at around 400 nm, but a small shift (blue shift or red shift) in the wavelength of the peak could be related to obtaining Ag-NPs in different shapes, sizes, or solvent dependences of prepared AgNPs [32]. Concerning the colloid stability of the prepared silver hydrosols, it was found to be strongly dependent on particle size. The colloids with particle sizes below 100 nm, prepared at lower ammonia concentrations, are stable for several months, while larger particles reveal a high level of instability as a result of the relatively quick sedimentation process. The colloid stability of silver particles prepared at lower ammonia concentrations is well documented by the time dependencies of absorption spectra, exhibiting a sharp plasmon absorption maximum even three months after preparation [33].

6. Applications

Nanoparticles application in catalysis, sensors, and medicine depends critically on the size, shape, and composition of the particles. Thus, different routes leading to the synthesis of nanoparticles of various shapes and sizes have extended the choice of properties that can be obtained. Various applications of nanoparticles are listed below.

6.1. Environmental Sciences. Due to the large surface area and relatively high surface energy, once released into the environment, AgNPs transformation takes place such as oxidation, aggregation, sulfurization, and chlorination. Also, environmental transformation related AgNP toxicity and stability should be investigated. Because environmental systems are always variable, AgNPs have limited stability and tendency of being easily oxidized and releasing silver ion; it is hard to predict the fate and transport of AgNPs. Furthermore, in the presence of dissolved organic matter, dissolved silver ion can also be reduced to AgNPs. Previous study revealed that silver ion release is mediated by dissolved oxygen and protons, but present study revealed that the dissolved oxygen would generate superoxide anion in natural waters under sunlight and significantly promote the reformation of AgNPs. Given their complicated behaviour in the environment, we must make great effort to broaden our knowledge of the transformation of AgNPs so as to correctly forecast their environmental and human health risks [34]. Photodynamic cancer therapy is based on the destruction of the cancer cells by laser generated atomic oxygen, which is cytotoxic [35].

6.2. Antibacterial Activity. The AgNPs are well known for their excellent antibacterial ability and superior physical properties and are widely used in a growing number of applications ranging from home disinfectants and medical devices to water purificants. The AgNPs have been an effective biocide against broad-spectrum bacteria including both Gram-negative and Gram-positive bacteria. Silver is known for antimicrobial properties and has been used in the medical field and also has been shown to prevent HIV from binding to host cells. AgNPs can be exploited in medicine and pharmacy for dental materials, burn treatments, coating stainless steel materials, and sunscreen lotions [36]. In general, therapeutic effects of AgNPs depend on important aspects, including particle size (surface area and energy), particle shape (catalytic activity), particle concentration (therapeutic index), and particle charge (oligodynamic quality) [27]. Mechanisms of antimicrobial effects of AgNPs are still not fully understood, but several studies have revealed that AgNPs may attach to the negatively charged bacterial cell wall and rupture it, which leads to denaturation of protein and finally cell death. The cell death due is also related to uncoupling of oxidative phosphorylation, induction of free radical formation, interference with respiratory chain at cytochrome C level, interaction with protein thiol groups and membrane bound enzymes. Additionally, interaction with phosphorus and sulphur containing compounds such as DNA and protein. AgNPs act as an antibacterial, antiviral, and antifungal agent when incorporated in coatings, nanofiber, first aid bandages, plastics soap, and textiles, in self-cleaning fabrics, and as conductive filler [27]. In hospitals, infection is the most common complication and cause of death in patients. Therefore, antibacterial effects of AgNPs have been incorporated into various medical applications. Plastic catheters coated with AgNPs prevent biofilm formation from *Escherichia coli, Enterococcus faecalis, Staphylococcus aureus, Candida albicans, Staphylococci,* and *Pseudomonas aeruginosa* and also show significant *in vitro* antimicrobial activity [37]. Microorganisms that are exposed to pollutants in the environment such as metal ions have remarkable ability to fight with metal stress. These metal-microbe interactions have already found to be beneficial role in nanobiotechnological applications.

6.3. Nanobiosensors. Nanoparticles are excellent labels for the biosensors because they can be detected by numerous techniques, such as optic absorption fluorescence and electric conductivity. Using the surface plasmon resonance effect the AgNPs gain a very high sensitivity and the measurements can be conducted in real time [38]. The unique physicochemical properties of metals at the nanoscale have led to the development of a wide variety of biosensors, such as nanobiosensors for point of care disease diagnosis, nanoprobes for *in vivo* sensing/imaging, cell tracking, and monitoring disease pathogenesis or therapy monitoring, and other nanotechnology-based tools that benefit scientific research on basic biology [35].

6.4. Agricultural Engineering. Agriculture is the backbone of most developing countries, with more than 60% of the population dependent on it for their occupation. Nanosized lignocellulosic materials have been obtained from crops and trees which had opened up a new market for innovative and value added nanosized materials and products. These can be applied in food and other packaging, construction, and transportation vehicle body structures. Nanofertilizer, nanopesticides including nanoherbicides, nanocoating, and smart delivery system for plant nutrients are being used extensively in agriculture with several industries making formulations which contain 100–250 nm nanoparticles that are more soluble in water thus increasing their activity [39]. Nanofertilizers are able to synchronize the release of nutrients with their plant uptake, thus avoiding nutrient losses and reducing the risks of groundwater pollution. Additionally, the nanofertilizers should release the nutrients on demand while preventing them from prematurely converting into chemical/gaseous forms that cannot be absorbed by plants. This can be achieved by preventing nutrients from interacting with soil, water, and microorganisms and releasing nutrients only when they can be directly internalized by the plant [40, 41].

6.5. Nanoparticles Impregnated Fabrics for Clinical Clothing. Because nanoparticles possess a large surface area to volume ratio as well as a high surface energy the use of nanoparticles could provide high durability for treated fabrics that lead to an increase in durability of the textile functions. The film thickness is in the range of 50–80 nm and acts as a catalyst to self-cleaning the fabric. Titanium nanoparticles with a smooth surface may be used as an antiadhesive coating for windows or spectacles lenses and application in textiles. AgNPs have been used to produce self-cleaning or antiodour clothes, furniture textiles, kitchen cloths, towels, antibacterial wound dressings, patient dresses, bed lines or reusable surgical gloves and masks, protective face masks, suits against biohazards, cosmetic products, ultrahydrophobic fabrics with potential applications in the production of highly water repellent materials, and sportswear. Freeman et al. (2012) investigated the effect of silver impregnation of surgical scrub suits on surface bacterial contamination during use in a veterinary hospital. It was observed that silver-impregnated scrubs had significantly lowered bacterial colony counts compared with polyester/cotton scrubs. The results showed that silver impregnation appeared to be effective in reducing bacterial contamination of scrubs during use in a veterinary hospital [42–45].

7. Conclusions and Future Prospects

Plants as a biological system for the fabrication of nanoparticles have emerged as simple, cost-effective, ecofriendly, and rapid technique. They could be a more efficient biological system than microorganisms along with physiochemical methods employed for the fabrication process. Nanoparticles of Ag, Au, and Pt have been successfully prepared using a simple and efficient green chemistry methodology.

Nanoparticles had a wide application in the field molecular research to study the nucleic acid structures and their

functions in the intact of the cell. Nanoparticles also act as biological markers included in the proteins, nucleic acids, hormones, and all other biological active molecules. The application of nanoparticles in the agriculture opens a new scope for the preparation of biologically degradable synthetic pesticides and having the target of the pesticide action for the agricultural pests. Nanoparticles suspensions with different ranges of nanoparticles had different mode of application in the agricultural biotechnology for the preparation of disease resistant and drought resistance plants in the future which can replace the classical experiments.

The antimicrobial activity of the nanoparticles had a wide scope in the preparation of target based drug delivery and clinical diagnostics system. The identification of the specific mechanism of the AgNPs inhibition of the microbial growth or the lethal effect provides major application in the medicine, environment, soil fertility, and water quality. Moreover, the synthesis of nanoparticles with different sizes and shapes is the basic challenging task in the green synthesis of nanoparticles; this requires a basic understanding of the nuclei formation and the influence of reaction species in nuclei morphology, but still there is dormancy about the actual mechanism of the nanoparticles synthesis from the biological mode of synthesis.

Nanobiotechnology has emerged as the present and the future technology of the era, with profound variety of applications that include fields such as quantum dots, opto-electronics, medicine, therapeutics, biosensors, and many more.

Conflict of Interests

The author declares that he has no conflict of interests.

References

[1] N. Savithramma, M. L. Rao, K. Rukmini, and P. S. Devi, "Antimicrobial activity of silver nanoparticles synthesized by using medicinal plants," *International Journal of ChemTech Research*, vol. 3, no. 3, pp. 1394–1402, 2011.

[2] Z. Sadowski, *Biosynthesis and Application of Silver and AuNPs*, Wroclaw University of Technology, 2009.

[3] E. C. Njagi, H. Huang, L. Stafford et al., "Biosynthesis of iron and silver nanoparticles at room temperature using aqueous *Sorghum* bran extracts," *Langmuir*, vol. 27, no. 1, pp. 264–271, 2011.

[4] M. Zargar, A. A. Hamid, F. A. Bakar et al., "Green synthesis and antibacterial effect of silver nanoparticles using *Vitex negundo*," *Molecules*, vol. 16, no. 8, pp. 6667–6676, 2011.

[5] J. Jain, S. Arora, J. M. Rajwade, P. Omray, S. Khandelwal, and K. M. Paknikar, "Silver nanoparticles in therapeutics: development of an antimicrobial gel formulation for topical use," *Molecular Pharmaceutics*, vol. 6, no. 5, pp. 1388–1401, 2009.

[6] A. Kajbafvala, M. R. Shayegh, M. Mazloumi et al., "Nanostructure sword-like ZnO wires: rapid synthesis and characterization through a microwave-assisted route," *Journal of Alloys and Compounds*, vol. 469, no. 1-2, pp. 293–297, 2009.

[7] A. Kajbafvala, H. Ghorbani, A. Paravar, J. P. Samberg, E. Kajbafvala, and S. K. Sadrnezhaad, "Effects of morphology on photocatalytic performance of Zinc oxide nanostructures synthesized by rapid microwave irradiation methods," *Superlattices and Microstructures*, vol. 51, no. 4, pp. 512–522, 2012.

[8] A. Kajbafvala, S. Zanganeh, E. Kajbafvala, H. R. Zargar, M. R. Bayati, and S. K. Sadrnezhaad, "Microwave-assisted synthesis of narcis-like zinc oxide nanostructures," *Journal of Alloys and Compounds*, vol. 497, no. 1-2, pp. 325–329, 2010.

[9] A. Kajbafvala, J. P. Samberg, H. Ghorbani, E. Kajbafvala, and S. K. Sadrnezhaad, "Effects of initial precursor and microwave irradiation on step-by-step synthesis of zinc oxide nano-architectures," *Materials Letters*, vol. 67, no. 1, pp. 342–345, 2012.

[10] N. Saifuddin, C. W. Wong, and A. A. N. Yasumira, "Rapid biosynthesis of silver nanoparticles using culture supernatant of bacteria with microwave irradiation," *E-Journal of Chemistry*, vol. 6, no. 1, pp. 61–70, 2009.

[11] V. C. Verma, R. N. Kharwar, and A. C. Gange, "Biosynthesis of antimicrobial silver nanoparticles by the endophytic fungus Aspergillus clavatus," *Nanomedicine*, vol. 5, no. 1, pp. 33–40, 2010.

[12] I. Willner, B. Basnar, and B. Willner, "Nanoparticle-enzyme hybrid systems for nanobiotechnology," *FEBS Journal*, vol. 274, no. 2, pp. 302–309, 2007.

[13] P. Mohanpuria, N. K. Rana, and S. K. Yadav, "Biosynthesis of nanoparticles: technological concepts and future applications," *Journal of Nanoparticle Research*, vol. 10, no. 3, pp. 507–517, 2008.

[14] V. K. Sharma, R. A. Yngard, and Y. Lin, "Silver nanoparticles: green synthesis and their antimicrobial activities," *Advances in Colloid and Interface Science*, vol. 145, no. 1-2, pp. 83–96, 2009.

[15] G. Singhal, R. Bhavesh, K. Kasariya, A. R. Sharma, and R. P. Singh, "Biosynthesis of silver nanoparticles using *Ocimum sanctum* (Tulsi) leaf extract and screening its antimicrobial activity," *Journal of Nanoparticle Research*, vol. 13, no. 7, pp. 2981–2988, 2011.

[16] J. L. Gardea-Torresdey, E. Gomez, J. R. Peralta-Videa, J. G. Parsons, H. Troiani, and M. Jose-Yacaman, "Alfalfa sprouts: a natural source for the synthesis of silver nanoparticles," *Langmuir*, vol. 19, no. 4, pp. 1357–1361, 2003.

[17] T. C. Prathna, N. Chandrasekaran, A. M. Raichur, and A. Mukherjee, "Biomimetic synthesis of silver nanoparticles by *Citrus limon* (lemon) aqueous extract and theoretical prediction of particle size," *Colloids and Surfaces B: Biointerfaces*, vol. 82, no. 1, pp. 152–159, 2011.

[18] H. Bar, D. K. Bhui, G. P. Sahoo, P. Sarkar, S. P. De, and A. Misra, "Green synthesis of silver nanoparticles using latex of *Jatropha curcas*," *Colloids and Surfaces A: Physicochemical and Engineering Aspects*, vol. 339, no. 1–3, pp. 134–139, 2009.

[19] J. Huang, Q. Li, D. Sun et al., "Biosynthesis of silver and gold nanoparticles by novel sundried *Cinnamomum camphora* leaf," *Nanotechnology*, vol. 18, no. 10, Article ID 105104, 2007.

[20] S. Li, Y. Shen, A. Xie et al., "Green synthesis of silver nanoparticles using *Capsicum annuum* L. extract," *Green Chemistry*, vol. 9, no. 8, pp. 852–858, 2007.

[21] A. Saxena, R. M. Tripathi, and R. P. Singh, "Biological synthesis of silver nanoparticles by using onion (*Allium cepa*) extract and their antibacterial activity," *Digest Journal of Nanomaterials and Biostructures*, vol. 5, no. 2, pp. 427–432, 2010.

[22] N. C. Sharma, S. V. Sahi, S. Nath, J. G. Parsons, J. L. Gardea-Torresdey, and P. Tarasankar, "Synthesis of plant-mediated gold nanoparticles and catalytic role of biomatrix-embedded nanomaterials," *Environmental Science and Technology*, vol. 41, no. 14, pp. 5137–5142, 2007.

[23] S. P. Chandran, M. Chaudhary, R. Pasricha, A. Ahmad, and M. Sastry, "Synthesis of gold nanotriangles and silver nanoparticles using *Aloe vera* plant extract," *Biotechnology Progress*, vol. 22, no. 2, pp. 577–583, 2006.

[24] A. Saxena, R. M. Tripathi, F. Zafar, and P. Singh, "Green synthesis of silver nanoparticles using aqueous solution of *Ficus benghalensis* leaf extract and characterization of their antibacterial activity," *Materials Letters*, vol. 67, no. 1, pp. 91–94, 2012.

[25] S. S. Shankar, A. Rai, A. Ahmad, and M. Sastry, "Rapid synthesis of Au, Ag, and bimetallic Au core-Ag shell nanoparticles using Neem (*Azadirachta indica*) leaf broth," *Journal of Colloid and Interface Science*, vol. 275, no. 2, pp. 496–502, 2004.

[26] R. M. Tripathi, D. Rana, A. Shrivastava, R. P. Singh, and B. R. Shrivastav, "Biogenic synthesis of silver nanoparticles using Saraca indica leaf extract and evaluation of their antibacterial activity," *Nano Biomedicine and Engineering*, vol. 5, no. 1, pp. 50–56, 2013.

[27] N. Prabhu, D. T. Raj, K. Y. Gowri, S. A. Siddiqua, and D. J. P. Innocent, "Synthesis of silver phyto nanoparticles and their antibacterial efficacy," *Digest Journal of Nanomaterials and Biostructures*, vol. 5, no. 1, pp. 185–189, 2010.

[28] S. Asta, P. Judita, P. Igoris, and T. Sigitas, "Investigation of silver nanoparticles formation kinetics during reduction of silver nitrate with sodium citrate," *Materials Science*, vol. 15, pp. 1392–1320, 2009.

[29] S. Asta, P. Igoris, P. Judita, J. Algimantas, and G. Asta, "Analysis of silver nanoparticles produced by chemical reduction of silver salt solution," *Materials Science*, vol. 12, pp. 1392–1320, 2006.

[30] L. Kvítek, A. Panáček, J. Soukupová et al., "Effect of surfactants and polymers on stability and antibacterial activity of silver nanoparticles (NPs)," *Journal of Physical Chemistry*, vol. 112, no. 15, pp. 5825–5834, 2008.

[31] V. K. Sharma, R. A. Yngard, and Y. Lin, "Silver nano-particles: green synthesis and their antimicrobial activities," *Journal of Colloid and Interface Science*, vol. 145, no. 1-2, pp. 83–96, 2009.

[32] M. Darroudi, M. B. Ahmad, A. H. Abdullah, and N. A. Ibrahim, "Green synthesis and characterization of gelatin-based and sugar-reduced silver nanoparticles," *International Journal of Nanomedicine*, vol. 6, no. 1, pp. 569–574, 2011.

[33] L. Kvítek, R. Prucek, A. Panáček, R. Novotný, J. Hrbác, and R. Zbořil, "The influence of complexing agent concentration on particle size in the process of SERS active silver colloid synthesis," *Journal Material Chemistry*, vol. 15, pp. 1099–1107, 2005.

[34] S.-J. Yu, Y.-G. Yin, and J.-F. Liu, "Silver nanoparticles in the environment," *Environmental Sciences: Processes and Impacts*, vol. 15, no. 1, pp. 78–92, 2013.

[35] G. Doria, J. Conde, B. Veigas et al., "Noble metal nanoparticles for biosensing applications," *Sensors*, vol. 12, no. 2, pp. 1657–1687, 2012.

[36] N. Durán, P. D. Marcato, G. I. H. de Souza, O. L. Alves, and E. Esposito, "Antibacterial effect of silver nanoparticles produced by fungal process on textile fabrics and their effluent treatment," *Journal of Biomedical Nanotechnology*, vol. 3, no. 2, pp. 203–208, 2007.

[37] D. Roe, B. Karandikar, N. Bonn-Savage, B. Gibbins, and J. Roullet, "Antimicrobial surface functionalization of plastic catheters by silver nanoparticles," *Journal of Antimicrobial Chemotherapy*, vol. 61, no. 4, pp. 869–876, 2008.

[38] A. J. Haes, A. D. McFarland, and R. P. van Duyne, "Nanoparticle optics: sensing with nanoparticle arrays and single nanoparticles," *The International Society for Optical Engineering*, vol. 5223, pp. 197–207, 2003.

[39] L. Marchiol, "Synthesis of metal nanoparticles in living plants," *Italian Journal of Agronomy*, vol. 7, no. 3, pp. 274–282, 2012.

[40] R. Prasad, V. Kumar, and K. S. Prasad, "Nanotechnology in sustainable agriculture: present concerns and future aspects," *African Journal of Biotechnology*, vol. 13, no. 6, pp. 705–713, 2014.

[41] Suman, R. Prasad, V. K. Jain, and A. Varma, "Role of nanomaterials in symbiotic fungus growth enhancement," *Current Science*, vol. 99, no. 9, pp. 1189–1191, 2010.

[42] J. Lee, Y. Huh, Y. Jun et al., "Artificially engineered magnetic nanoparticles for ultra-sensitive molecular imaging," *Nature Medicine*, vol. 13, no. 1, pp. 95–99, 2007.

[43] R. Karthik, I. K. Swaminatha, K. K. Mark et al., "Ultrahydrophobic textiles using nanoparticles: lotus approach," *Journal of Engineered Fibers and Fabrics*, vol. 3, no. 4, pp. 1–14, 2008.

[44] A. M. Sherik and K. M. Nabulsi, "Applications of nanotechnology in oil and gas," *International Journal of Nano and Biomaterials*, vol. 2, no. 1–5, pp. 409–415, 2009.

[45] A. I. Freeman, L. J. Halladay, and P. Cripps, "The effect of silver impregnation of surgical scrub suits on surface bacterial contamination," *Veterinary Journal*, vol. 192, no. 3, pp. 489–493, 2012.

[46] S. S. Shankar, A. Rai, A. Ahmad, and M. Sastry, "Controlling the optical properties of lemongrass extract synthesized gold nanotriangles and potential application in infrared-absorbing optical coatings," *Chemistry of Materials*, vol. 17, no. 3, pp. 566–572, 2005.

[47] S. S. Shankar, A. Ahmad, and M. Sastry, "Geranium leaf assisted biosynthesis of silver nanoparticles," *Biotechnology Progress*, vol. 19, no. 6, pp. 1627–1631, 2003.

[48] B. Ankamwar, C. Damle, A. Ahmad, and M. Sastry, "Biosynthesis of gold and silver nanoparticles using *Emblica officinalis* fruit extract, their phase transfer and transmetallation in an organic solution," *Journal of Nanoscience and Nanotechnology*, vol. 5, no. 10, pp. 1665–1671, 2005.

[49] G. F. Paciotti, L. Myer, D. Weinreich et al., "Colloidal gold: a novel nanoparticle vector for tumor directed drug delivery," *Drug Delivery*, vol. 11, no. 3, pp. 169–183, 2004.

[50] B. Ankamwar, M. Chaudhary, and M. Sastry, "Gold nanotriangles biologically synthesized using tamrind leaf extract and potential application in vapor sensing synthetic reaction," *Inorganic Metal Organic Nano Metal Chemistry*, vol. 35, no. 1, pp. 19–26, 2005.

[51] A. Rai, A. Singh, A. Ahmad, and M. Sastry, "Role of halide ions and temperature on the morphology of biologically synthesized gold nanotriangles," *Langmuir*, vol. 22, no. 2, pp. 736–741, 2006.

[52] S. Pandey, A. Mewada, M. Thakur et al., "Rapid biosynthesis of silver nanoparticles by exploiting the reducing potential of *Trapa bispinosa* peel extract," *Journal of Nanoscience*, vol. 2013, Article ID 516357, 9 pages, 2013.

[53] A. E. Lamb, W. N. Anderson, and R. G. Haverkamp, "The induced accumulation of gold in the plants *Brassica juncea*, *Berkheyacoddii* and *chicory*," *Chemistry in New Zealand*, vol. 9, pp. 34–36, 2001.

[54] W. Raut Rajesh, R. Lakkakula Jaya, S. Kolekar Niranjan, D. Mendhulkar Vijay, and B. Kashid Sahebrao, "Phytosynthesis of silver nanoparticle using *Gliricidia sepium* (Jacq.)," *Current Nanoscience*, vol. 5, no. 1, pp. 117–122, 2009.

[55] E. K. Elumalai, T. N. V. K. V. Prasad, J. Hemachandran, S. Viviyan Therasa, T. Thirumalai, and E. David, "Extracellular synthesis of silver nanoparticles using leaves of *Euphorbia hirta* and their antibacterial activities," *Journal of Pharmaceutical Sciences and Research*, vol. 2, no. 9, pp. 549–554, 2010.

[56] A. Singh, D. Jain, M. K. Upadhyay, N. Khandelwal, and H. N. Verma, "Green synthesis of silver nanoparticles using *Argemone mexicana* leaf extract and evaluation of their antimicrobial activities," *Digest Journal of Nanomaterials and Biostructures*, vol. 5, no. 2, pp. 483–489, 2010.

[57] S. Ankanna, T. N. V. K. V. Prasad, E. K. Elumalai, and N. Savithramma, "Production of biogenic silver nanoparticles using *Boswellaovali foliolata* stem bark," *Digest Journal of Nanomaterials and Biostructures*, vol. 5, no. 2, pp. 369–372, 2010.

[58] A. K. Jha and K. Prasad, "Green synthesis of silver nanoparticles using cycas leaf," *International Journal of Green Nanotechnology: Physics and Chemistry*, vol. 1, no. 2, pp. P110–P117, 2010.

[59] M. Mano Priya, B. Karunai Selvi, and J. A. John Paul, "Green synthesis of silver nanoparticles from the leaf extracts of *Euphorbia hirta* and *Nerium indicum*," *Digest Journal of Nanomaterials and Biostructures*, vol. 6, no. 2, pp. 869–877, 2011.

[60] B. Mahitha, B. Deva Prasad, G. R. Raju et al., "Biosynthesis, characterization and antimicrobial studies of AgNP's extract from *Bacopa monniera* whole plant," *Digest Journal of Nanomaterials and Biostructures*, vol. 6, pp. 135–142, 2011.

[61] J. J. Antony, P. Sivalingam, D. Siva et al., "Comparative evaluation of antibacterial activity of silver nanoparticles synthesized using *Rhizophora apiculata* and glucose," *Colloids and Surfaces B: Biointerfaces*, vol. 88, no. 1, pp. 134–140, 2011.

[62] K. S. Prasad, D. Pathak, A. Patel et al., "Biogenic synthesis of silver nanoparticles using *Nicotiana tobaccum* leaf extract and study of their antibacterial effect," *African Journal of Biotechnology*, vol. 9, no. 54, pp. 8122–8130, 2011.

[63] T. Elavazhagan and K. D. Arunachalam, "Memecylon edule leaf extract mediated green synthesis of silver and gold nanoparticles," *International Journal of Nanomedicine*, vol. 6, pp. 1265–1278, 2011.

[64] V. Kumar and S. K. Yadav, "Synthesis of variable shaped gold nanoparticles in one solution using leaf extract of *Bauhinia variegata* L," *Digest Journal of Nanomaterials and Biostructures*, vol. 6, no. 4, pp. 1685–1693, 2011.

[65] L. Christensen, S. Vivekanandhan, M. Misra, and A. K. Mohanty, "Biosynthesis of silver nanoparticles using *Murraya koenigii* (curry leaf): an investigation on the effect of broth concentration in reduction mechanism and particle size," *Advanced Materials Letters*, vol. 2, no. 6, pp. 429–434, 2011.

[66] C. Singh, R. K. Baboota, P. K. Naik, and H. Singh, "Biocompatible synthesis of silver and gold nanoparticles using leaf extract of *Dalbergia sissoo*," *Advanced Materials Letters*, vol. 3, no. 4, pp. 279–285, 2012.

[67] S. C. G. K. Daniel, B. B. Nazeema, M. Harshiny et al., "*Ipomea carnea*-based silver nanoparticle synthesis for antibacterial activity against selected human pathogens," *Journal of Experimental Nanoscience*, pp. 1–13, 2012.

[68] A. Annamalai, V. L. P. Christina, and P. T. V. Lakshmi, "Green synthesis and characterisation of AgNPs using aqueous extract of *Phyllanthus maderaspatensis* L.," *Journal of Experimental Nanoscience*, vol. 9, no. 2, pp. 113–119, 2012.

[69] V. S. Swamy and R. Prasad, "Green synthesis of silver nanoparticles from the leaf extract of *Santalum album* and its antimicrobial activity," *Journal of Optoelectronic and Biomedical Materials*, vol. 4, no. 3, pp. 53–59, 2012.

[70] R. Prasad, V. Satyanarayana Swamy, K. S. Prasad, and A. Varma, "Biogenic synthesis of silver nanoparticles from the leaf extract of *Syzygium cumini* (L.) and its antibacterial activity," *International Journal of Pharma and Bio Sciences*, vol. 3, no. 4, pp. 745–752, 2012.

[71] R. Prasad and V. S. Swamy, "Antibacterial activity of silver nanoparticles synthesized by bark extract of *Syzygium cumini*," *Journal of Nanoparticles*, vol. 2013, Article ID 431218, 6 pages, 2013.

Hindawi Publishing Corporation
Journal of Nanoparticles
Volume 2014, Article ID 689419, 6 pages
http://dx.doi.org/10.1155/2014/689419

Research Article

Biogenic Synthesis of Silver Nanoparticles Using *Scenedesmus abundans* and Evaluation of Their Antibacterial Activity

Nafe Aziz,[1] Tasneem Fatma,[2] Ajit Varma,[1] and Ram Prasad[1]

[1] *Amity Institute of Microbial Technology, Amity University, Noida, Uttar Pradesh 201303, India*
[2] *Department of Bio-Sciences, Jamia Millia Islamia, Jamia Nagar, New Delhi 110025, India*

Correspondence should be addressed to Ram Prasad; rpjnu2001@gmail.com

Received 6 August 2014; Revised 23 August 2014; Accepted 25 August 2014; Published 14 September 2014

Academic Editor: Amir Kajbafvala

Silver nanoparticle (AgNP) was synthesized using the cell free extract of *Scenedesmus abundans* with $AgNO_3$. The synthesized silver nanoparticles were characterized by UV-visible spectroscopy, dynamic light scattering (DLS), scanning electron microscopy (SEM), and Photoluminescence. Bioreduction of Ag^+ ions showed a gradual change in the colour of the extract and nanoparticles were synthesized having the range of 420–440 nm under UV-visible spectrum. The antibacterial efficacy was assessed against pathogenic bacteria *E. coli, Klebsiella pneumoniae,* and *Aeromonas hydrophila*. The present study revealed that the AgNPs prepared from *Scenedesmus abundans* show antibacterial efficacy against the test pathogens. The bioaccumulation of silver particles makes the organism potential candidate for ecofriendly silver biorecovery system and *S. abundans* can be used as a source of silver nanoparticles.

1. Introduction

Nanoparticles are gaining the interest in it due to their unique characteristics such as electronic, mechanical, optical, magnetic, chemical properties [1, 2] and high surface to volume ratio which differ significantly with bulk materials [3, 4]. In nanotechnology, the formation of nanoparticles has the method that mainly involved the process of separation deformation and transformation of materials to atoms or molecules [5]. The synthesis of nanoparticles can occur by different methods such as dry, wet, and through computational nanotechnology. Basically dry nanotechnology concentrates on surface science, physical chemistry, and structure of organic and inorganic materials. Wet nanotechnology deals with biological systems that exist primarily in water base system, such as enzymes, membranes, and cellular components. Computational nanotechnology comprises modelling and stimulation of complex nanometer. The novel metal nanoparticles had attended much interest due to their vast applications in diverse areas such as optoelectronics, cosmetics, photo catalysis, diodes, piezoelectric devices, fluorescent tubes, laser, sensor, photography, biological labeling, photonics coatings, packaging, and drug delivery system [5–9]. Now a days nanomaterials are produced by industries for commercial application having many benefits. Green synthesis of nanoparticles attracts many researchers and industries. Many microorganisms are utilized for the synthesis of nanoparticles intracellularly as well as extracellularly [10–13]. The mechanism behind the synthesis of silver nanoparticles was not known before but it was hypothesized later that the enzymes NADH-dependent nitrate reductase were used for the reduction of silver ions [14]. Biosynthesis of nanoparticles has been reported by many photoautotrophic microorganisms such as cyanobacteria, eukaryotic algae, and fungi, and even in plants [15–20] there are various other processes such as bioremediation, bioleaching, biological metal recovery, and biomineralization which have been done by biological system [21]. Biologically synthesized nanoparticles have proved to be better than the chemically synthesized nanoparticles due to slower kinetics, which offer a better control over crystal growth and reduced investment involved in production [22]. Among the biological materials, algae could be considered as "bionanofactories" because the live and dead dried biomass can be utilized for synthesis of

metallic nanoparticles. Both unicellular and multicellular organisms have been known to produce intracellular or extracellular inorganic materials as well as high growth rate and high biomass productivity with a less cultivation time. Besides, they have been proved as a potential organism for heavy metal detoxification and production of commercially important metabolites, including biodiesel production [23]. As algae have diverse groups of organisms and make up the lower phylogenetic echelons of the plant kingdom and contain many characteristics of the higher plants [24]. Algae execute about 50% of the photosynthesis on earth planet and thus are involved in supporting the biosphere [25]. *S. abundans* required smaller amount of sunlight, CO_2, and minerals for growth, because of these properties it is a suitable organism for the biosynthesis of nanoparticles.

This study reported that the nanoparticles synthesis by using the fresh water green microalga *S. abundans* extract and characterized by UV-vis spectroscopy and morphological structure which were characterized by SEM. The antimicrobial activity of silver nanoparticles against pathogenic bacteria was studied as well.

2. Material and Methods

2.1. Chemicals, Culture, and Growth Conditions. All analytical reagents and media components were purchased from HiMedia (Mumbai, India) and Sigma Chemicals (St. Louis, MO, USA). *Scenedesmus abundans* (NCIM 2897) culture procured from National Centre for Industrial Microorganism (NCIM), Pune. Culture was grown on Bold's Basal Medium which is composed of (mgL^{-1}): $NaNO_3$ (250), K_2HPO_4 (75), KH_2PO_4 (175), $CaCl_2{\cdot}2H_2O$ (25), $MgSO_4{\cdot}7H_2O$ (75), NaCl (25), $ZnSO_4{\cdot}7H_2O$ (882), $MnCl_2{\cdot}4H_2O$ (144), $Co(NO_3)_2{\cdot}6H_2O$ (49), MoO_3 (71), H_3BO_3 (114), EDTA·Na_2 (500), KOH (310), $FeSO_4{\cdot}7H_2O$ (498), and conc. H_2SO_4 (1 mL) at 24 ± 1°C in a continuous illumination with cool white fluorescent tubes (Philips 40 W) having irradiance of 50 $Me/m^2/s$ in a 16 h : 8 h light/dark regime. The bacterial pathogens used as *E. coli*, *Klebsiella pneumoniae*, and *Aeromonas hydrophila* were grown on Muller Hinton agar (MHA) at 37°C for overnight incubation for further use and stored at 4°C.

2.2. Biosynthesis of Silver Nanoparticles. Cell free extract was prepared from *Scenedesmus abundans* for nanoparticle synthesis. It was grown in Bold's basal medium and after 14 days of incubation pellets were separated by centrifugation at 10,000 rpm for 10 minutes and the pellets were washed with sterile double distilled water in order to remove the traces of media. Pellets were dried at 80°C and dry weight measurement was done. 1 gm of algal powder into 30 mL of double distilled water was added and boiled at 100°C for 20 minutes in an Erlenmeyer flask then centrifuged at 5000 rpm for 10 min after cooling. Biosynthesis of AgNP was done by adding 10 mL of cell free extract in 90 mL of 1 mM $AgNO_3$ and incubated at room temperature for 48 hours. The change in colour indicates AgNP synthesis.

2.3. Characterization of Synthesized Silver Nanoparticles. The bioreduction of AgNPs was monitored using Double Beam UV-Vis spectrophotometer (Labtronics) in 1 cm path length quartz cuvette having spectral range of 300 and 700 nm at different time intervals. *Dynamic Light Scattering* was used to determine hydrodynamic sizes, polydispersities, and aggregation effects of colloidal samples. Size distribution of synthesized AgNPs was measured using a Nano Zetasizer system (Malvern Instruments). The particular parameters used such as measurement temperature of 25°C, medium viscosity of 0.8872 mPa·s, and material refractive index of 1.59 before measuring the sample were passed through a 0.2 μm polyvinylidene fluoride (PVDF) membrane and the sample was loaded into quartz microcuvette, and measurement was performed. Scanning electron microscopy offers the information regarding the shape, size, and surface of the nanoparticles. Electron microscopy images a sample by scanning it with a high-energy beam of electrons. First the sample was sonicated for 15 minutes, then a drop of sample was dried on the glass slide, and this thin film was coated by carbon coated copper grid and observed under ZEISS EVO HD SEM. *Photoluminescence spectra* were recorded in Shimadzu (Japan) spectrofluorometer using 90° illumination and performed to find out the excitation and emission maxima for the silver nanoparticles. The excitation and emission slit widths were kept at 10 and 10 nm, respectively. The entire scanning was done at the speed of 600 nm/min.

2.4. Antimicrobial Property. To study the antibacterial effect of synthesized AgNPs from microalgae, agar well diffusion method was used against *E. coli*, *Klebsiella pneumoniae*, and *Aeromonas hydrophila*. 100 μL of bacteria was spread uniformly on MHA plate and 5 mm diameter wells were made on the medium. Into each well, 25, 50, 75, and 100 μL concentrations of AgNPs were added and the plates were incubated at 37°C for 24 hours and zone of inhibition was measured. Each experiment was performed in triplicate.

3. Result and Discussion

3.1. Scenedesmus abundans Mediated Bioreduction of Silver Ions. During bioreduction of AgNPs from silver ions there is a colour change which was monitored by using spectroscopic techniques. *In vitro* synthesis of AgNPs by *S. abundans*, it was observed that there is a colour change from colourless to reddish yellow due to the excitation of plasmon vibrations with AgNPs and the absorbance maximum was observed at 420 nm (Figure 1). The mechanism behind the synthesis of AgNPs was not known before but it was hypothesized later that the enzymes NADH-dependent nitrate reductase were used for the reduction of silver ions. The UV-Vis absorption spectra of AgNPs of *S. abundans* were shown in Figure 1 after 48 hours of the bioreduction.

3.2. Dynamic Light Scattering. The size measured in DLS technique is the hydrodynamic diameter of the theoretical area that diffuses with the similar speed as the measured nanoparticles. This size is not only connected with the

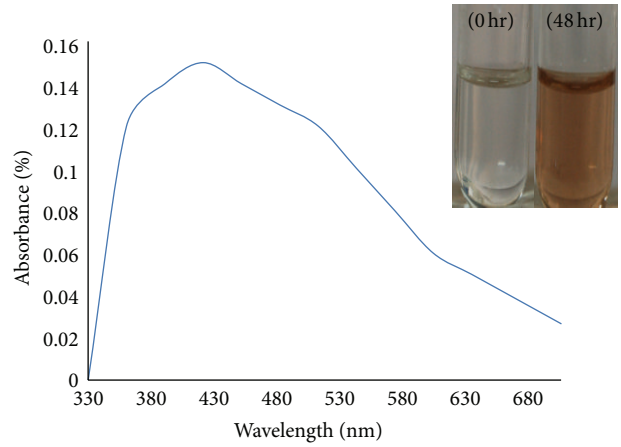

Figure 1: UV-Visible spectra of cell free extract after bioreduction.

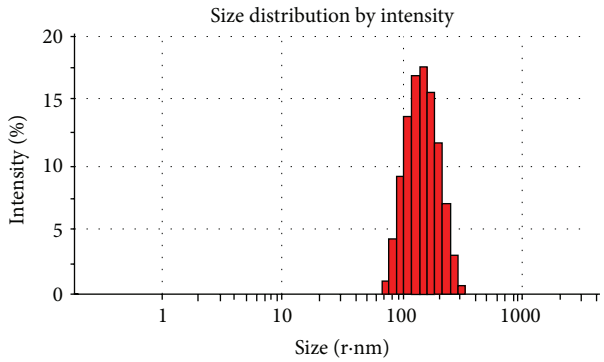

Figure 2: DLS spectra of the size distribution profile of the synthesized AgNPs.

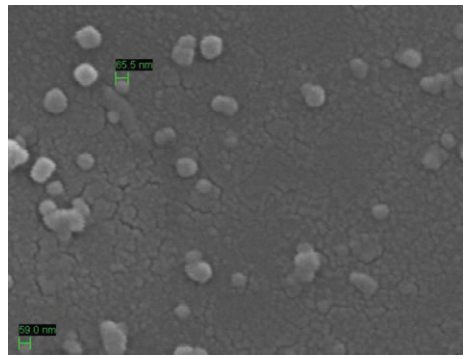

Figure 3: SEM image of synthesized AgNPs from *S. abundans*.

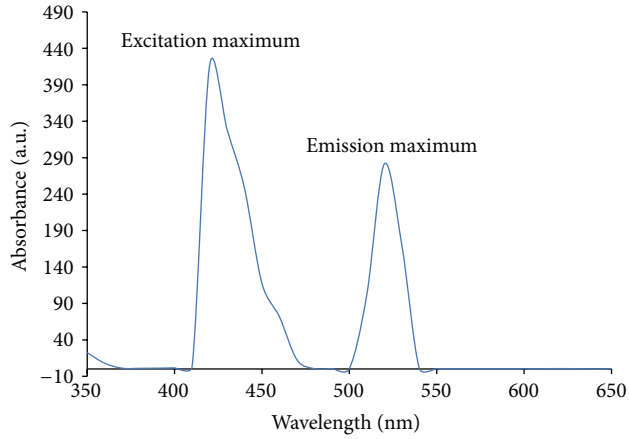

Figure 4: Photoluminescence of AgNPs synthesized from *S. abundans*.

metallic core of the nanoparticles but it is also influenced with all substances adsorbed on the surface of the nanoparticles (e.g., stabilizers) and the thickness of the electrical double layer (solvation shell), moving along with the particle. The thickness of the electrical double layer and its influence on the measured size of nanoparticles depend on the substances present in the colloid and on the surface of nanoparticles. As a result, the size measured in DLS technique is bigger in comparison with macroscopic techniques done in order to analyse the size distribution of synthesized nanoparticles with respect to the intensity. It was observed that on *in vitro* synthesis of nanoparticles the mean average size of the nanoparticles was found to be around 150 nm as given in Figure 2. The polydispersity index (PDI) of AgNPs was observed to be 0.212 which points out that these particles are polydispersed. Further analysis was done in order to confirm the size and presence of silver nanoparticles.

3.3. Scanning Electron Microscopy. SEM was carried out to analyze the synthesized nanoparticles for the morphology and their size. The SEM micrograph of *in vitro* bioreduction of silver ions confirms the size of the nanoparticles within the average range of 59–66 nm. The particles are well dispersed and showing no agglomeration as shown in Figure 3.

3.4. Photoluminescence. The data were analyzed using the WINFLR software. The photoluminescence from the roughened surface of noble metals could be viewed as an excitation of electrons from occupied d bands into state above the Fermi level; this mechanism is responsible for the nanocluster photoluminescence. This means that the growth of the clusters and the surface has changed the efficiency of the coupling of the excitation radiation to the surface plasmon. It is also found that there is no photoluminescence for large metal particles, because of them rapid radiation less processes compete effectively with radiative processes. Thus the smaller AgNPs clusters coexisting with the larger AgNPs are mainly responsible for the photoluminescence phenomena [26, 27]. Through analysis it was found that the photoluminescence spectra of synthesized AgNPs show that the excitation peak was found at 420 nm, while the emission peak was observed at 520 nm (Figure 4). The excitation peak at 420 nm is very well correlated with the absorption maxima recorded with UV-visible spectrophotometer.

3.5. Antibacterial Activity. Biosynthesized AgNPs were analysed for antibacterial activity against human pathogenic bacteria such as *E. coli*, *Klebsiella pneumonia*, and *Aeromonas hydrophila*. These tests were performed on MHA plates by

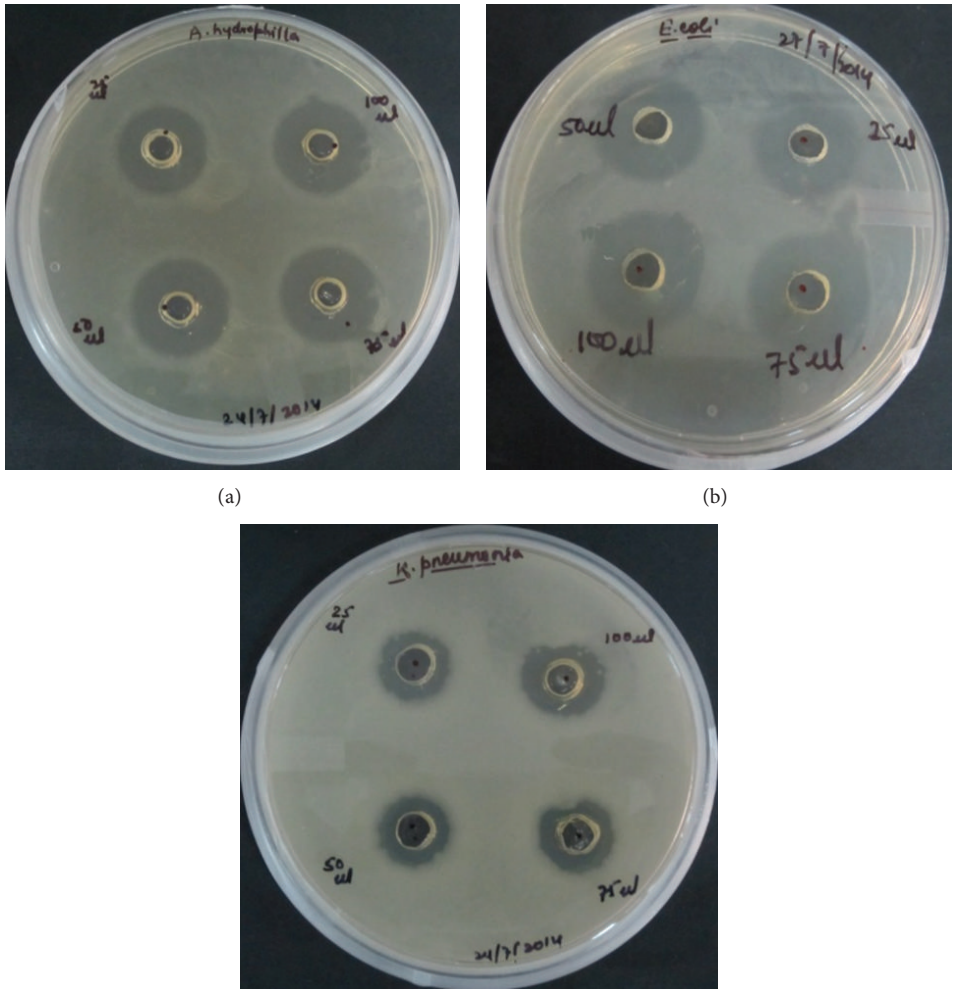

(a) (b)

(c)

Figure 5: Antibacterial effects varying the concentrations of AgNPs from 25 μL to 100 μL against (a) *Aeromonas hydrophila*, (b) *E. coli*, and (c) *Klebsiella pneumonia*.

well-diffusion method [28]. Growth of bacteria was inhibited by AgNPs and forms an inhibitory zone in Figures 5 and 6.

The highest zone of inhibition was observed for *E. coli* even at lower concentration. The mechanism of inhibition is still unknown. But the possible hypothesis for the mechanism related to the inhibition may be due to ionic binding of the AgNPs on the surface of the bacteria causing increase in the proton motive force; other hypothesis states that the nanoparticles enter into the cell and bind to the enzymes containing thiol groups [29, 30]. The molecular basis for the biosynthesis of these silver crystals, as the organic matrix contains the properties of silver binding which provides amino acid moieties which serve as the nucleation sites [31, 32]. The nanoparticles produced through *in vitro* synthesis that is by cell free extract gives zone of inhibition. The bacterial growth inhibition may be dependent upon the concentration of the nanoparticles present in the medium.

During the study *S. abundans* was utilized for the synthesis of AgNps upon addition of silver ions into the cell free extract. The colour of the samples changed from colourless to yellowish brown and observed UV-visible spectrum 420 nm due to reduction of the silver nitrate in aqueous solution

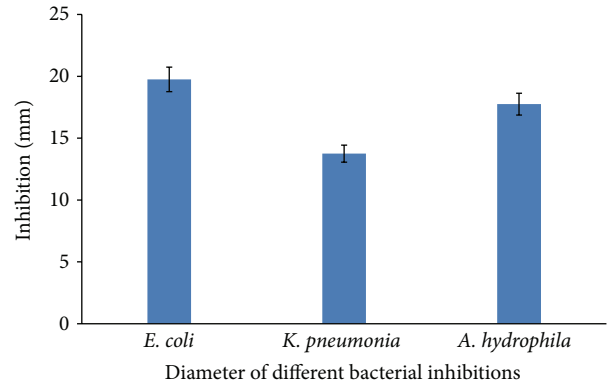

Figure 6: Antibacterial activity against synthesized AgNPs from *S. abundans*.

due to excitation of surface plasmon vibrations in silver nanoparticles. The plasmon bands were observed as broad, due to the size distribution of the particles [33, 34]. The size and structure of nanoparticles were further characterized using DLS and SEM analysis. The surface deposited AgNps are clearly seen at high magnification in the micrograph. Photoluminescence spectra of silver nanoparticles show that the excitation peak was at 420 nm, while the emission peak was observed at 520 nm. The rapid biological synthesis of silver nanoparticles by *S. abundans* provides a simple and proficient route for the synthesis of nanoparticles with optical properties directed by particle size. AgNPs have been verified to exhibit antimicrobial properties against bacteria with close attachment of the nanoparticles with the microbial cell and the action being size dependent [35–37].

4. Conclusion and Future Prospects

Biological synthesis of the AgNPs is rapid, cost effective, ecofriendly, and simple method of synthesis. There is lots of work done for green synthesis of nanoparticles from both prokaryotic as well as eukaryotic organisms [38]. During the whole work it has been concluded that the synthesized AgNPs through *in vitro* bioreduction system from unicellular microalga *S. abundans* produced significant amount of nanoparticles when it is exposed to 1 mM silver nitrate solution. The SEM analysis revealed that size of the nanoparticles ranges from 59 to 66 nm, and the synthesized nanoparticles were well dispersed. These nanoparticles show a broad spectrum of antimicrobial activity against both Gram positive and Gram negative bacteria [39, 40]. There is an everlasting need to increase the development of green synthesis of nanoparticles which should be environmentally acceptable solvent system, ecofriendly reducing and capping agents, high yield, low cost, and nontoxic [41].

Future prospects of this research is to scale up the biosynthesis production of AgNPs using these algae and also with the wide spectrum of microbial population. Further investigations would involve exploring the potency of microalgae to synthesize other metallic nanoparticles that can be used in pharmaceutical, food, cosmetics industry, and therapeutically in biomedical applications.

Conflict of Interests

The authors declare that there is no conflict of interests regarding the publication of this paper.

Acknowledgments

The authors are thankful to Dr. VK Jain, Advisor, AIARS (M&D), Amity University for SEM and Dr. Ravi Mani Tripathi, Assistant Professor, Amity University, India, for critically reading the paper and analyzing the data.

References

[1] P. Mukherjee, A. Ahmad, D. Mandal et al., "Fungus-mediated synthesis of silver nanoparticles and their immobilization in the mycelial matrix: a novel biological approach to nanoparticle synthesis," *Nano Letters*, vol. 1, no. 10, pp. 515–519, 2001.

[2] A. Kajbafvala, J. P. Samberg, H. Ghorbani, E. Kajbafvala, and S. K. Sadrnezhaad, "Effects of initial precursor and microwave irradiation on step-by-step synthesis of zinc oxide nanoarchitectures," *Materials Letters*, vol. 67, no. 1, pp. 342–345, 2012.

[3] A. Kajbafvala, M. R. Shayegh, M. Mazloumi et al., "Nanostructure sword-like ZnO wires: rapid synthesis and characterization through a microwave-assisted route," *Journal of Alloys and Compounds*, vol. 469, no. 1-2, pp. 293–297, 2009.

[4] S. Sinha, I. Pan, P. Chanda, and S. K. Sen, "Nanoparticles fabrication using ambient biological resources," *Jounal of Applied Biological Science*, vol. 19, pp. 1113–1130, 2009.

[5] B. Wiley, Y. Sun, and Y. Xia, "Synthesis of silver nanostructures with controlled shapes and properties," *Chemical Research*, vol. 40, no. 10, pp. 1067–1076, 2007.

[6] A. Kajbafvala, H. Ghorbani, A. Paravar, J. P. Samberg, E. Kajbafvala, and S. K. Sadrnezhaad, "Effects of morphology on photocatalytic performance of Zinc oxide nanostructures synthesized by rapid microwave irradiation methods," *Superlattices and Microstructures*, vol. 51, no. 4, pp. 512–522, 2012.

[7] A. Kajbafvala, S. Zanganeh, E. Kajbafvala, H. R. Zargar, M. R. Bayati, and S. K. Sadrnezhaad, "Microwave-assisted synthesis of narcis-like zinc oxide nanostructures," *Journal of Alloys and Compounds*, vol. 497, no. 1-2, pp. 325–329, 2010.

[8] H. J. Klasen, "A historical review of the use of silver in the treatment of burns. II. Renewed interest for silver," *Burns*, vol. 26, no. 2, pp. 131–138, 2000.

[9] Y. F. Huang, H. T. Chang, and W. Tan, "Cancer cell targeting using multiple aptamers conjugated on nanorods," *Analytical Chemistry*, vol. 80, no. 3, pp. 567–572, 2008.

[10] N. Chakraborty, R. Pal, A. Ramaswami, D. Nayak, and S. Lahiri, "Diatom: a potential bio-accumulator of gold," *Journal of Radioanalytical and Nuclear Chemistry*, vol. 270, no. 3, pp. 645–649, 2006.

[11] D. Parial, H. K. Patra, A. K. R. Dasgupta, and R. Pal, "Screening of different algae for green synthesis of gold nanoparticles," *European Journal of Phycology*, vol. 47, no. 1, pp. 22–29, 2012.

[12] C. Nethradevi, P. Sivakumar, and S. Renganathan, "Green synthesis of silver nanoparticles using datura metel flower extract and evaluation of their antimicrobial activity," *International Journal of Nanomaterials and Biostructures*, vol. 2, pp. 16–21, 2012.

[13] R. R. Nayak, N. Pradhan, D. Behera et al., "Green synthesis of silver nanoparticle by *Penicillium purpurogenum* NPMF: the process and optimization," *Journal of Nanoparticle Research*, vol. 13, no. 8, pp. 3129–3137, 2011.

[14] D. Vijayaraj, J. Anarkali, K. Rajathi, and S. Sridhar, "Green synthesis and characterization of silver nanoparticles from the leaf extract of aristolochia bracteata and its antimicrobial efficacy," *International Journal of Nanomaterials and Biostructures*, vol. 2, pp. 11–15, 2012.

[15] A. Saxena, R. M. Tripathi, F. Zafar, and P. Singh, "Green synthesis of silver nanoparticles using aqueous solution of Ficus benghalensis leaf extract and characterization of their antibacterial activity," *Materials Letters*, vol. 67, no. 1, pp. 91–94, 2012.

[16] N. Pradhan, R. R. Nayak, A. K. Pradhan, L. B. Sukla, and B. K. Mishra, "In situ synthesis of entrapped silver nanoparticles by a fungus-*penicillium purpurogenum*," *Nanoscience and Nanotechnology Letters*, vol. 3, no. 5, pp. 659–665, 2011.

[17] R. G. Haverkamp and A. T. Marshall, "The mechanism of metal nanoparticle formation in plants: limits on accumulation," *Journal of Nanoparticle Research*, vol. 11, no. 6, pp. 1453–1463, 2009.

[18] V. K. Sharma, R. A. Yngard, and Y. Lin, "Silver nanoparticles: green synthesis and their antimicrobial activities," *Advances in Colloid and Interface Science*, vol. 145, no. 1-2, pp. 83–96, 2009.

[19] N. Savithramma, M. Linga Rao, K. Rukmini, and P. Suvarnalatha Devi, "Antimicrobial activity of silver nanoparticles synthesized by using medicinal plants," *International Journal of ChemTech Research*, vol. 3, no. 3, pp. 1394–1402, 2011.

[20] R. Prasad, "Synthesis of silver nanoparticles in photosynthetic plants," *Journal of Nanoparticles*, vol. 2014, Article ID 963961, 2014.

[21] K. N. Thakkar, S. S. Mhatre, and R. Y. Parikh, "Biological synthesis of metallic nanoparticles," *Nanomedicine*, vol. 6, no. 2, pp. 257–262, 2010.

[22] K. Vijayaraghavan and S. P. K. Nalini, "Biotemplates in the green synthesis of silver nanoparticles," *Biotechnology Journal*, vol. 5, no. 10, pp. 1098–1110, 2010.

[23] A. L. Ahmad, N. H. M. Yasin, C. J. C. Derek, and J. K. Lim, "Microalgae as a sustainable energy source for biodiesel production: a review," *Renewable and Sustainable Energy Reviews*, vol. 15, no. 1, pp. 584–593, 2011.

[24] S. Rajeshkumar, C. Malarkodi, K. Paulkumar, M. Vanaja, G. Gnanajobitha, and G. Annadurai, "Algae mediated green fabrication of silver nanoparticles and examination of its antifungal activity against clinical pathogens," *International Journal of Metals*, vol. 2014, Article ID 692643, 8 pages, 2014.

[25] H. C. Bold and M. J. Wynne, *Introduction to the Algae: Structure and Reproduction*, vol. 16, Prentice-Hall, Englewood Cliffs, NJ, USA, 2nd edition, 1985.

[26] P. He, X.-H. Shen, and H.-C. Gao, "Photoluminescence phenomenon during the formation of silver nanoparticles," *Acta Physico-Chimica Sinica*, vol. 20, no. 10, pp. 1200–1203, 2004.

[27] N. Vigneshwaran, A. A. Kathe, P. V. Varadarajan, R. P. Nachane, and R. H. Balasubramanya, "Biomimetics of silver nanoparticles by white rot fungus, *Phaenerochaete chrysosporium*," *Colloids and Surfaces B: Biointerfaces*, vol. 53, no. 1, pp. 55–59, 2006.

[28] R. Prasad, V. S. Swamy, K. S. Prasad, and A. Varma, "Biogenic synthesis of silver nanoparticles from the leaf extract of *Syzygium cumini* (L.) and its antibacterial activity," *International Journal of Pharma and Bio Sciences*, vol. 3, no. 4, pp. 745–752, 2012.

[29] N. Prabhu, D. T. Raj, K. Yamuna Gowri, S. Ayisha Siddiqua, and D. Joseph Puspha Innocent, "Synthesis of silver phyto nanoparticles and their antibacterial efficacy," *Digest Journal of Nanomaterials and Biostructures*, vol. 5, no. 1, pp. 185–189, 2010.

[30] R. Prasad, V. Kumar, and K. S. Prasad, "Nanotechnology in sustainable agriculture: present concerns and future aspects," *African Journal of Biotechnology*, vol. 13, pp. 705–713, 2014.

[31] V. S. Swamy and R. Prasad, "Green synthesis of silver nanoparticles from the leaf extract of Santalum album and its antimicrobial activity," *Journal of Optoelectronic and Biomedical Materials*, vol. 4, no. 3, pp. 53–59, 2012.

[32] A. Saxena, R. M. Tripathi, and R. P. Singh, "Biological synthesis of silver nanoparticles by using onion *Allium cepa* extract and their antibacterial activity," *Digest Journal of Nanomaterials and Biostructures*, vol. 5, no. 2, pp. 427–432, 2010.

[33] G. C. Schatz and R. P. van-Duyne, "Electromagnetic enhancement of surface-enhanced raman spectroscopy," in *Handbook of Vibrational Spectroscopy*, J. M. Chalmers and P. R. Griffiths, Eds., Wiley, New York, NY, USA, 2002.

[34] T. A. Davis, B. Volesky, and A. Mucci, "A review of the biochemistry of heavy metal biosorption by brown algae," *Water Research*, vol. 37, no. 18, pp. 4311–4330, 2003.

[35] A. B. G. Lansdown, "Silver. I: its antibacterial properties and mechanism of action," *Journal of Wound Care*, vol. 11, no. 4, pp. 125–130, 2002.

[36] I. Sondi and B. Salopek-Sondi, "Silver nanoparticles as antimicrobial agent: a case study on *E. coli* as a model for Gram-negative bacteria," *Journal of Colloid and Interface Science*, vol. 275, no. 1, pp. 177–182, 2004.

[37] R. M. Tripathi, D. Rana, A. Shrivastava, R. P. Singh, and B. R. Shrivastav, "Biogenic synthesis of silver nanoparticles using Saraca indica leaf extract and evaluation of their antibacterial activity," *Nano Biomedicine and Engineering*, vol. 5, no. 1, pp. 50–56, 2013.

[38] J. R. Morones, J. L. Elechiguerra, A. Camacho et al., "The bactericidal effect of silver nanoparticles," *Nanotechnology*, vol. 16, no. 10, pp. 2346–2353, 2005.

[39] R. Prasad and V. S. Swamy, "Antibacterial activity of silver nanoparticles synthesized by bark extract of *Syzygium cumini*," *Journal of Nanoparticles*, vol. 2013, Article ID 431218, 6 pages, 2013.

[40] S. S. Birla, S. C. Gaikwad, A. K. Gade, and M. K. Rai, "Rapid synthesis of silver nanoparticles from *Fusarium oxysporum* by optimizing physicocultural conditions," *The Scientific World Journal*, vol. 2013, Article ID 796018, 12 pages, 2013.

[41] J. Xie, J. Y. Lee, D. I. C. Wang, and Y. P. Ting, "Silver nanoplates: from biological to biomimetic synthesis," *ACS Nano*, vol. 1, no. 5, pp. 429–439, 2007.

Hindawi Publishing Corporation
Journal of Nanoparticles
Volume 2014, Article ID 916429, 7 pages
http://dx.doi.org/10.1155/2014/916429

Research Article

Role of Surfactant in the Formation of Gold Nanoparticles in Aqueous Medium

Abhishek Das, Ridhima Chadha, Nandita Maiti, and Sudhir Kapoor

Radiation & Photochemistry Division, Bhabha Atomic Research Centre, Trombay, Mumbai 400 085, India

Correspondence should be addressed to Sudhir Kapoor; sudhirk@barc.gov.in

Received 25 July 2014; Accepted 28 August 2014; Published 10 September 2014

Academic Editor: Amir Kajbafvala

The stability of gold nanoparticles is a major issue which decides their impending usage in nanobiotechnological applications. Often biomimetically synthesized nanoparticles are deemed useless owing to their instability in aqueous medium. So, surfactants are used to stabilize the nanoparticles. But does the surfactant only stabilize by being adsorbed to the surface of the nanoparticles and not play significantly in moulding the size and shape of the nanoparticles? Keeping this idea in mind, gold nanoparticles (GNPs) synthesized by l-tryptophan (Trp) mediated reduction of chloroauric acid ($HAuCl_4$) were stabilized by anionic surfactant, sodium dodecyl sulphate (SDS), and its effect on the moulding of size and properties of the GNPs was studied. Interestingly, unlike most of the gold nanoparticles synthesis mechanism showing saturation growth mechanism, inclusion of SDS in the reaction mixture for GNPs synthesis resulted in a bimodal mechanism which was studied by UV-Vis spectroscopy. The mechanism was further substantiated with transmission electron microscopy. Zeta potential of GNPs solutions was measured to corroborate stability observations recorded visually.

1. Introduction

Gold nanoparticles are important to bionanotechnology, owing to their easy synthesis, inert nature, good biocompatibility, and unique optical properties [1]. The tuning of optical properties of gold nanoparticles can be achieved by controlling the size of the nanoparticles [2]. Factors controlling the size of the gold nanoparticles are, namely, surface charge and double layer thickness [3]. Surface charge is again controlled by two criteria, nature and charge of ions adsorbed on the particles and surfactants used to stabilize the particles [4, 5]. Surfactants are used in the synthesis of gold nanoparticles when the reducing agent is not able to stabilize the particles [6]. The standard reducing agents which stabilize the gold nanoparticles in absence of any surfactant are sodium borohydride [7] and sodium citrate [8]. But for in-vivo applications these nanoparticles are of little use since the oxidised products of the reducing agents themselves show cytotoxicity [9, 10]. Thus, biomimetic routes of synthesis of gold nanoparticles are often implemented wherein a biomolecule is used as a reducing agent [11].

In recent years, many biomimetic synthetic [12–14] routes have been proposed to make the synthesized GNPs viable for bioapplication. For example, a variety of amino compounds have been explored as reducing agents which includes amino acids [15, 16], primary amines [17], peptides [18–22], and polymers [23]. Amino acids being the building blocks of proteins, which are ubiquitous in organisms, have collected a lot of interest to serve as a reducing agent. In some cases, amino acids have been also used as a capping agent to stabilize GNPs [24] since amino acids show strong interaction with gold nanoparticles [25]. Jacob et al. have shown that replacement of BH_4^- ion by Trp at silver nanoparticles surface resulted in particle aggregation [26]. Recently a simple, facile single-step technique for synthesis of gold nanowires and nanochains has been demonstrated using amino acids like histidine and glutamic acid [27]. Wangoo et al. have demonstrated the successful synthesis and capping of GNPs by glutamic acid [28]. Glutathione stabilized gold nanoparticles were found as an alternative to polyethylene glycol (PEG) stabilized GNPs that increase the stealth properties in *in vivo* studies for application in therapeutics [29]. It was also demonstrated

that tyrosine plays an important role in reduction of Au^{3+} to Au^0 by a number of tyrosine containing peptides, but mostly limited to dipeptides and tripeptides [19]. Oligopeptides containing l-tryptophan at C-terminus are used by Si and Mandal to synthesize gold and silver nanoparticles at high pH [22]. Selvakannan et al. have reported the synthesis of lysine and tryptophan capped GNPs by spontaneous reduction of $HAuCl_4$ or reduction by $NaBH_4$ followed by capping with tryptophan [15, 30]. Iosin et al. have reported the synthesis of GNPs using tryptophan as reducing agent and have shown that with changing temperature the morphology of the GNPs synthesized changes from spherical to anisotropic shapes [31]. Tryptophan exists in our body as free tryptophan, dipeptides and in peptide chains [32]. Tryptophan is easily detectable by UV-Vis spectroscopy and fluorescence owing to the indole ring in its structure. Tryptophan is known to reduce gold nanoparticles [31], but it is inadequate in stabilizing the nanoparticles. Thus, in this study, the use of stabilizing agent becomes imperative. In this work, chloroauric acid ($HAuCl_4$) is reduced by l-tryptophan (Trp) in presence of a stabilizing agent, sodium dodecyl sulphate (SDS).

2. Materials and Methods

2.1. Chemicals. Chloroauric acid (Sigma-Aldrich), l-tryptophan (Fluka AG), and sodium dodecyl sulphate (Sigma, USA) were used as received. All experiments were performed in Millipore purified water.

2.2. Synthesis and Characterization of Au Nanoparticles. Gold nanoparticles are produced in absence of any stabilizer by the reaction of chloroauric acid ($HAuCl_4$) with l-tryptophan (Trp) mixed in different ratio. The UV-Vis spectra of the produced nanoparticles were then recorded in JASCO V-650 spectrophotometer. The same experiment was performed in presence of 1 mM sodium dodecyl sulphate (SDS). The stable gold sols were then characterised by scanning electron microscopy (SERON INC, South Korea, AIS 2100), energy dispersive X-ray spectroscopy (Oxford Instruments, UK, INCA E350), transmission electron microscopy (Zeiss, Libra 12), and zeta potential measurements (Zetasizer, Malvern, Nano-Z).

3. Results and Discussion

UV-Vis spectroscopy is an important tool for analysing formation of gold nanoparticles as gold nanoparticles have high molar extinction coefficient. The UV-visible absorption spectra of the fairly dilute dispersion of colloidal particles can be calculated from the "Mie theory" [5] and this technique serves as a powerful tool to characterize metal nanoparticles. The absorbance A of a colloidal solution containing N particles per unit volume is given by

$$A = \left(\frac{N\sigma_{\text{abs}}L}{\ln 10}\right), \quad (1)$$

where σ_{abs} (given by $\sigma_{\text{abs}} = \sigma_{\text{ext}} - \sigma_{\text{scattering}}$) and L are absorption cross-section and optical path length, respectively. So, it can be clearly understood that the magnitude of absorbance for resonant peak indicates the concentration of nanoparticles.

Again, the particle size determines the peak position. At nanoregime, the variation in surface to volume ratio with increasing size shows a gradually decreasing trend. As a result, on increasing size the fraction of surface free electrons decreases. So less energy is required to polarize them. Thus, red shift (shift to longer wavelength) is observed on increasing size. Moreover, plasmonic dipolar coupling leads to red shift of the plasmon band on agglomeration.

GNPs were synthesized by the reaction of $HAuCl_4$ and Trp in absence of any stabilizing agent. UV-Vis spectrums of the GNP solutions were recorded, as shown in Figure 1. When 0.5 mM $HAuCl_4$ reacted with 0.5 mM Trp (Figure 1(a)) red coloured GNPs which showed maximum absorbance at 577 nm (λ_{max}) were formed. When 0.5 mM $HAuCl_4$ reacted with 1 mM Trp (Figure 1(b)), red coloured GNPs were formed with λ_{max} at 569 nm. GNPs formed by the reaction of 1 mM $HAuCl_4$ and 0.5 mM Trp (Figure 1(c)) showed λ_{max} at 530 nm. GNPs formed by the reaction of 1 mM $HAuCl_4$ and 1 mM Trp showed absorption maxima (λ_{max}) at 570 nm, as shown in Figure 1(d). All the above GNP solutions precipitated within 1 hour of formation of gold nanoparticles. In all the above GNPs solutions, λ_{max} ranges from 530 nm to 577 nm.

Another set of similar reactions where the ratios of $HAuCl_4$ and Trp were the same as above, was carried out in presence of 1 mM SDS as stabilizer. The UV-Vis spectrums of the gold nanoparticles solutions were recorded as shown in Figure 2(a–d). λ_{max} ranges from 533 nm to 543 nm. The narrow range of λ_{max} suggests that surfactant is controlling the shape and size of the GNPs formed. In reaction set where the ratio of $HAuCl_4$ to Trp was 2 : 1, GNPs were found to precipitate (Figure 2(c)). This can be attributed to the presence of excess of $HAuCl_4$ as compared to Trp, which reduced the double layer thickness, thereby facilitating faster agglomeration. In this set of reactions performed in presence of SDS, it was also observed that the surface plasmon peaks were quite sharper than that of the solution sets prepared in absence of SDS. This indicates that SDS is able to stabilize gold sol quite efficiently.

Transmission electron microscope images of GNPs formed in the above four reaction sets prepared in presence of 1 mM SDS were recorded as shown in Figures 3(a)–3(d). GNPs shown in Figures 3(a), 3(b), and 3(d) are approximately 20 nm in size. GNPs shown in Figure 3(c) show a size range of about 50–100 nm which indicates high agglomeration. Scanning electron microscope (SEM) image of GNPs synthesized by the reaction of 1 mM $HAuCl_4$ and 1 mM Trp in presence of 1 mM SDS and drop casted on silica substrate revealed that the nanoparticles are well dispersed, as shown in Figure S1(a) (see the Supplementary Material available online at http://dx.doi.org/10.1155/2014/916429). Moreover, energy dispersive X-ray spectroscopy (EDX) of the above GNPs confirms the presence of gold in the sol as shown in Figure S1(b).

Zeta potential measurements were carried out in an electrophoretic cell to determine the long term stability and

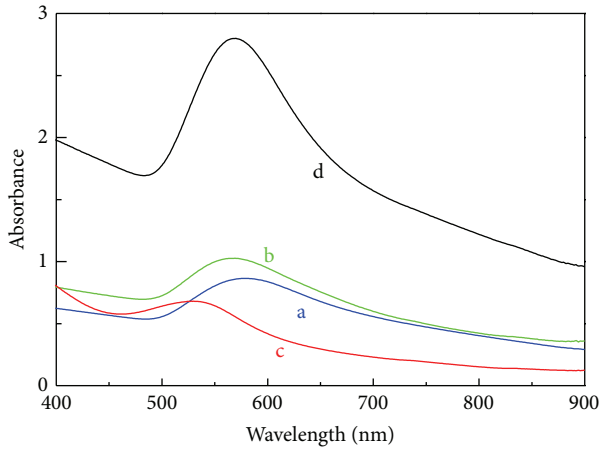

Figure 1: UV-Vis spectrum of gold nanoparticles in absence of any stabilizer in aqueous medium formed by the reaction of 0.5 mM $HAuCl_4$ with (a) 0.5 mM l-Trp and (b) 1 mM Trp and that of 1 mM $HAuCl_4$ with (c) 0.5 mM l-Trp and (d) 1 mM Trp.

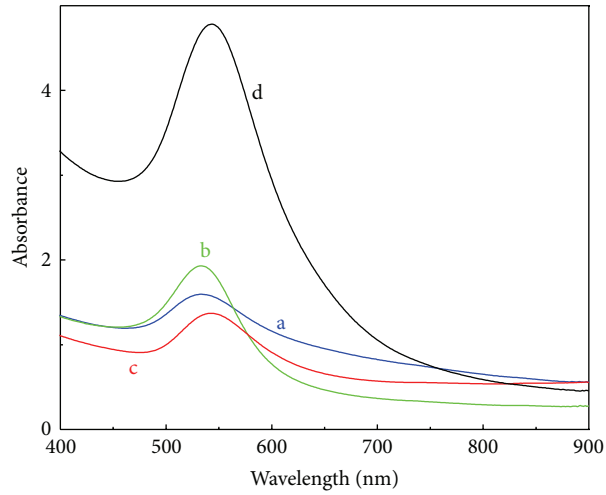

Figure 2: UV-Vis spectrum of gold nanoparticles in 1 mM SDS solution formed by the reaction of 0.5 mM $HAuCl_4$ with (a) 0.5 mM Trp and (b) 1 mM Trp and that of 1 mM $HAuCl_4$ with (c) 0.5 mM Trp and (d) 1 mM Trp.

to provide a basis to the earlier mentioned visual observations about the stability of different gold nanoparticles solutions. Zeta potential values recorded after formation of GNPs shown in Figures 3(a), 3(b), 3(c), and 3(d) prepared in SDS solution are −41.4 mV, −47.7 mV, −28.9 mV, and −37.3 mV, respectively. This clearly corroborates earlier observation that out of these four solutions, GNPs shown in Figure 3(c) are not stable in solution. Moreover the above negative zeta potential values also show that the colloids have a net negative charge on them. The reason behind the negative charge may be due to adsorption of negatively charged SDS molecules on the surface.

Studying of the kinetics involves plotting of UV-Vis λ_{max} absorption value of GNPs with time from the beginning of the reaction. The reaction of 5×10^{-4} M Trp with 1×10^{-3} M $HAuCl_4$ shows saturation growth type of kinetics. An absorbance *versus* time spectra of the reaction, recorded at 530 nm (λ_{max} for the GNPs synthesized), is shown in Figure 4. The above observation shows that Au^{3+} and Trp show a simple reaction mechanism where GNPs of only one size distribution are formed. It has also been observed that the trace is concentration dependent.

All the solution sets of $HAuCl_4$ and Trp in presence of SDS were subjected to fixed wavelength UV-Vis absorption at their respective λ_{max} to study their growth with time. GNPs formed by the reaction of 0.5 mM $HAuCl_4$ and 0.5 mM Trp in 1 mM SDS had very low final absorbance as shown in Figure 2(a), which made them unsuitable for study of mechanism of growth of nanoparticles. The same case was with the GNPs formed by the reaction of 0.5 mM $HAuCl_4$ with 1 mM Trp in presence of 1 mM SDS as shown in Figure 2(b). Again GNPs formed by the reaction of 1 mM $HAuCl_4$ with 0.5 mM Trp in presence of 1 mM SDS were rendered unsuitable since the particles precipitated within the time of study. Only the GNP synthesis by the reaction of 1 mM $HAuCl_4$ and 1 mM Trp in presence of 1 mM SDS was the most suitable candidate for fixed wavelength UV-Vis absorption study. UV-Vis absorption with time of the above solution was recorded at 543 nm as shown in Figure 5.

The absorbance versus time plot (Figure 5) is divided into five regions, namely, A, B, C, D, and E. At the end of region A, GNPs first start appearing 509 nm. In region B, the peak remains in the range from 509 to 512 nm. A drastic peak shift from 512 nm to 543 nm is observed in region C within a short span of 22 minutes. In region D, the peak remains almost at the same position (543 to 545 nm). In region E, a slight shift of peak is seen from 543 nm to 541 nm. Then onwards the peak remains at 541 nm. This phenomenon is also observed in case reaction of 0.5 mM $HAuCl_4$ with 0.5 mM Trp as well as 1 mM Trp, but because of low final absorbance and taking the sensitivity of the UV-Vis measurement into consideration, these reactions were not studied to determine the mechanism of reaction. The UV-Vis spectrum of the above solution at different times is also recorded as shown in Figure 6.

In region A (Figure 5), it seems that smaller GNPs are forming by the reduction of $HAuCl_4$ by Trp. In region B (Figure 5), the reduction process seems to have achieved saturation. In region C (Figure 5), the drastic shift can be attributed to bimolecular agglomeration and autocatalytic agglomeration as there is an observable shift in λ_{max} value. In region D (Figure 5), the almost linear and saturation type of growth at a fixed λ_{max} can be attributed to predominance of autocatalytic agglomeration mechanism. In region E (Figure 5), the small shift in λ_{max} may be attributed to adsorption of surfactant molecules on the GNPs. In the above reaction, bimodal size distribution is observed during the course of the reaction. This reaction can be said to follow a bimodal mechanism.

Finney et al. [33] and Sabir et al. [34] have observed similar mechanisms to occur during synthesis of GNPs by different routes. A proposed scheme of bimodal mechanism is shown in Scheme 1.

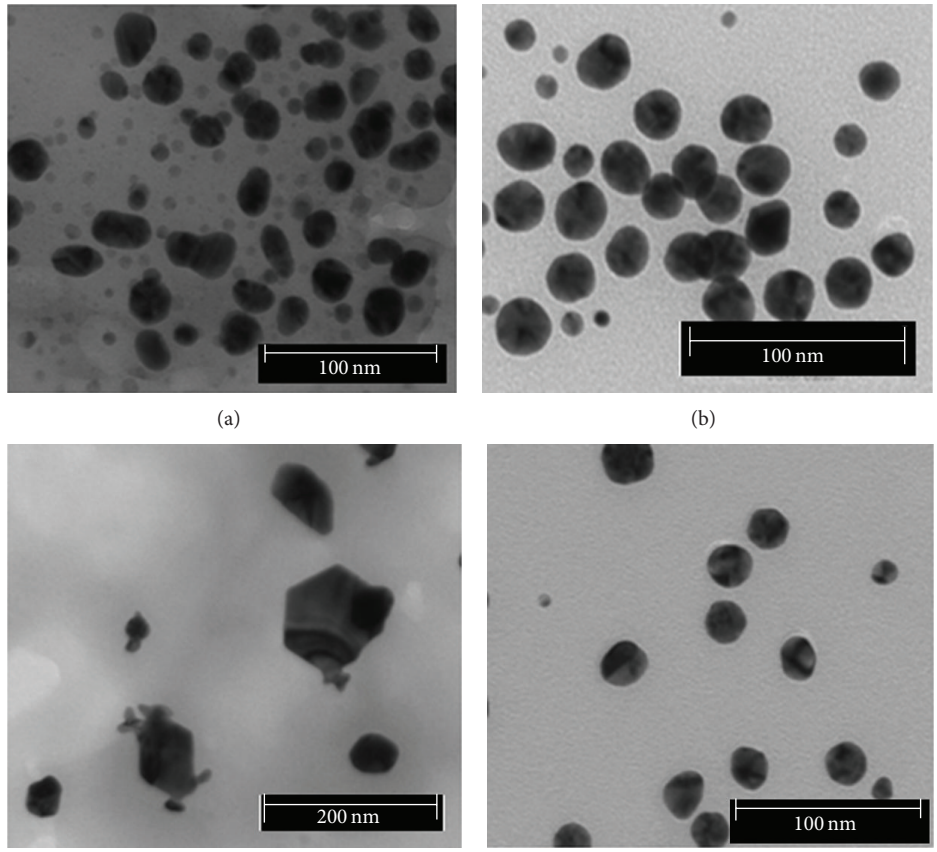

Figure 3: Transmission electron microscope image of gold nanoparticles in 1 mM SDS solution formed by the reaction of 0.5 mM $HAuCl_4$ with (a) 0.5 mM Trp and (b) 1 mM Trp and that of 1 mM $HAuCl_4$ with (c) 0.5 mM Trp and (d) 1 mM Trp.

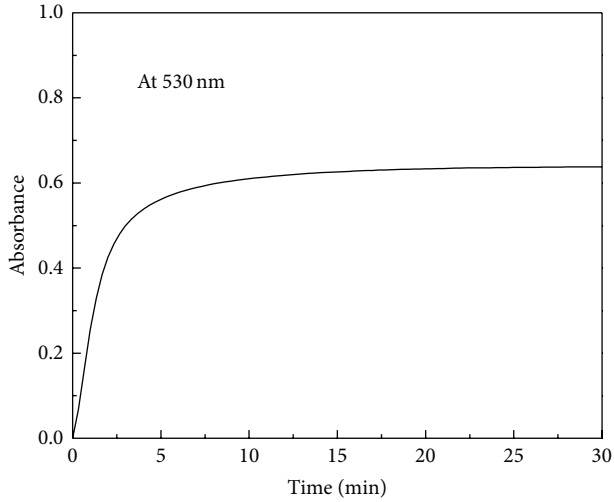

Figure 4: UV-Vis spectrum recorded at 530 nm with time (in minutes) for the reaction of 0.5 mM Trp with 1 mM $HAuCl_4$ in absence of any stabilizer.

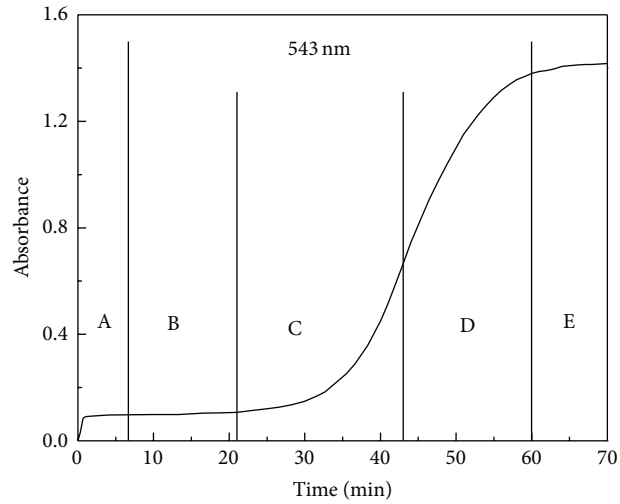

Figure 5: UV-Vis spectrum recorded at 543 nm with time (in minutes) for the reaction of 1 mM Trp with 1 mM $HAuCl_4$ in 1 mM SDS solution.

First two steps, namely, nucleation and autocatalytic growth, are difficult to characterize by optical method as magnitude of σ_{abs} is very low for small GNPs (here B is assumed to be small GNPs). Here it is assumed that, before the commencement of bimolecular agglomeration and autocatalytic agglomeration step, the first two elementary

$$n\mathrm{Au}^{3+} + \mathrm{A} \xrightarrow[\text{Nucleation}]{k_1} \mathrm{Au}_n^0 + \mathrm{B}\ (\text{smaller GNPs})$$

$$\mathrm{A} + \mathrm{B} \xrightarrow[\text{Autocatalytic growth}]{k_2} 2\mathrm{B}$$

$$\mathrm{B} + \mathrm{B} \xrightarrow[\text{Bimolecular agglomeration}]{k_3} \mathrm{C}\ (\text{larger GNPs})$$

$$\mathrm{B} + \mathrm{C} \xrightarrow[\text{Autocatalytic agglomeration}]{k_4} 1.5\mathrm{C}$$

Scheme 1: Schematic representation of bimodal mechanism of formation of gold nanoparticles.

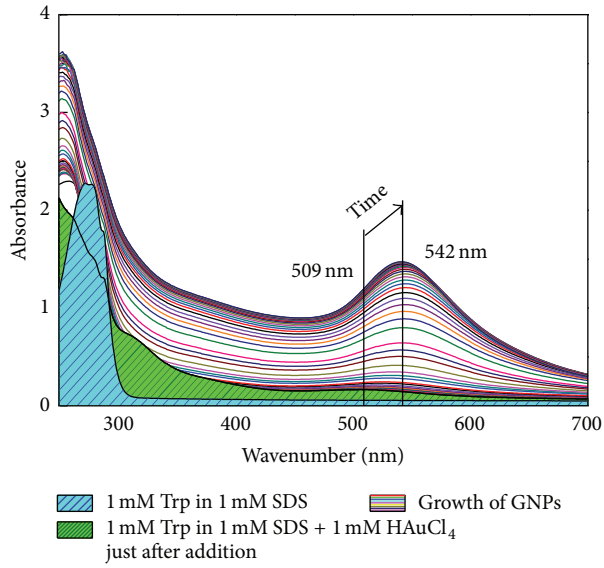

Figure 6: UV-Vis spectrums recorded during the reaction of 1 mM Trp with 1 mM $HAuCl_4$ in 1 mM SDS solution.

reactions involving reduction of Au^{3+} ions, are complete. But as the size of the GNPs falls within the range of 5–20 nm, optical measurements become quite reliable.

It can be seen that the variation in wavelength in region B is very less. It reflects that though bimolecular agglomeration has started but the rate is not that high. The rate law for the last two steps, namely, bimolecular agglomeration and autocatalytic agglomeration, may be given as follows:

$$-\frac{d[\mathrm{B}]}{dt} = 2k_3[\mathrm{B}]^2 + k_4[\mathrm{B}][\mathrm{C}]$$

$$\because 2[\mathrm{C}] = [\mathrm{B}]_0 - [\mathrm{B}], \quad \text{we get} \tag{2}$$

$$\frac{d[\mathrm{C}]}{dt} = k_3[\mathrm{B}]^2 + \frac{1}{2}k_4[\mathrm{B}][\mathrm{C}].$$

In region B, as the number density of larger GNPs, that is [C], is very low, (2) reduces to $d[\mathrm{C}]/dt = k_3[\mathrm{B}]^2$, and solving it we get

$$[\mathrm{C}] = \frac{[\mathrm{B}]_0}{2}\left\{1 - \frac{1}{2k_3[\mathrm{B}]_0 t + 1}\right\}. \tag{3}$$

Thus with increasing time, number density of C increases. Again as absorbance is directly proportional to the number density, absorbance also increases.

In region C, there is a drastic increase in the wavelength as well as absorbance. This indicates that the formation of C has increased and as a result the size distribution shifts toward the higher wavelength. Now the rate equation can be given by

$$\frac{d[\mathrm{C}]}{dt} = \frac{1}{2}k_4[\mathrm{B}][\mathrm{C}]. \tag{4}$$

Here the basic assumption is that formation of B has reached saturation.

In region D, trace resembles a saturation growth type of profile. In this region, the change in wavelength is very less. It may be said that, in this region, the predominant process occurring is autocatalytic agglomeration.

This bimodal mechanism of formation of GNPs is further confirmed by transmission electron microscopy by recording the image of the GNPs formed after 5 minutes of initiation of reaction, that is, in the plateau region shown in Figure 7. The TEM image shows that the particles are roughly 10 nm in size, whereas the particles formed after the completion of the reaction are about 20 nm in size

It is assumed that UV-Vis absorbance value is proportional to the concentration and approximate concentration of gold nanoparticles determined by taking the approximate size of gold nanoparticles as obtained from TEM image shown in Figures 3(d) and 7. With the above assumptions, the curve shown in Figure 5 is fitted with (3) and (4). It was found that the bimolecular aggregation step has initiated just after the onset of reduction step and the autocatalytic agglomeration has started at around 28 minutes from the onset of reaction as shown in Figure 8.

4. Conclusion

L-tryptophan reduced gold nanoparticles are stabilized in aqueous solution by SDS. Results revealed that SDS plays an important role in the formation mechanism of the gold nanoparticles. Moreover, the reaction kinetics of GNPs in this case is easily observable by a steady-state spectroscopic method such as UV-Vis spectroscopy unlike $NaBH_4$ where the reaction is too fast and citrate method where heating is required to initiate the reaction. The kinetic details of the formation processes of GNPs reveal the bimodal mechanism. The observation of formation of gold nanoparticles of two different sizes, spaced over a time gap of about 30 minutes during the process of synthesis, opens up the prospect of utilizing the same reaction to tune nanoparticles size. The GNPs prepared by this method are quite stable, which suggests that their usage in biological application can be safely extrapolated in future. This study guides our attention towards the potential usage of anionic surfactants in tuning the size of GNPs along with their stabilization.

Conflict of Interests

The authors declare that there is no conflict of interests regarding the publication of this paper.

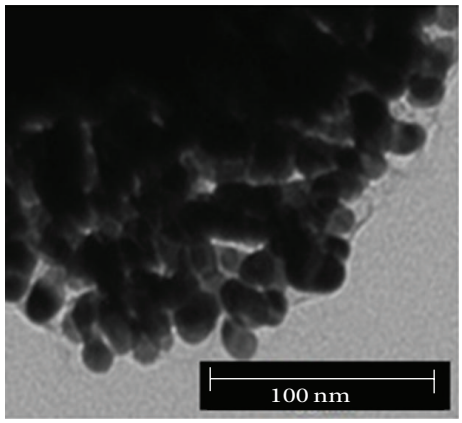

Figure 7: Transmission electron microscope image of GNPs formed after 5 minutes of initiation of reaction between 1 mM $HAuCl_4$ and 1 mM Trp in presence of 1 mM SDS.

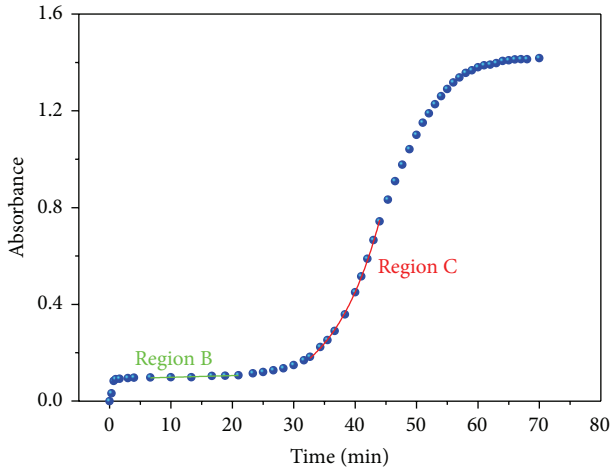

Figure 8: UV-Vis spectrum recorded at 543 nm with time (in minutes) for the reaction of 1 mM Trp with 1 mM $HAuCl_4$ in 1 mM SDS solution, showing fitted curve using (3) and (4) for the regions B and C as mentioned in Figure 5.

Acknowledgments

The authors are grateful to Dr. B. N. Jagatap, Director of Chemistry Group, and Dr. D. K. Palit, Head of Radiation & Photochemistry Division, for their encouragement during the course of this study.

References

[1] M.-C. Daniel and D. Astruc, "Gold nanoparticles: assembly, supramolecular chemistry, quantum-size-related properties, and applications toward biology, catalysis, and nanotechnology," *Chemical Reviews*, vol. 104, no. 1, pp. 293–346, 2004.

[2] E. S. Kooij, W. Ahmed, C. Hellenthal, H. J. W. Zandvliet, and B. Poelsema, "From nanorods to nanostars: tuning the optical properties of gold nanoparticles," *Colloids and Surfaces A: Physicochemical and Engineering Aspects*, vol. 413, pp. 231–238, 2012.

[3] J. Jiang, G. Oberdörster, and P. Biswas, "Characterization of size, surface charge, and agglomeration state of nanoparticle dispersions for toxicological studies," *Journal of Nanoparticle Research*, vol. 11, no. 1, pp. 77–89, 2009.

[4] L. Kvítek, A. Panáček, J. Soukupová et al., "Effect of surfactants and polymers on stability and antibacterial activity of silver nanoparticles (NPs)," *Journal of Physical Chemistry C*, vol. 112, no. 15, pp. 5825–5834, 2008.

[5] S. K. Ghosh and T. Pal, "Interparticle coupling effect on the surface plasmon resonance of gold nanoparticles: From theory to applications," *Chemical Reviews*, vol. 107, no. 11, pp. 4797–4862, 2007.

[6] J. Duy, L. B. Connell, W. Eck, S. D. Collins, and R. L. Smith, "Preparation of surfactant-stabilized gold nanoparticle-peptide nucleic acid conjugates," *Journal of Nanoparticle Research*, vol. 12, no. 7, pp. 2363–2369, 2010.

[7] L. F. Hohnstedt, B. O. Miniatas, and M. C. Waller, "Aqueous sodium borohydride chemistry: the coinage metals, copper, silver, and gold," *Analytical Chemistry*, vol. 37, no. 9, pp. 1163–1164, 1965.

[8] J. Turkevich, P. C. Stevenson, and J. Hillier, "A study of the nucleation and growth processes in the synthesis of colloidal gold," *Discussions of the Faraday Society*, vol. 11, pp. 55–75, 1951.

[9] J. Kaur and K. Tikoo, "Evaluating cell specific cytotoxicity of differentially charged silver nanoparticles," *Food and Chemical Toxicology*, vol. 51, no. 1, pp. 1–14, 2013.

[10] S. Vijayakumar and S. Ganesan, "In vitro cytotoxicity assay on gold nanoparticles with different stabilizing agents," *Journal of Nanomaterials*, vol. 2012, Article ID 734398, 9 pages, 2012.

[11] D. R. Bhumkar, H. M. Joshi, M. Sastry, and V. B. Pokharkar, "Chitosan reduced gold nanoparticles as novel carriers for transmucosal delivery of insulin," *Pharmaceutical Research*, vol. 24, no. 8, pp. 1415–1426, 2007.

[12] M. M. Tomczak, J. M. Slocik, M. O. Stone, and R. R. Naik, "Bio-based approaches to inorganic material synthesis," *Biochemical Society Transactions*, vol. 35, no. 3, pp. 512–515, 2007.

[13] F. Delbecq, K. Tsujimoto, Y. Ogue, H. Endo, and T. Kawai, "N-stearoyl amino acid derivatives: potent biomimetic hydro/organogelators as templates for preparation of gold nanoparticles," *Journal of Colloid and Interface Science*, vol. 390, no. 1, pp. 17–24, 2013.

[14] Y. Iwasaki, T. Kimura, M. Orisaka, H. Kawasaki, T. Goda, and S.-I. Yusa, "Label-free detection of C-reactive protein using highly dispersible gold nanoparticles synthesized by reducible biomimetic block copolymers," *Chemical Communications*, vol. 50, no. 42, pp. 5656–5658, 2014.

[15] P. R. Selvakannan, S. Mandal, S. Phadtare et al., "Water-dispersible tryptophan-protected gold nanoparticles prepared by the spontaneous reduction of aqueous chloroaurate ions by the amino acid," *Journal of Colloid and Interface Science*, vol. 269, no. 1, pp. 97–102, 2004.

[16] S. K. Bhargava, J. M. Booth, S. Agrawal, P. Coloe, and G. Kar, "Gold nanoparticle formation during bromoaurate reduction by amino acids," *Langmuir*, vol. 21, no. 13, pp. 5949–5956, 2005.

[17] J. D. S. Newman and G. J. Blanchard, "Formation of gold nanoparticles using amine reducing agents," *Langmuir*, vol. 22, no. 13, pp. 5882–5887, 2006.

[18] S. Si, R. R. Bhattacharjee, A. Banerjee, and T. K. Mandal, "A mechanistic and kinetic study of the formation of metal nanoparticles by using synthetic tyrosine-based oligopeptides," *Chemistry*, vol. 12, no. 4, pp. 1256–1265, 2006.

[19] R. R. Bhattacharjee, A. K. Das, D. Haldar, S. Si, A. Banerjee, and T. K. Mandal, "Peptide-assisted synthesis of gold nanoparticles and their self-assembly," *Journal of Nanoscience and Nanotechnology*, vol. 5, no. 7, pp. 1141–1147, 2005.

[20] J. M. Slocik, R. R. Naik, M. O. Stone, and D. W. Wright, "Viral templates for gold nanoparticle synthesis," *Journal of Materials Chemistry*, vol. 15, no. 7, pp. 749–753, 2005.

[21] J. M. Slocik, M. O. Stone, and R. R. Naik, "Synthesis of gold nanoparticles using multifunctional peptides," *Small*, vol. 1, no. 11, pp. 1048–1052, 2005.

[22] S. Si and T. K. Mandal, "Tryptophan-based peptides to synthesize gold and silver nanoparticles: a mechanistic and kinetic study," *Chemistry—A European Journal*, vol. 13, no. 11, pp. 3160–3168, 2007.

[23] K. R. Berry Jr., A. G. Russell, P. A. Blake, and D. K. Roper, "Gold nanoparticles reduced in situ and dispersed in polymer thin films: optical and thermal properties," *Nanotechnology*, vol. 23, no. 37, Article ID 375703, 2012.

[24] D. Zare, A. Akbarzadeh, M. Barkhi et al., "L-arginine and L-glutamic acid capped gold nanoparticles at physiological PH: synthesis and characterization using agarose gel electrophoresis," *Synthesis and Reactivity in Inorganic, Metal-Organic and Nano-Metal Chemistry*, vol. 42, no. 2, pp. 266–272, 2012.

[25] L. Zhang, C. Xu, C. Liu, and B. Li, "Visual chiral recognition of tryptophan enantiomers using unmodified gold nanoparticles as colorimetric probes," *Analytica Chimica Acta*, vol. 809, pp. 123–127, 2014.

[26] J. A. Jacob, S. Naumov, T. Mukherjee, and S. Kapoor, "Preparation, characterization, surface modification and redox reactions of silver nanoparticles in the presence of tryptophan," *Colloids and Surfaces B: Biointerfaces*, vol. 87, no. 2, pp. 498–504, 2011.

[27] L. Polavarapu and Q.-H. Xu, "A single-step synthesis of gold nanochains using an amino acid as a capping agent and characterization of their optical properties," *Nanotechnology*, vol. 19, no. 7, Article ID 075601, 2008.

[28] N. Wangoo, K. K. Bhasin, S. K. Mehta, and C. R. Suri, "Synthesis and capping of water-dispersed gold nanoparticles by an amino acid: bioconjugation and binding studies," *Journal of Colloid and Interface Science*, vol. 323, no. 2, pp. 247–254, 2008.

[29] C. A. Simpson, K. J. Salleng, D. E. Cliffel, and D. L. Feldheim, "In vivo toxicity, biodistribution, and clearance of glutathione-coated gold nanoparticles," *Nanomedicine: Nanotechnology, Biology, and Medicine*, vol. 9, no. 2, pp. 257–263, 2013.

[30] P. R. Selvakannan, S. Mandal, S. Phadtare, R. Pasricha, and M. Sastry, "Capping of gold nanoparticles by the amino acid lysine renders them water-dispersible," *Langmuir*, vol. 19, no. 8, pp. 3545–3549, 2003.

[31] M. Iosin, P. Baldeck, and S. Astilean, "Study of tryptophan assisted synthesis of gold nanoparticles by combining UV-Vis, fluorescence, and SERS spectroscopy," *Journal of Nanoparticle Research*, vol. 12, no. 8, pp. 2843–2849, 2010.

[32] D. M. Richard, M. A. Dawes, C. W. Mathias, A. Acheson, N. Hill-Kapturczak, and D. M. Dougherty, "L-tryptophan: basic metabolic functions, behavioral research and therapeutic indications," *International Journal of Tryptophan Research*, vol. 2, no. 1, pp. 45–60, 2009.

[33] E. E. Finney, S. P. Shields, W. E. Buhro, and R. G. Finke, "Gold nanocluster agglomeration kinetic studies: evidence for parallel bimolecular plus autocatalytic agglomeration pathways as a mechanism-based alternative to an avrami-based analysis," *Chemistry of Materials*, vol. 24, no. 10, pp. 1718–1725, 2012.

[34] T. S. Sabir, D. Yan, J. R. Milligan et al., "Kinetics of gold nanoparticle formation facilitated by triblock copolymers," *Journal of Physical Chemistry C*, vol. 116, no. 7, pp. 4431–4441, 2012.